NAVAL POSTGRADUATE SCHOOL

MONTEREY, CALIFORNIA

DISSERTATION

CORRECTION OF A SPACE TELESCOPE ACTIVE PRIMARY MIRROR USING ADAPTIVE OPTICS IN A WOOFER-TWEETER CONFIGURATION

by

Matthew R. Allen

September 2015

Dissertation Supervisor	Brij Agrawal

Approved for public release; distribution is unlimited

THIS PAGE INTENTIONALLY LEFT BLANK

REPORT DOCUMENTATION PAGE			*Form Approved OMB No. 0704-0188*
Public reporting burden for this collection of information is estimated to average 1 hour per response, including the time for reviewing instruction, searching existing data sources, gathering and maintaining the data needed, and completing and reviewing the collection of information. Send comments regarding this burden estimate or any other aspect of this collection of information, including suggestions for reducing this burden, to Washington headquarters Services, Directorate for Information Operations and Reports, 1215 Jefferson Davis Highway, Suite 1204, Arlington, VA 22202-4302, and to the Office of Management and Budget, Paperwork Reduction Project (0704-0188) Washington DC 20503.			
1. AGENCY USE ONLY *(Leave blank)*	**2. REPORT DATE** September 2015	**3. REPORT TYPE AND DATES COVERED** Dissertation	
4. TITLE AND SUBTITLE CORRECTION OF A SPACE TELESCOPE ACTIVE PRIMARY MIRROR USING ADAPTIVE OPTICS IN A WOOFER-TWEETER CONFIGURATION		**5. FUNDING NUMBERS**	
6. AUTHOR(S) Allen, Matthew R.			
7. PERFORMING ORGANIZATION NAME(S) AND ADDRESS(ES) Naval Postgraduate School Monterey, CA 93943-5000		**8. PERFORMING ORGANIZATION REPORT NUMBER**	
9. SPONSORING /MONITORING AGENCY NAME(S) AND ADDRESS(ES) N/A		**10. SPONSORING/MONITORING AGENCY REPORT NUMBER**	
11. SUPPLEMENTARY NOTES The views expressed in this dissertation are those of the author and do not reflect the official policy or position of the Department of Defense or the U.S. Government. IRB Protocol number ____N/A____.			
12a. DISTRIBUTION / AVAILABILITY STATEMENT Approved for public release; distribution is unlimited		**12b. DISTRIBUTION CODE**	
13. ABSTRACT			

The Department of Defense seeks to improve space-based imaging capabilities by building larger space telescopes designed for higher orbits in order to provide timely accurate imagery to the military and national decision makers. Satellites have mass and volume constraints due to the limited size of the launch vehicle. Larger aperture imagery satellites require lightweight deployable segmented primary mirrors to meet mass and volume constraints. Lightweight segmented mirrors exist but lack the structure and mass necessary for high-quality optical performance. This research investigates using a deformable mirror with a large lightweight active primary mirror to improve optical performance.

Control techniques are applied to simultaneously manipulate an active primary mirror segment and deformable mirror in a woofer-tweeter configuration. Computer simulations and experiments using woofer-tweeter control techniques show reduction of residual wavefront error attributed to the primary mirror. A woofer-tweeter gradient control technique was shown to experimentally reduce wavefront error by 24% using the Naval Postgraduate School's 3-m diameter segmented mirror telescope test bed. The addition of a deformable mirror to an active space telescope in a woofer-tweeter configuration is a technically feasible option for a large-aperture telescope design, and can reduce primary mirror requirements potentially reducing cost.

14. SUBJECT TERMS segmented mirror telescope, dual deformable mirror, woofer-tweeter, space telescope, adaptive optics, active optics, wavefront control			**15. NUMBER OF PAGES** 197
			16. PRICE CODE
17. SECURITY CLASSIFICATION OF REPORT Unclassified	**18. SECURITY CLASSIFICATION OF THIS PAGE** Unclassified	**19. SECURITY CLASSIFICATION OF ABSTRACT** Unclassified	**20. LIMITATION OF ABSTRACT** UU

NSN 7540-01-280-5500

Standard Form 298 (Rev. 2-89)
Prescribed by ANSI Std. 239-18

THIS PAGE INTENTIONALLY LEFT BLANK

CORRECTION OF A SPACE TELESCOPE ACTIVE PRIMARY MIRROR USING ADAPTIVE OPTICS IN A WOOFER-TWEETER CONFIGURATION

Matthew R. Allen
Major, United States Air Force
B.S., Rensselaer Polytechnic Institute, 2000
M.S., Naval Postgraduate School, 2007

Submitted in partial fulfillment of the
requirements for the degree of

DOCTOR OF PHILOSOPHY IN ASTRONAUTICAL ENGINEERING

from the

NAVAL POSTGRADUATE SCHOOL
September 2015

Author:	Matthew R. Allen	
Approved by:	Brij Agrawal Distinguished Professor of Mechanical and Aerospace Engineering Dissertation Supervisor	Marcello Romano Associate Professor of Mechanical and Aerospace Engineering
	Oleg Yakimenko Professor of Mechanical and Aerospace Engineering	Roberto Cristi Professor of Electrical and Computer Engineering
	Jae Jun Kim Research Associate Professor of Mechanical and Aerospace Engineering	
Approved by:	Garth Hobson, Chair, Department of Mechanical and Aerospace Engineering	
Approved by:	Douglas Moses, Vice Provost for Academic Affairs	

THIS PAGE INTENTIONALLY LEFT BLANK

ABSTRACT

The Department of Defense seeks to improve space-based imaging capabilities by building larger space telescopes designed for higher orbits in order to provide timely accurate imagery to the military and national decision makers. Satellites have mass and volume constraints due to the limited size of the launch vehicle. Larger aperture imagery satellites require lightweight, deployable, segmented primary mirrors to meet mass and volume constraints. Lightweight segmented mirrors exist but lack the structure and mass necessary for high-quality optical performance. This research investigates using a deformable mirror with a large lightweight active primary mirror to improve optical performance.

Control techniques are applied to simultaneously manipulate an active primary mirror segment and deformable mirror in a woofer-tweeter configuration. Computer simulations and experiments using woofer-tweeter control techniques show reduction of residual wavefront error attributed to the primary mirror. A woofer-tweeter gradient control technique was shown to experimentally reduce wavefront error by 24% using the Naval Postgraduate School's 3-m diameter segmented mirror telescope test bed. The addition of a deformable mirror to an active space telescope in a woofer-tweeter configuration is a technically feasible option for a large-aperture telescope design, and can reduce primary mirror requirements potentially reducing cost.

THIS PAGE INTENTIONALLY LEFT BLANK

TABLE OF CONTENTS

LIST OF FIGURES

xiv

THIS PAGE INTENTIONALLY LEFT BLANK

LIST OF TABLES

THIS PAGE INTENTIONALLY LEFT BLANK

LIST OF ACRONYMS AND ABBREVIATIONS

AO	adaptive optics
BMC	Boston Micromachine Corporation
CCA	coarse control actuator
CLS	constrained least squares
CMA	Composite Mirror Applications
CTE	coefficient of thermal expansion
DOD	Department of Defense
FCA	fine control actuator
FSA	face-sheet actuator
FSM	field steering mirror
GSD	ground sample distance
GS	gap sensor
HST	Hubble space telescope
JWST	James Webb space telescope
LEO	low Earth orbit
MARS	Membrane with Active Rigid Support
MIMO	multi-input multi-output
OPD	optical path difference
PSF	point spread function
P-V	peak-to-valley
RMS	root-mean-square
SMT	segmented mirror telescope
SVD	singular value decomposition
ULE	ultra-low expansion
WT	woofer-tweeter

THIS PAGE INTENTIONALLY LEFT BLANK

ACKNOWLEDGMENTS

THIS PAGE INTENTIONALLY LEFT BLANK

I.   INTRODUCTION

The National Security Space Strategy seeks to improve U.S. space capabilities that deliver timely and accurate space services to both the military and national decision makers [1]. High-resolution, space-based imagery is one of these capabilities. Imagery collection timeliness, however, is constrained by orbital mechanics and the total number of satellites. This research develops technologies to improve large-aperture, high-altitude imagery satellites that can improve space-based imagery timeliness using fewer satellites while maintaining current imagery accuracy.

Satellites have mass and volume constraints due to the limited size of the launch vehicle. Larger aperture imagery satellites require lightweight deployable primary mirrors to meet mass and volume constraints. Lightweight primary mirrors exist but lack the structure and mass that improve the mirror optical surface performance, which improves the image quality. Using a deformable mirror along with a lightweight primary mirror can allow for the correction of surface errors common with large lightweight primary mirrors. This could allow the development of high-altitude imagery satellites, providing persistent high-resolution imagery from space. The addition of a deformable mirror also provides a robust correctable design that can reduce the primary mirror optical requirements, reduce optical testing during manufacturing, and correct for on-orbit external disturbances.

The goal of this research is to investigate the feasibility of using a deformable mirror with current state-of-the-art large aperture active mirrors recently developed for segmented space telescopes at the Naval Postgraduate School Segmented Mirror Telescope Lab. This research applies and describes control techniques used to simultaneously control a lightweight active primary mirror segment and deformable mirror to reduce the residual wavefront error attributed to the primary mirror. The segmented space telescope model and control techniques are described and simulated results are presented. The control techniques are experimentally validated using the Naval Postgraduate School's 3-m diameter segmented mirror telescope (SMT) test bed.

1

A.   PROBLEM SPACE

Current imagery satellites operate in low Earth orbit (LEO) and use large monolithic primary mirrors to achieve high-resolution images. The LEO limits the time a satellite is in view of a ground target and the constellation size limits the frequency the target is revisited. Raising the orbit of the satellite increases the time the satellite is in view of the ground target. To achieve similar ground resolution at a higher altitude, however, the primary mirror's diameter must increase. The primary mirror size required for a medium Earth orbit (MEO) or geostationary Earth orbit (GEO) high-resolution imagery satellite is greater than the diameter of available launch vehicle fairings.

The launch vehicle volume and mass constraints impact the space telescope primary mirror design. The volume constraint forces a trade between a monolithic primary mirror and a segmented mirror. A monolithic primary mirror offers a simpler design, but a deployable-segmented mirror allows a primary mirror with a diameter larger than the launch vehicle fairing diameter. The mass constraint impacts primary mirror stiffness and primary mirror optical surface figure. Past space telescope primary mirrors depended on stiffness achieved through structure and mass to maintain their optical surface quality. However, a constraint on mass requires larger primary mirrors to reduce density, therefore reducing stiffness, and potentially reducing surface figure performance.

Current large lightweight mirror technologies do not meet surface error requirements for a visible telescope. This research proposes the addition of a deformable mirror to a space telescope optical assembly in a woofer-tweeter configuration to compensate for these surface errors. Researchers considered active mirror systems for space telescopes since the early developments of adaptive optics. Howell [2] provides an overview of early advances in large space telescope optical control. This study uses a deformable mirror and active primary mirror together to correct residual surface errors of the active replicated primary mirrors. This research builds upon several fields of study including adaptive optics, telescope and mirror design, structures, and controls. Several key pieces of literature are discussed.

Babcock [3] introduced the modern concept of adaptive optics in 1953, and an early implementation was adding tip/tilt compensation to the Wilson Observatory in 1956 to compensate for atmospheric scintillation. Adaptive optics technologies continued to develop through the 1990s primarily for defense purposes. Hardy [4], Greenwood, and Primmerman [5] provide a concise overview of the early history of adaptive optics. In the 1980s Nelson, Mast, and Faber [4] recommended building a ten-meter telescope using a segmented primary mirror. This recommendation resulted in the development of the Keck Observatory included the necessary wavefront sensing and control systems. Chanan et al. provide an overview of the techniques used to actively phase the primary mirror segments [5]–[8]. The success of ground-based segmented telescopes furthered research in segmented space telescopes.

Lane et al. [9] provide an overview of past efforts to develop deployable space telescope technology. This includes the development of several ground-based technology demonstrations and experiments from the late 1980s to the early 2000s. However, the main development in segmented space telescope technology is the 6.5 meter 18 segment infrared James Webb Space Telescope (JWST). The JWST required new wavefront sensing techniques like dispersed fringe sensing presented by Shi et al. [10] and control techniques presented by Redding et al. [11].

Researchers continue to develop technologies to support visible wavelength segmented space telescopes with a focus on development of advanced lightweight primary mirror segments. Current advanced mirror technologies under consideration include actuated hybrid mirrors (AHM) described by Hickey et al. [12], [13], and carbon fiber mirror technologies presented by Romeo et al. [14] and Steeves et al. [15]. Both technologies are lightweight replicated optics and can include embedded actuators to compensate for surface figure errors. However, current AHM mirrors and carbon fiber mirrors struggle to achieve optical surface performance of traditional monolithic glass mirrors.

B.   RESEARCH RESOURCES

To address the design challenges of a large aperture deployable space telescope the Department of Defense (DOD) developed the Segmented Mirror Demonstrator (SMD) telescope.   The SMD telescope developed critical segmented mirror telescope technologies including lightweight active mirror segments, deployment mechanisms, and wavefront sensing and control technologies using a ground-based demonstration.   After program completion the DOD transferred the SMD telescope to the Naval Postgraduate School and renamed the telescope the Segmented Mirror Telescope (SMT).

The SMT is a 3-meter deployable-segmented telescope with six hexagonal active 1-meter segments.   The active mirror segments have many advantages over traditional mirrors.   The segments are lower cost, lower mass, and actively correct surface errors using a wavefront sensing and control system.   The optical telescope assembly includes the control system as part of the optical prescription.   The SMT has 992 actuator inputs including 936 surface parallel face sheet actuators, 18 fine control actuator, 36 coarse control actuators, and a tip/tilt fast steering mirror.   The SMT sensors include a Shack-Hartmann wavefront sensor, phase diversity sensor, and segment edge sensors.   Figure 1 shows the SMT located at the Naval Postgraduate School.

Figure 1. Naval Postgraduate School segmented mirror telescope

The SMT active segments have residual surface errors after correction. The segment manufacturing process caused residual surface error consisting of high spatial frequency print-through. The fixture points on the back of the segments also caused larger low spatial frequency errors. Figure 2 shows a two-dimensional plot of the SMT segment optical path difference measured in waves (632.8 nm) after applying a correction. The high spatial frequency print-through error caused by the segment ribs, low spatial frequency error caused by the fine control actuator attachment points, and mirror surface defects are apparent.

SMT Segement Residual WFE
RMS WFE = 0.313
Peak-to-Valley WFE = 2.4023
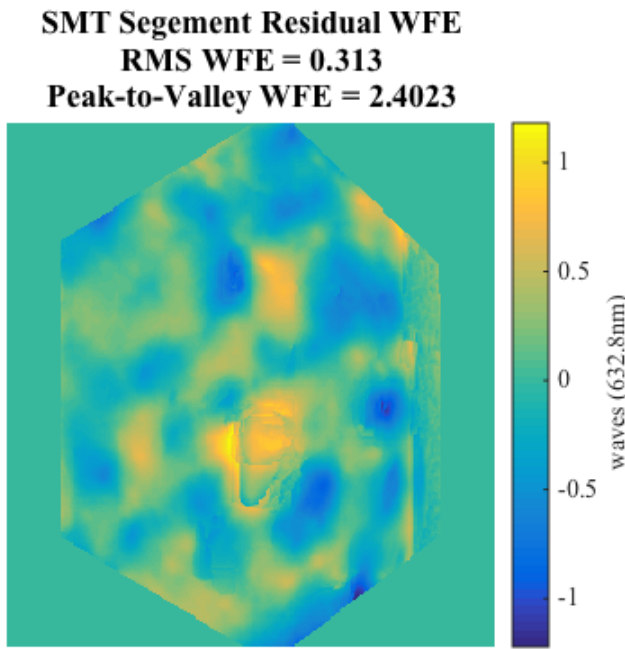
Figure 2. SMT segment residual surface error, 0.32468 waves RMS wavefront error and 2.5464 waves peak-to-valley wavefront error, from [16]

For this research the SMT test bed was modified to include a deformable mirror in the optical path. This is similar to a woofer-tweeter adaptive optics system used to compensate for atmospheric turbulence in astronomical telescopes and high-energy lasers systems. In these systems the woofer deformable mirror compensates for low spatial and temporal frequency disturbances, and the tweeter deformable mirror compensates for high spatial and temporal frequency disturbances. However, a space-based woofer-tweeter system does not have to correct atmospheric high temporal frequency

disturbances, but rather static errors and low frequency disturbances caused by a thermally dynamic environment [17], [18]. In this system the SMT active segment represents the woofer and the additional deformable mirror represents the tweeter.

In addition to active segmented mirror technologies, NPS conducts research in lightweight monolithic mirrors with the intent of reducing mass and manufacturing cost. Figure 3 shows a 1-meter carbon fiber mirror from Composite Mirror Applications (CMA) delivered to NPS in March 2012. The mirror surface shows significant manufacturing print through (quilting) on the optical surface (see Figure 4). Despite the poor optical quality, the relative low cost and short manufacturing time is an attractive quality if the optical performance can be improved or corrected. Adding a deformable mirror to a passive carbon fiber primary telescope can also improve optical performance.

Figure 3. Carbon fiber reinforced polymer mirror, 1-meter without optical coating
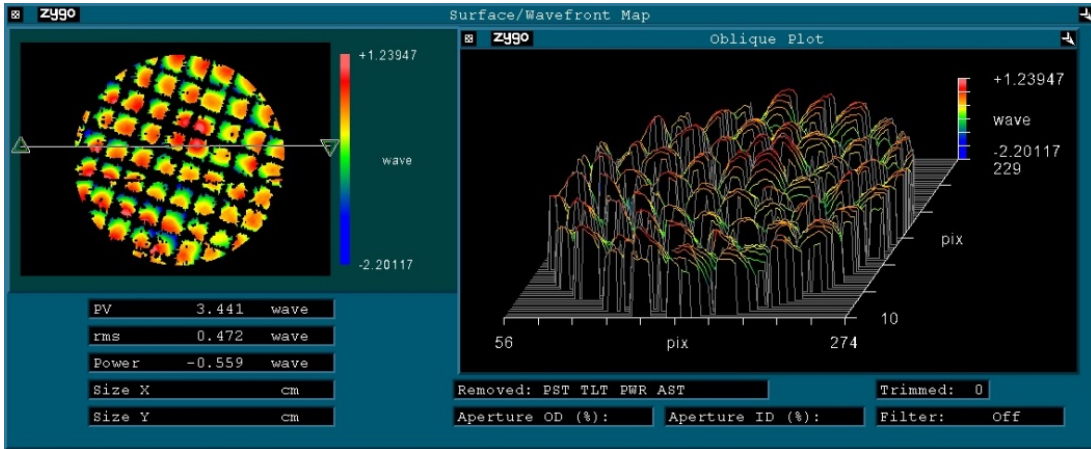
Figure 4. Carbon fiber reinforced polymer mirror surface error, RMS
wavefront error of 0.472 waves, peak-to-valley wavefront error of 3.443 waves

C.   RESEARCH OBJECTIVES

The objective of this research is to advance control techniques for woofer-tweeter space telescopes. This research demonstrates wavefront error improvement on the SMT test bed using new control techniques. The addition of active optics to the telescope and new control techniques may enable current and future lightweight primary mirror designs. The specific research objectives are to:

- Develop an analytical segmented space telescope model with an additional deformable mirror in the optical telescope assembly

- Develop control algorithms to simultaneously control an active primary mirror and deformable mirror to reduce wavefront error

- Experimentally validate the space telescope model and control techniques

- Reduce the surface error of the SMT segment by controlling the segment and deformable mirror simultaneously

D.   DISSERTATION OUTLINE

Chapter II provides background information for this research including an overview of remote sensing. The background includes an overview of large aperture mirror technologies and limitations of the current technology. The second chapter also

includes a review of the history of segmented telescopes and recent developments in segmented space telescopes. An overview of adaptive optics, the SMT test bed, and previous SMT research is provided.

Chapter III describes the analytical space telescope modeling approach, and the placement of the deformable mirror in the SMT optical telescope assembly. In Chapter III the analytical model of the SMT and the additional deformable mirror are described, as is the combination of these models to create a dual deformable mirror model.

Chapter IV describes using woofer-tweeter control techniques to simultaneously control the SMT active primary segment and the deformable mirror. A new woofer-tweeter gradient control technique is proposed using singular value weighting. Chapter IV also introduces a technique to iteratively update the influence matrix to improve mirror performance when there is uncertainty in the influence matrix or a non- linear response in the SMT AHM mirror.

Chapter V presents computer-simulated results of the control techniques described in Chapter IV. The SMT coarse alignment, coarse phasing, and fine phasing simulations demonstrate the need to improve the SMT segment surface error. The woofer-tweeter simulations show the feasibility of adding a deformable mirror to the optical telescope assembly and predict the performance of the different woofer-tweeter controllers. The simulated results show the iterative constrained minimization controller and global gradient controller outperform the traditional woofer-tweeter control approaches. The simulation results also show that controlling the woofer and tweeter simultaneously outperforms controlling them serially.

Chapter VI describes the experimental system and presents the experimental results. The results are compared to the simulated results and show that the woofer-tweeter outperformed the SMT segment performance and outperform operating the mirrors serially. The SMT AHM actuator response and SMT mirror surface response is experimentally characterized and the results show operating regions with a non-linear response. Finally, the adaptive influence matrix technique showed a small improvement in residual wavefront error when using an uncertain influence matrix.

Chapter VII provides a summary of the dissertation contributions with recommendations for future work.

THIS PAGE INTENTIONALLY LEFT BLANK

II.   BACKGROUND

This dissertation develops control techniques for an active primary mirror space telescope with an additional deformable mirror. This work requires an understanding of several fields of study including optics, structures, and controls. This background provides an overview of the technologies that support the development of future large aperture space telescopes. The chapter begins with an overview of space-based remote sensing characteristics followed by a review of space telescope mirror technologies. The chapter then provides background on adaptive optics and discusses segmented mirror telescopes. The chapter finishes with a background on segmented mirror telescope research conducted at the Naval Postgraduate School.

A.   SPACE-BASED EARTH REMOTE SENSING

Spatial resolution, spectral resolution, and temporal resolution are performance characteristics of space-based remote sensing systems. Payload and satellite designers trade these characteristics to optimize the performance for the mission. The satellite payload spatial resolution depends on angular resolution and is determined by the Rayleigh criterion, Equation (2.1), where λ is the wavelength and D is the aperture diameter. This spatial resolution translates to a ground resolution using the small angle approximation, Equation (2.2), where R is the range from the target ground resolution is the smallest resolvable spot size on the Earth.

$$\theta = 1.22\frac{\lambda}{D} \tag{2.1}$$

$$\text{Ground Resolution} \approx \theta \cdot R \tag{2.2}$$

The satellite orbit constrains the temporal resolution. Equation (2.3) determines the orbital period of a satellite in circular orbit where r is the orbit radius and μ is the standard gravitational parameter. Therefore a satellite at a higher circular orbit has a longer view of a target, but a worse ground resolution than a system with the same spatial resolution at a lower orbit. Temporal resolution also relates to the revisit rate of the satellite over a specific ground target.

$$T = 2\pi\left(\frac{r^3}{\mu}\right) \qquad\qquad (2.3)$$

The time a satellite is in continuous view of a target on a single orbit is the satellite dwell time. In LEO dwell times are measured in minutes and depend on both the orbit and the off nadir pointing capability of the satellite. As the satellite orbit approaches a geosynchronous orbit the dwell time approaches infinity meaning that there is persistent coverage of the target from a single satellite.

To increase dwell time and maintain the same ground resolution as a LEO imagery satellite the angular resolution must decrease by increasing the aperture diameter. New telescope technologies like lightweight large aperture replicated mirrors and segmented mirror telescopes can enable future large aperture remote sensing telescopes that operate in high altitude orbits.

B.   SPACE TELESCOPE MIRROR TECHNOLOGIES

This section provides an overview of space telescope mirrors including existing on-orbit mirror technologies and new technologies developed for large aperture space telescopes. Advantages and disadvantages of each technology are presented as well as physical properties. This survey gives the reader an overview of current mirror capabilities and a historical perspective.

New technologies include large aperture replicated optics and large lightweight active mirrors. In most cases active mirrors are also replicated optics. Replicated mirrors are formed using a mandrel where the mirror is a negative spatial image of the mandrel. This process produces identical copies where the surface quality closely matches the quality of the mandrel. Traditional grinding and polishing mirror-manufacturing processes result in an original optical element. An active mirror includes actuators that apply controlled forces to change the shape of the mirror. Active mirrors can be replicated or manufactured using grinding and polishing methods.

Traditional grinding and polishing mirror-manufacturing methods can take years. For example, the 18 JWST segments took 8 years to complete manufacturing [19]. Large replicated mirrors are desirable because they offer a lower cost, high volume, and shorter

manufacturing process over traditional grinding and polishing methods [20]. Segmented mirrors require multiple copies of the same mirror making replicated mirrors desirable.

Hickey, Barbee, Ealey, and Redding make the argument for actively controlled lightweight mirrors for space telescopes [21]. They assert that reduction in mass and the ability to correct for surface figure error, testing errors, and on orbit degrading effects outweighs increased complexity. This technology has the potential to reduce program risk of large primary optics by relaxing fabrication requirements, testing requirements, integration requirements and reducing overall schedule. Reducing mass compared to conventional optics can also reduce system cost in addition to cost savings associated with reduced risk. These savings must be traded against the complexity of adding a wavefront sensing and control system to actively correct the mirror surface.

1.   Ultra Low Expansion Glass Mirrors

Ultra Low Expansion (ULE) glass is the standard for primary mirror construction for optical telescopes. The Hubble Space Telescope (HST) primary mirror began development in the late 1970s, launched in 1990, and remains the largest primary mirror in space at 2.4-meter diameter. The Kepler Space Telescope launched in 2009 and uses a 1.4-meter ULE glass primary mirror similar to the HST. These mirrors have great properties for space telescope missions, as ULE glass is thermally stable, stiff, and can be polished to optical requirements [22]. A downside to ULE glass mirrors is mass as the area density (mass / optical surface) is approximately 180 kg/m^2 [22]. The current primary mirrors are monolithic and scaling those mirrors to a larger diameter will decrease the stiffness, requiring an increase in support structure to maintain stiffness requirements [22]. The mass and stiffness requirements make ULE undesirable for a large telescope.

2.   Beryllium Mirrors

In the mid-1990s NASA began developing beryllium mirror technologies for the JWST program. Beryllium mirrors offer several advantages over ULE glass, including lighter mass, super cryogenic coefficient of thermal expansion (CTE), and thermal sensitivity. The thermal properties drove the decision to use Beryllium since it

outperformed ULE over the telescope temperature operating range [23]. The JWST beryllium mirror segments have an areal density of approximately 10 kg/m^2. The segments are also active and have center actuators that compensate for mirror curvature. In addition to the JWST the infrared Spitzer Space Telescope uses beryllium for the 85-cm primary mirror to meet required thermal properties.

3. Glass Membrane Facesheet with Active Rigid Support

In the late 1990s the University of Arizona developed a prototype mirror known as Membrane with Active Rigid Support (MARS) to demonstrate advance mirror concepts for the JWST program. The MARS mirrors were non-replicated active mirrors. A glass membrane was ground and polished from a glass blank. The resulting 2mm thick glass membrane was attached to a rigid carbon fiber epoxy support structure. The demonstrator for the JWST had a 2m diameter, 166 actuators, and an areal density of 13kg/m^2 [24], [25]. Glass membrane mirror designs traded the total number of actuators and the membrane thickness. The actuators corrected surface warping of the membrane, but the discrete actuator locations caused rippling of the membrane. Adding actuators or increasing the thickness of the membrane could have fixed this problem.

4. Actuated Hybrid Mirrors

Actuated hybrid mirrors (AHM) are replicated active mirrors that are an alternative to conventional glass primary mirrors. Developed in the early 2000s by AOA Xinetics, AHM technology combined actuated integrated zonal meniscus mirrors with a nanolaminate foils [12], [21], [26], [27]. The integrated zonal meniscus mirrors combine an optical substrate, a mirror surface, and embedded actuators in the support structure parallel to the mirrors surface. The actuators generate bending moments to control the shape of the mirror surface. The mirror surface is a nanolaminate foil made from a magnetron sputtering process developed at Lawrence Livermore National Laboratory [27]. The process coats a polished mandrel surface atom by atom to form a foil that is 10-100 microns thick. The magnetron sputtering process first deposits a carbon layer that serves as a release layer from the mandrel. The process then applies a reflective layer like gold to form the optical surface. The next step adds alternating crystalline layers and

amorphous layers of zirconium and zirconium/copper to form the laminate foil [21]. The substrate bonds directly to the foil while attached to the mandrel.

Figure 5 shows the elements of an AHM. The substrate is a rib-stiffened silicon carbide (SiC) structure cast to meet the required optical figure. The nanolaminate face sheet forms on a precision mandrel and bonds to the surface of the SiC substrate. Lead magnesium niobate (PMN) electro static surface parallel actuators bond to the substrate ribs with an epoxy. Fine control actuators and backing hardware attaches to the segment to position the mirror. The result is a replicable mirror segment that has an areal density of approximately 20 kg/m². AHM mirrors greater than 1-meter diameter achieved a RMS wavefront error of 42 nm [21].
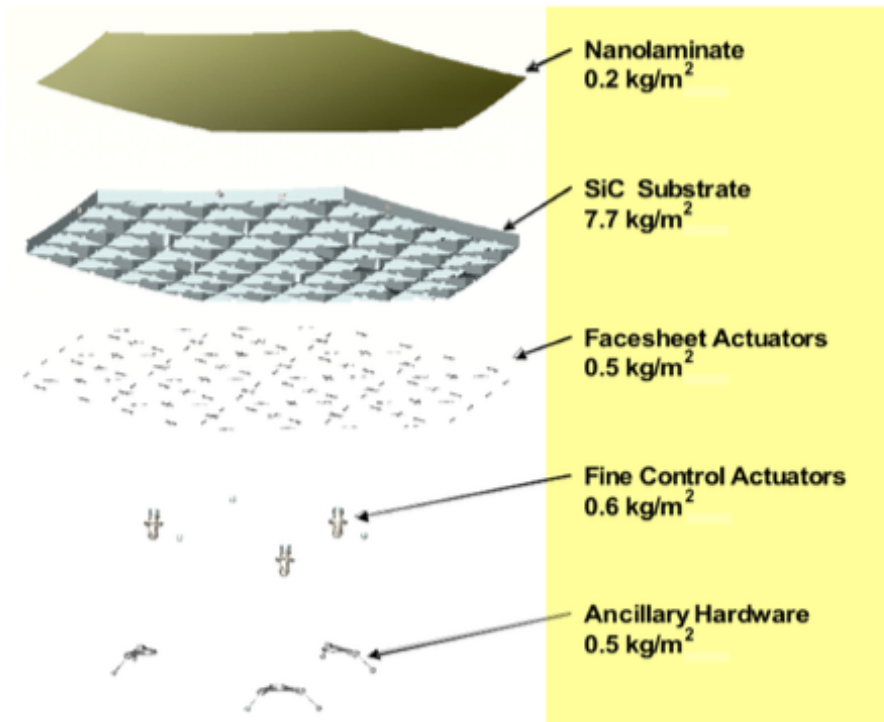
Figure 5. Actuated Hybrid Mirror from [21]

5. Carbon Fiber Mirrors

Interest in replicated Carbon fiber reinforced polymer (CFRP) mirrors began in the mid-1990s because the material properties are attractive for optical systems. CFRP is

very stiff, has a low CTE, thermal conductivity similar to steel, and low areal density between 2-10 kg/m^2 depending on structural configuration [28]. The fabrication process uses a negative shape polished mandrel to form the mirror surface. The manufacturer layers CFRP prepreg over the mandrel and after curing applies the structural core to the back of the face sheet. The manufacturer then releases the mirror from the mandrel and applies the optical coating [14], [29]. The optical performance of these mirrors depends on the surface quality of the mandrel as well as mitigating fiber and core print through issues. Figure 6 shows the 1-meter diameter CFRP mirror at the Naval Postgraduate School with an areal density of 17.6 kg/m^2 including the substrate structure. The residual wavefront error of this mirror is presented later in Chapter III.

Figure 6. 1-meter carbon fiber reinforced polymer mirror

CMA, Naval Research Laboratory (NRL), and Sandia National Laboratories (SNL) developed active CFRP mirrors and showed that astigmatism is inherent to large aperture CFRP mirrors due to the isotropic nature of CFRP. CMA, NRL, and SNL mounted actuators to the back of the CFRP mirror to correct low order aberrations using closed loop feedback. They experimentally demonstrated an actuation method to change the CFRP mirror radius of curvature [30], [31].

Steeves et. al [15] developed another CFRP mirror concept called carbon shell mirrors (CSMs). The mirror substrate is a thin shell made from CFRP. The reflective

layer is a nano-laminate bonded to the front of the CFRP substrate. An active layer is bonded to the back of the substrate to provide surface parallel actuation. Figure 7 shows a diagram of the mirror. CSMs with a diameter of 175 mm have been prototyped with an areal density of 1.5-2.7 kg/m^2, but do not include a support structure. The current prototypes do not meet surface requirements for visible wavelength applications, but demonstrate potential for large correctable space telescope mirrors.
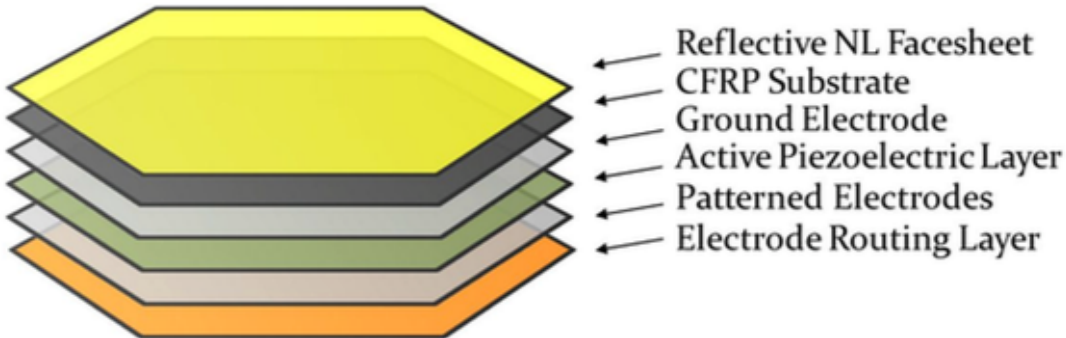
Figure 7. Exploded diagram of the CSM layers from [15]

C.   ADAPTIVE OPTICS

Adaptive optics is a multidisciplinary field focused on improving the performance of an optical signal. The SMT design and this research are founded on the principles of adaptive optics. This section provides a background of adaptive optics systems including woofer-tweeter adaptive optics. The principle components of an adaptive optics system are described including wavefront sensors, deformable mirrors, and adaptive optics control techniques. The research in this dissertation builds on these principles.

1.   Background

The two major historical applications of adaptive optics have been laser beam control and astronomical imaging. Initial work in adaptive optics began when Babcock [3] introduced the concept of adaptive optics in 1953 to compensate for atmospheric scintillation when making astronomical observations. Later in 1957, Linnik [32]

proposed using segmented mirrors to compensate for atmospheric turbulence including the use of a reference beacon.

The invention of the laser in 1960 led to the use of adaptive optics in laser beam control and atmospheric compensation for defense purposes. Hardy [33] and Greenwood [34] give a historical overview of early adaptive optics research focused on defense applications from the late 1960s through the early 1990s. One use of adaptive optics was the development of tactical and strategic military laser systems. Initial adaptive optics research and experiments compensated for laser propagation through the atmosphere. Later research investigated compensating thermal blooming of high-energy lasers through the atmosphere for strategic defense applications.

Image compensation adaptive optic applications began in the 1980s to improve the performance of large ground telescopes used by the DOD for space surveillance. Adaptive optics compensated for atmospheric turbulence to improve telescope performance. Hardy [33] summarizes the early development of astronomical telescope compensation systems including the use of laser guide stars. These techniques were later declassified and transferred to the astronomical telescope community in the early 1990s.

Two mirror adaptive optics systems were introduced in the 1990s to compensate for phase and amplitude of lasers propagated through atmospheric turbulence and thermal blooming [35], [36]. The air borne laser (ABL) program used several adaptive optics systems to compensate for atmospheric turbulence for the high-energy laser weapon. The ABL program introduced a woofer-tweeter system to compensate for wavefront errors caused by thermal heating of the optics and errors from the laser cavity [37]. The deformable mirror called a woofer compensates for low spatial and temporal frequency disturbances while the tweeter compensates for high spatial and temporal frequency disturbances.

Hampton et al. proposed woofer-tweeter systems for ground-based astronomical telescope atmospheric correction [38]. These systems addressed the adaptive optic system requirements for future large aperture ground-based telescopes. Instead of designing a single deformable mirror to meet both large actuator stroke and high actuator

density requirements the researchers proposed using two of deformable mirrors. The woofer deformable mirror has large stroke, fewer actuators, and correct large amplitude but low spatial and temporal frequency errors. The tweeter deformable mirror has high actuator density with smaller stroke and corrects small amplitude high spatial and temporal frequency errors. Gavel and Norton demonstrated woofer-tweeter techniques using the Lick 3-meter telescope [39].

2.   Components

The primary components of an adaptive optics system are the wavefront sensor, wavefront corrector, and control system. Configurations of these components depend on the application, but the purpose of the wavefront sensor is to provide feedback, the wavefront corrector compensates the wavefront, and the control computer reconstructs the wavefront and/or computes the control signal for the wavefront compensator. Figure 8 shows an example adaptive optics system.
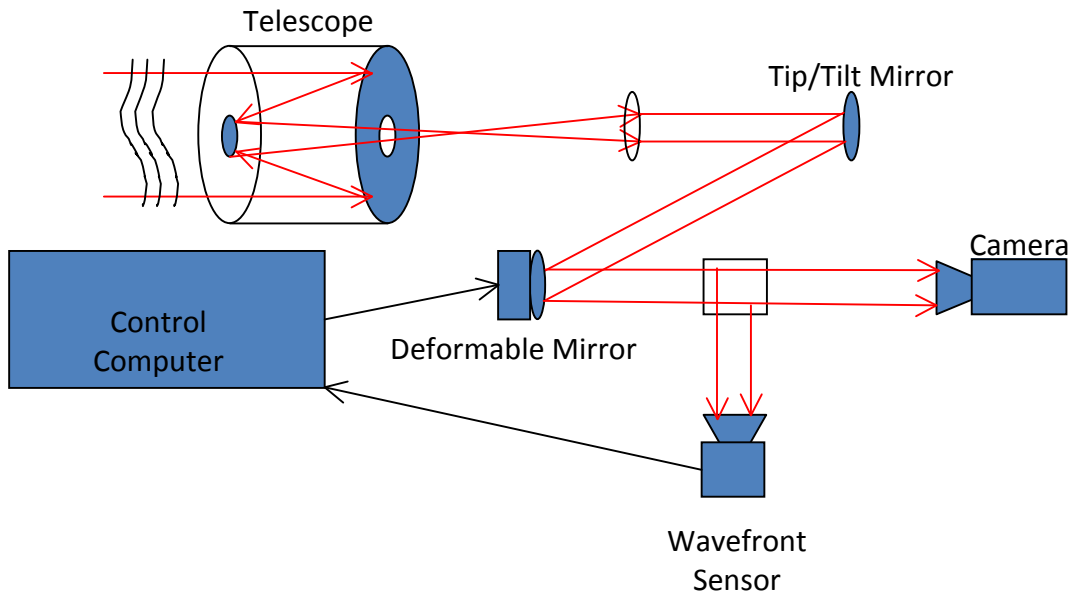
Figure 8. Example adaptive optics system

a.   *Wavefront Sensors*

Wavefront sensors in adaptive optics systems provide feedback to the wavefront corrector and operate at a frequency greater than the disturbance being corrected. Typical wavefront sensors in adaptive optics systems include Shack-Hartmann, curvature, and phase diversity. A Shack-Hartmann wavefront sensor output is proportional to the wavefront slope measured at the pupil plane. The wavefront can be reconstructed from these measurements. A curvature sensor and phase diversity sensor measure irradiance at two locations at or near the image plane, but use different phase retrieval techniques.

Figure 9 shows a one-dimensional geometric representation of a Shack-Hartmann wavefront sensor. The sensor consists of an array of lenses in front of a camera. Light passes through the lenses and creates small focus spots on the camera. The spots are proportional to the local wavefront tilt at the location of each lens. The local wavefront slopes is calculated from the lateral shifts, Δx_{ij}, of the local focal point on the sensor. To estimate the phase we use the relationship between slope and phase points as described by Southwell [40].
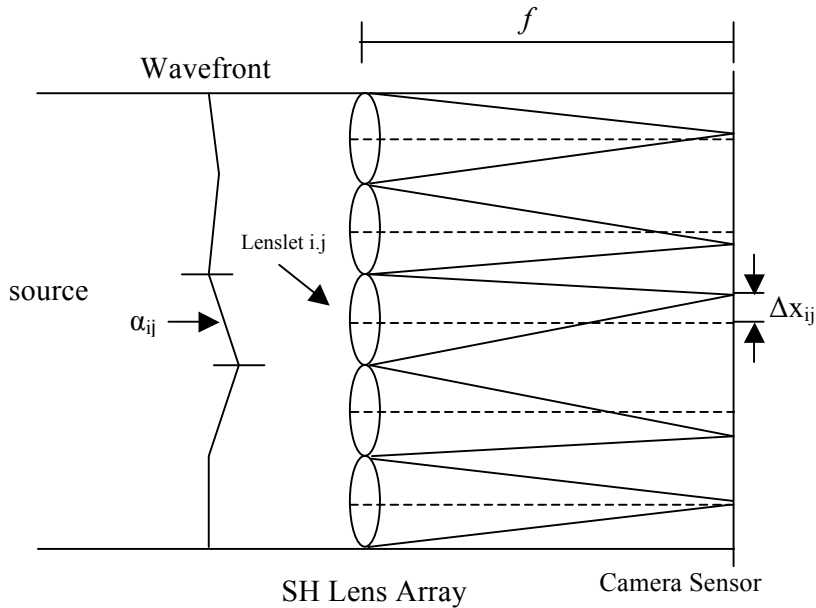
Figure 9. Shack-Hartmann wavefront sensor, after [40]

A curvature sensor uses an image sensor to take two highly out of focus images in two planes that are symmetric about the focal plane [41]. The intensity of the image pixels measures the irradiance distribution at the out of focus planes. Figure 10 shows an example of a curvature sensor described by Roddier [42]. The difference in irradiance distribution between the two planes is a measure of the local wavefront curvature. Using the sensor data and solving the irradiance transport equation with the proper boundary conditions estimates the phase [43]. Figure 11 shows an example of the curvature sensor measurements, difference image and reconstructed wavefront for a wavefront with astigmatism.
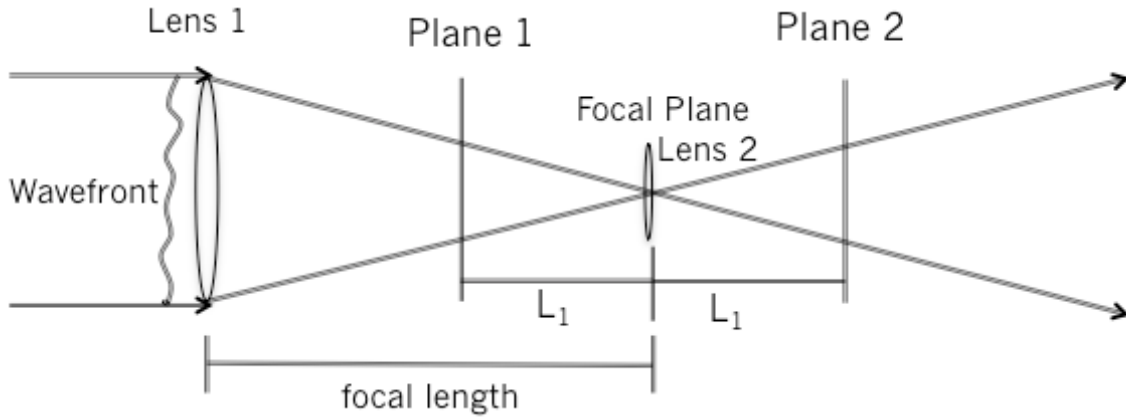
Figure 10. Curvature wavefront sensor example, after [42]
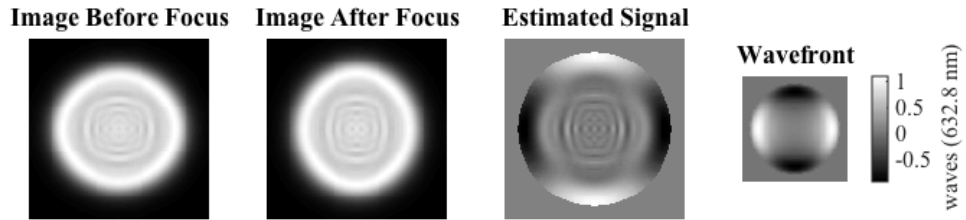
Figure 11. Curvature wavefront sensor example of wavefront with astigmatism.

Phase diversity sensors also measure intensity to retrieve phase information. However, the intensity measurements are usually asymmetric with a measurement at the focal plane and one just slightly out of focus on the order of a single wave. The

wavefront is estimated from the intensity measurements using phase retrieval algorithms like the Gerchberg-Saxton algorithm [44] or modified Gerchberg-Saxton algorithm [45]. These algorithms use the fact that the Fourier transform relates the complex amplitude field at the pupil and the image plane. The image intensity measured from the phase diversity camera provides the magnitude of the complex amplitude but not the phase. However, by iteratively processing multiple defocused images one can correlate the intensity variations between the images and compute the wavefront.

The wavefront sensors work well for fine phasing and surface figure control, however the sensors cannot determine wavefront phase differences greater than 2π. The 2π ambiguity is caused by alignment piston error of the segments. Coarse segment phasing requires a different sensor and phase retrieval technique that can retrieve phase errors greater than a wavelength. Dispersed fringe sensing (DFS) was developed to phase the JWST segments and has been experimentally tested using the ground-based Keck telescope. DFS can produce a direct measurement of the magnitude of the piston error. The technique uses a grated prism placed at the interface of two segments to disperse broadband light from a point source onto a camera to create a fringe image. To solve for piston a least squares routine uses the measured intensity of the fringe images to solve the parameters of the fringe equation (2.4) where I is the dispersed fringe intensity, x is the dispersion coordinate, I_0 is the mean intensity, γ is the fringe visibility between 0 and 1, and ϕ is the phase constant [46].

$$I(x,y) = I_0 \left[1 + \gamma \cos \left(\frac{2\pi}{\lambda(x)} \delta + \phi(y) \right) \right] \tag{2.4}$$

b.   Deformable Mirror

The tip/tilt mirror is one of the simplest wavefront compensators and can operate at very high temporal frequencies but only compensates for tip/tilt spatial modes. Deformable mirrors can correct more spatial frequencies by adding more actuators, but the temporal frequency is typically reduced. Figure 12 shows a plot of spatial frequency versus temporal frequency for a deformable mirror. The spatial frequencies are represented as a fraction of the mirror diameter. The deformable mirror correction

capabilities are also dependent on actuator stroke. Stroke, spatial frequency, and temporal frequency are deformable mirror design trades. Generally low spatial frequency correction requires large amplitudes while higher spatial frequency correction requires small amplitudes. Therefore most adaptive optic systems include multiple wavefront compensators to meet wavefront correction requirements in terms of stroke, spatial correction and temporal correction.
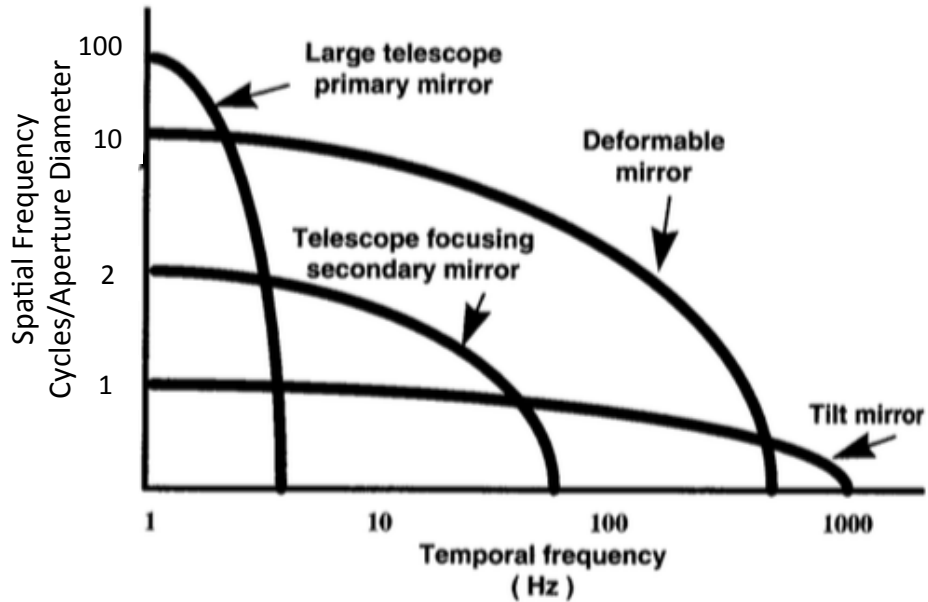
Figure 12. Spatial frequency versus temporal frequency of wavefront compensating mirrors, after [47]

Figure 13 shows examples of current deformable mirror actuator technologies and geometries. The two main actuator configurations are surface normal and surface parallel. Deformable mirrors with surface normal actuators create a local influence on the mirror surface while surface parallel actuators create both a local influence and a global influence. In both cases the mirror response is designed to be linear, and the actuator responses obey the principle of linear superposition. This means that the entire mirror response to a set of actuator commands is a linear combination of the response of the individual actuators being commanded.

23

Some deformable mirror technologies combine different types of actuators geometries. For example, a surface parallel mirror may have global control actuators like in the top right mirror in Figure 13 and another set of local actuators nested within the substrate ribs. This configuration increases the actuator density and allows for the correction of more spatial frequencies, but the actuators experience coupling and the assumption of linear superposition does not hold.

Deformable mirror actuators are typically piezoelectric or electrostrictive and generate a displacement producing a constant strain on the mirror structure. Lead zirconate titanate (PZT) piezoelectric actuators produce a strain linearly proportional to the applied electric field. Lead magnesium niobate (PMN) electrorestrictive actuators produce a strain proportional to the square of the applied electric field [48].
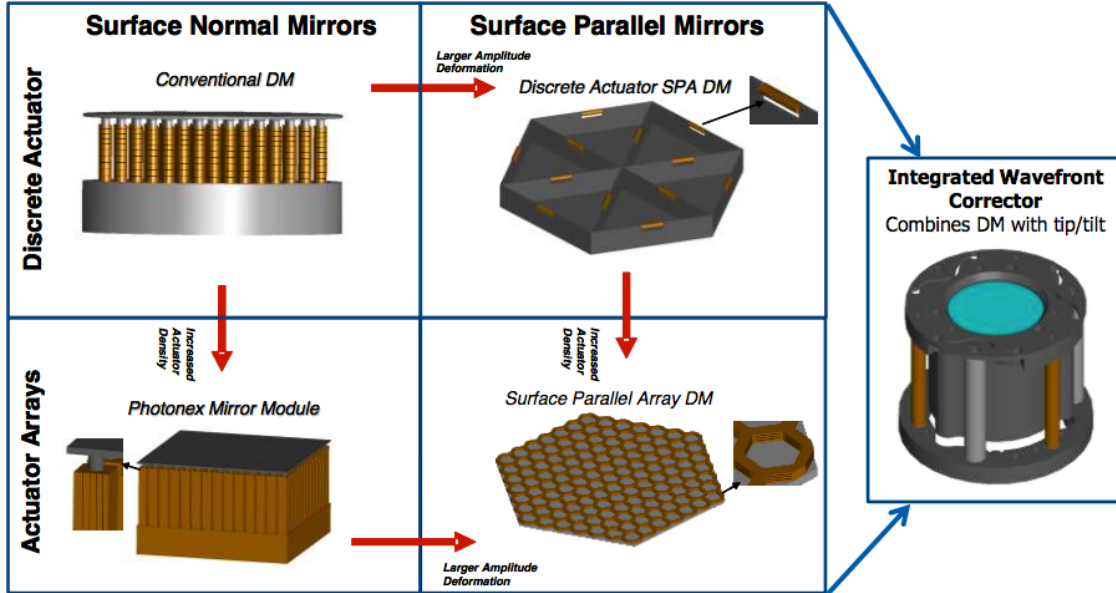
Figure 13. Deformable mirror technologies, from [49]

3. Adaptive Optics Control

Most adaptive optics control techniques exploit the linear behavior of deformable mirrors. In addition to the assumption of linear response we assume the deformable mirrors dynamics are much faster than the bandwidth of the feedback sensors. This

allows the deformable mirror control system to use a static controller built from an influence matrix. An influence matrix converts deformable mirror actuator inputs to a deformable mirror response, usually the wavefront sensor output. The influence matrix contains column vectors called influence functions, equation (2.6). To form the influence function the mirror is set to a biased position and each actuator is individually actuated in the positive and negative direction. Equation (2.5) shows the positive and negative mirror responses are averaged, and normalized over the control input voltage, v, for each actuator, a_i. Equation (2.7) relates the input control vector u to the mirror output y using the influence matrix Γ. The reconstruction matrix relates the desired output to a set of control signals by taking the Moore-Penrose pseudo-inverse Γ, equation (2.8).

$$Influence\_Function(a_i) = b_i = \frac{b_i^+ - b_i^-}{2v} \tag{2.5}$$

$$\Gamma = \begin{bmatrix} b_1 & b_2 & \dots & b_n \end{bmatrix} \tag{2.6}$$

$$y = \Gamma u \tag{2.7}$$

$$R = \left(\Gamma^T \Gamma\right)^{-1} \Gamma^T \tag{2.8}$$

Most adaptive optics systems use a feedback integral controller. In this control approach the control signal is proportional to the integral of the error. Equation (2.10) implements the discrete time integral control using the reconstruction matrix R, a gain g, and error signal defined in equation (2.9) where y is the measured wavefront and y_0 is the desired wavefront.

$$e_k = y - y_0 \tag{2.9}$$

$$u_{k+1} = g\,\mathrm{Re}_k + u_k \tag{2.10}$$

D.   SEGMENTED TELESCOPES

The telescope used in this research is a segmented telescope. The SMT was one of the first visible large aperture segmented telescopes where the control system was included in the optical prescription. This section provides background on the reason for using segmented telescopes, provides a review of segmented telescope research, and describes the SMT.

1.   Background

Manufacturers and researchers can fabricate larger and lighter monolithic mirrors than the HST. However, scaling existing traditional monolithic mirrors introduces mirror stiffness problems. The mirror must be stiff enough to allow manufacturing, maintain the proper shape, and survive launch. Increasing the mirror diameter without increasing the thickness drastically reduces the mirror's stiffness requiring the addition of stiffening support structure. Large aperture telescopes require a segmented mirror to fit in the launch vehicle fairing [22].

The transition of space-based telescopes from monolithic primary mirrors to segmented mirrors is partially based on the success of ground based astronomical segmented telescopes. A ground-based segmented telescope was proposed in the late 1970s in order to build cost effective 10-meter diameter telescopes. The result was the first of two Keck telescopes completed in 1993 using 36 segments. The Keck telescope actively aligns the segments and adjusts the segment surface figure to ensure the segments act as a single surface. There are several other large ground-based segmented telescopes that use active optics including the Hobby-Eberly Telescope, Gran Telescopio Canaritas, the Southern African Large Telescope (SALT), and the Large Sky Area Multi-Object Fibre Spectroscopic Telescope (LAMOST). Figure 14 shows a comparison of telescope primary mirrors.

Research in deployable space telescopes has been ongoing since the 1970s. Research focused on the objective of phasing the telescope segments. This required work in many fields including structures, wavefront sensing, and controls. Lane et al. [9] provides an overview of past research efforts. In the 1980s and 1990s the Lockheed Martin adaptive large aperture technology (ALOT) program demonstrated segmented mirror alignment and wavefront sensing and control technologies. Lockheed Martin also analyzed structural behavior of a segmented primary mirror on the advanced structures and controls integrated experiment (ASCIE). This research informed initial work on the JWST in the mid-1990s.

Technology demonstrations and risk reduction efforts continued into the 2000s. Massachusetts Institute of Technology (MIT) developed a sparse aperture interferometer test bed called Adaptive Reconnaissance Golay-3 Optical Satellite (ARGOS). ARGOS identified the multidisciplinary design challenges of integrating building interferometric array and integrating in a spacecraft simulator [50]. Air Force Research Laboratory (AFRL) also built the Deployable Optical Telescope (DOT) to demonstrate the deployment and calibration of a three-segment telescope.

More recent technology developments include the SMT and NASA UV/EO space telescope work like the Advanced Technology Large Aperture Space Telescope (ATLAST). ATLAST is an 8 to 16-meter ultraviolet optical infrared space observatory [51]. NASA has also proposed concepts to robotically assemble a large segmented telescope on orbit. This resulted in a risk reduction program for ATLAST called Optical Testbed and Integration of ISS experiment (OpTIIX). The OpTIIX program intended to demonstrate on orbit telescope assembly technologies and end-to-end wavefront sensing and control of an optical segmented telescope [52].
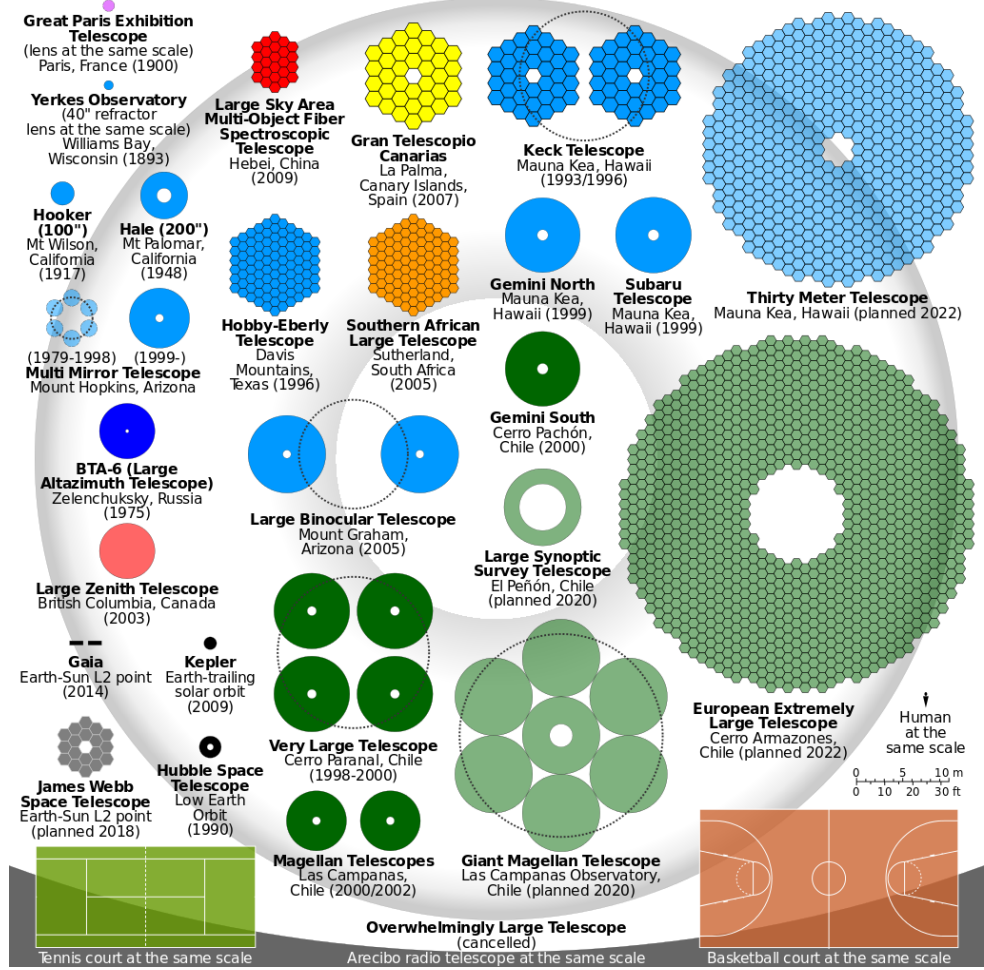
Figure 14. Comparison of telescope primary mirrors, from [53]

2.   SMT Description

The 3-meter 6 segment SMT requires the segment phasing in order for the SMT to operate as a single monolithic mirror. This means that the surface of each mirror segment must align within close proximity of the design prescription. Generally a peak to valley wavefront error of λ/4 is considered phased. The segment surface RMS wavefront error should also have a RMS wavefront error less than λ/15. Phasing the SMT primary mirror requires the SMT actuators, wavefront sensors and a control system.

The 3-meter diameter primary mirror has six hexagonal 1-meter diameter AHM segments with 156 PMN surface parallel face-sheet actuators (FSAs) each.   These actuators correct the surface of the segment. Each segment is aligned using six coarse

28

control actuators (CCAs) and three fine control actuators (FCAs).   Each FCA is connected to a bipod and each leg of the bipod is a CCA. The CCA has a stroke length of +/- 2.8mm with a step resolution of 1.5μm. The six CCAs per a segment act as a hexapod and are used for coarse alignment and phasing. The FCA actuators are PMN actuators like the FSAs. They have a step resolution of less than 1nm and a total stroke of +/- 5μm. The three segment FSAs control segment piston, tip, and tilt. Figure 15 shows the position of the FSAs and CCAs on the segment back structure.
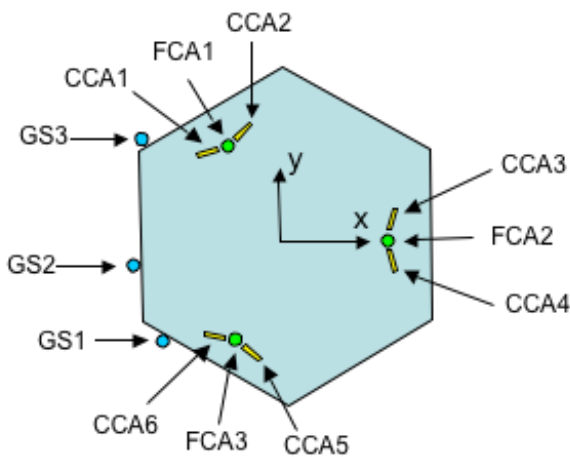
Figure 15. SMT FCA, CCA, and GS locations

Figure 16 shows the SMT optical layout. The SMT has a three-mirror anastigmat optical design. The primary, secondary, and tertiary mirrors all have curvature in order to remove spherical aberrations, coma, and astigmatism. The primary and secondary mirror work similar to a Cassegrain design and the tertiary mirror enables a large system focal length of 60 meters giving a $f_\#$ of 20.   The magnification of the tertiary relay mirror enables the long system focal length.
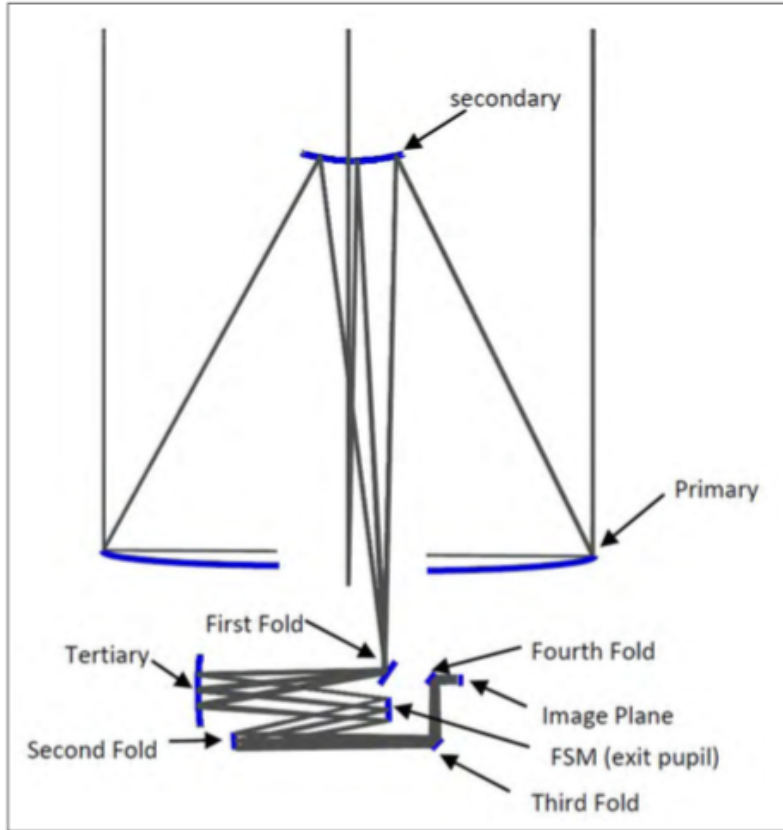
Figure 16. SMT optical layout, from [54]

The satellite field of regard (FOR) is the target area that the telescope can see based on the telescope position, while the field of view (FOV) is the area that the sensor can image within the FOR. The SMT FOR is 0.5 degrees circular and the design provides a full 0.5 x 0.5 degree rectangular FOR. The sensor FOV is 2x2 arc minutes and can only image a small portion of the FOR. The SMT includes a field steering mirror (FSM) at the exit pupil to steer the FOV over the FOR. The FSM also removes mechanical jitter from the optical assembly. Figure 17 shows an example of the SMT FOV within the FOR.
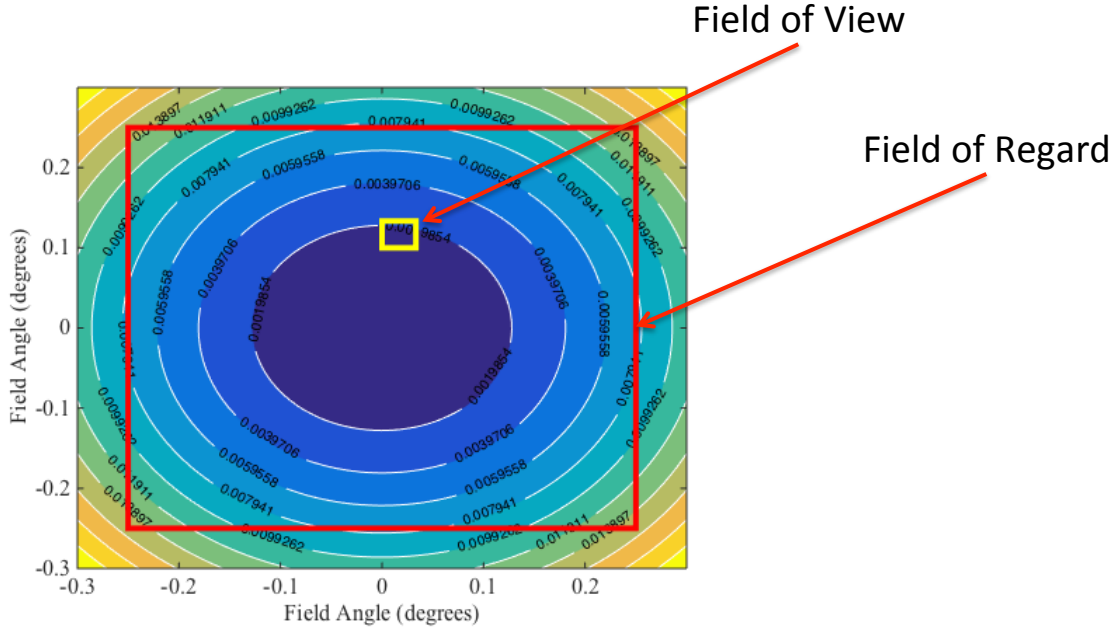
Figure 17. SMT Field of Regard and Field of View

The SMT wavefront sensing system includes edge sensors, jitter sensor, a phase diversity wavefront sensor, and a Shack-Hartmann wavefront sensor. The phase capture range of the sensors varies. The Shack-Hartmann and phase diversity wavefront sensors suffer from a 2π ambiguity, but provide feedback for fine phase control and surface figure control. The edge sensors are not susceptible to the 2π ambiguities and provide feedback for coarse alignment and phasing of the segments. The coarse phasing control approach uses both the edge sensors and the phase diversity sensor data to remove edge sensor bias terms. The SMT edge sensors do not meet design requirements and currently prohibit segment phasing using the existing control architecture.

More recent segmented telescope research introduces wavefront sensing and control techniques including a laser truss metrology system and dispersed fringe sensing [46], [55], [56]. NASA JPL developed laser truss metrology techniques to perform segment phasing in the ATLAST and OpTIIX programs. Figure 18 shows the laser truss metrology concept. A laser truss system measures the full optical state of the telescope at high bandwidth and offers advantages over edge sensors used in the SMT. The system uses laser light to measure the position of the primary, secondary and tertiary mirrors in

31

relation to each other. According to NASA JPL the laser truss system provides better observably of segment rigid body errors, can operate when there is no guide star, provides measurements that support alignment across the full field of view, and can estimate all the required degrees of freedom [55].
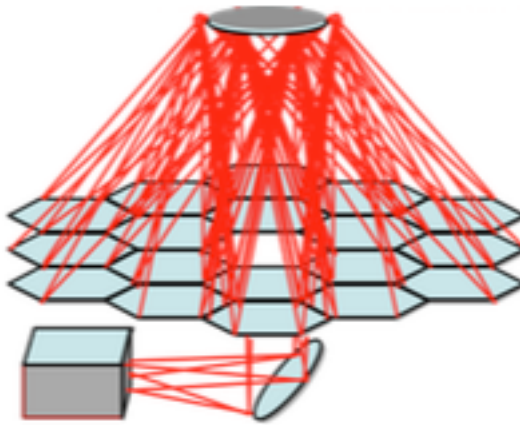
Figure 18. Space telescope laser truss metrology concept, from [55]

3.   SMT State Space Model Background

Analytical modeling of segmented telescopes is necessary to design the wavefront sensing and control system. The control design in this dissertation is based on analytical models developed by Yingling [54], Hom and Bampton [57]. They developed integrated optical-mechanical SMT models resulting in a state space plant model for the SMT. The state space model represents the structural and optical response of the SMT. The state space model inputs include all the actuator inputs and seismic disturbances. The model outputs the optical path difference (OPD) of light at the focal plane array pupil and the displacement of the gap sensors. The OPD output is in the form of a 282 x 282 matrix. The sensor outputs are converted from the OPD output. Table 2 shows the model inputs and sensor outputs. Figure 19 shows the state space model layout.

Table 1.   SMT state space model inputs and outputs

Control Inputs		
Source	Number	per segment
Face Sheet Actuators	936	156
Fine Control Actuators	18	3
Coarse Control Actuators	36	6
Fast Steering Mirror	4	
Seismic	3	
Total	997	
Outputs		
Source	Number	per segment
Shack-Hartmann Sensor	732	122
Phase Diversity Sensor	18	3
Gap Sensor	18	3
Jitter Sensor	2	
Modal States	166	
Total	936	
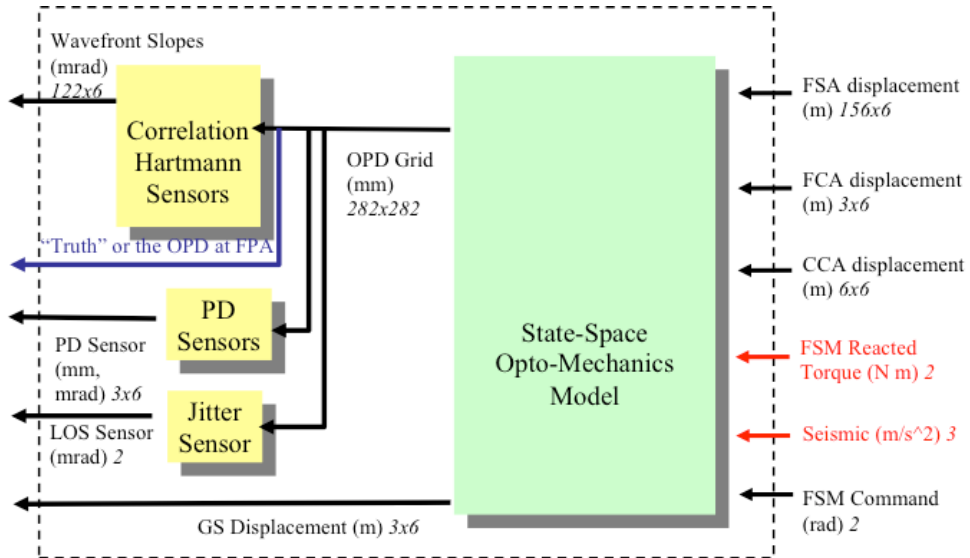
Figure 19. SMT Opto-mechanical state space model flow diagram, from [57]

4. SMT Control Approach

The SMT wavefront sensing and control system is required to move the segments from their post deployment un-phased positions to their operational diffraction limited position. The initialization process begins after telescope deployment and improves the wavefront error from several millimeters to below the diffraction limit. The three-wavefront sensing and control modes are coarse segment alignment, coarse phasing, and fine phasing. The coarse segment alignment mode identifies the segment on the camera focal plane and moves the segment to center of the field reducing the alignment error from millimeters to micrometers. The coarse phasing mode co-aligns the segments resulting in a wavefront error of less than a wavelength. The fine phasing mode uses the phase diversity sensor and FCAs to adjust segment piston, tip/tilt, and uses the Shack Hartmann wavefront sensor to reduce the wavefront error of the segment using the FSAs. Table 2 shows the developer's SMT control loops, the associated inputs and outputs, and the phasing mode they support. The SMD program did not demonstrate a real-time high-bandwidth closed loop control system [58].

Table 2.   SMT control loops

Control Mode	Controller	Sample Rate (Hz)	Inputs	Outputs
Coarse Alignment	Bipod Offload	0.1	Gap Sensor	CCAs
Coarse Phasing	Segment Rigid Body	1000	Gap Sensor, Full Aperture Phase Diversity	FCAs
Fine Phasing	Segment Shape	200	Shack-Hartmann	FSAs
	Phase Diversity	1	Phase Diversity Sensor	FCAs

The initialization process brings the segments into phase and reduces the primary mirror surface wavefront error. The telescope points toward a coherent light source reference like a star. The initialization process also establishes the relative set point conditions for the edge sensors. The maintenance control takes place during mission

operations and uses the CCAs, FCAs, edge sensors, and phase diversity sensor to maintain the segment phasing using a closed loop controller. The edge sensors provide high bandwidth relative positions of the segments while the phase diversity sensor provide low bandwidth absolute reference to correct for edge sensor bias and drift using a Kalman filter. The FSAs are designed to hold the segment shape for extended periods of time allowing the segment shape to be updated periodically during calibration opportunities.

The SMT control system also compensates for jitter using a fast steering mirror and a jitter beacon. The fast steering mirror is also the field steering mirror (FSM). The FSM is placed in a common path with the imaging sensor and compensates for wavefront tip and tilt. The FSM control loop is operates at 1kHz.

E. SMT RESEARCH AT NAVAL POSTGRADUATE SCHOOL

Segmented mirror telescope research at the Naval Postgraduate School has included both analytical and experimental work by students, staff researchers, and external organizations. The development of a segmented mirror space telescope is a multi-disciplinary effort. Past areas of research include controls, structures, vibrational analysis, segmented telescope design, and wavefront reconstruction. Key works that inform this dissertation are surveyed below.

Past SMT control research was conducted analytically with some experiments using test beds other than the SMT. Burtz [59] applied a multi-input multi-output (MIMO) H_∞ controller to a flexible segmented space telescope dynamic model that included model reduction techniques to reduce computer simulation complexity. The control technique was experimentally tested using an adaptive optics test bed. The work by Burtz was continued by Looysen [60] who combined H_∞ control techniques with low pass filters to improve plant stability.

Several researchers have addressed the computational burden of a large MIMO control problem and complex structural model. Nagashima and Agrawal [61] reduced the model dimensions by decoupling the dynamic and static portions of the telescope plant using a sensitivity decoupling method. They applied an H_∞ controller to the new

plant and showed improved performance compared to the uncoupled plant. Axtell [62] developed a wavelet reconstruction technique to improve the computational efficiency for systems with many sensor outputs like the SMT. Dras, Jennings, and Cobb's [63] developed a reduced order model for the SMT. They experimentally validated the model using SMT vibration data enabling faster model tuning and analysis.

In addition to controls and wavefront reconstruction researchers developed opto-mechanical design techniques and performed detailed structure and vibration analysis. Yingling [54] developed an integrated opto-mechanical design method resulting in a model that was experimentally validated using the SMT. Yingling's model is the basis for the models developed in this research. Yingling also added tuned mass dampers to the SMT to reduce structural disturbances allowing improved experimental controls research in this dissertation.

Most recently Watson and Bagnasco's [64], [65] added pupil relay optics and a deformable mirror the SMT experimental setup. This work provided a starting point for the experimental woofer-tweeter research in this dissertation.

This dissertation builds on previous research in segmented mirror telescopes, adaptive optics, wavefront sensing, and control. This dissertation responds to the residual surface error of lightweight active mirrors by offering control techniques to compensate for the residual surface errors using an additional deformable mirror in a woofer-tweeter configuration. The control approaches are specific to a space telescope application, and the simulation and experimental results are demonstrated using an AHM.

III. SPACE TELESCOPE WOOFER-TWEETER MODEL

In preparation for the development of space telescope woofer-tweeter control techniques this chapter presents the segmented telescope, deformable mirror, and woofer-tweeter analytical models. This requires understanding the SMT woofer-tweeter design assumptions and an understanding of the SMT design. The SMT design drives several trades when determining the size and placement of the deformable mirror in the optical path. The chapter provides a design recommendation based on the assumptions and design drives which informs the development of the woofer-tweeter model. The chapter begins by presenting design assumptions and design drivers for the optical configuration. Next the chapter describes the placement of the deformable mirror. Then the chapter describes analytical models of the surface error, the SMT, the deformable mirror, and the woofer-tweeter system.

A. DESIGN ASSUMPTIONS

Three key assumptions are made when designing the SMT woofer-tweeter system. The first assumption is that wavefront disturbances are low frequency allowing the two mirrors to operate at the same bandwidth. The second assumption is that the optical layout only requires one wavefront sensing system. The third assumption is that the SMT segment edges are already phased prior to woofer-tweeter fine phasing. These assumptions are discussed further below.

1. Disturbance Bandwidth

The purpose of the proposed space telescope woofer-tweeter system is to correct primary mirror static residual errors, and low bandwidth disturbances. O'meara, Swigert, and Brown noted that surface figure control of an orbiting telescope is different from a ground-based telescope based on the frequency of the error sources [17]. This allows the two mirrors to operate at the same bandwidth unlike a woofer-tweeter atmospheric compensation system where the mirrors correct disturbances at different temporal frequencies requiring the woofer and tweeter to operate at different bandwidths [66]–[68].

2. Wavefront Sensing Approach

In order to simplify design and controls the wavefront sensing system measures the combined effects of the primary segmented mirror and the tweeter deformable mirror. The wavefront sensing system assumes that the incoming light is coherent and that the only source of wavefront error is from the primary mirror and deformable mirror. This single output approach allows a relationship between the woofer-tweeter inputs and the measured output.

3. Segment Phasing Assumption

The proposed woofer-tweeter system improves the telescope fine phasing by improving the surface figure error of individual primary mirror segments. This requires that the individual segments already be phased relative to each other. In order to preserve actuator stroke and prevent actuator saturation the woofer-tweeter control system does not compensate for piston, tip, and tilt. Any residual segment piston, tip or tilt error is removed using the segment FCAs.

B. DESIGN DRIVERS

The optical design of the SMT drives the proposed woofer-tweeter design. This section discusses two key design considerations when adding a deformable mirror to the optical telescope. The first is the fact that the SMT has a steerable FOV and the second consideration is the impact of field angle magnification based on the size of the exit pupil and deformable mirror size.

1. SMT Field Steering

The SMT is a steerable field of view system where the telescope has a wide FOR and the sensor has a smaller FOV. The telescope uses the FSM located at the exit pupil to steer the FOV within the telescope FOR. In order for the telescope to perform well at all FOV locations the wavefront error due to the primary mirror must be corrected at all field angles. This may require the deformable mirror to update the correction based on the telescope FOV setting.

The logical place to make this correction is at the exit pupil because all the field angles are present and it is conjugate to the primary mirror. However, the SMT exit pupil location is already occupied by the FSM. A design trade is discussed in a later section to determine the best place to locate the deformable mirror.

2. Field Angle Magnification

The next consideration is field angle magnification. The current SMT exit pupil is de-magnified to a diameter is 150mm, or 20x. This has the effect of magnifying the field angles due to the Lagrange invariant. The Lagrange invariant relates the ray height and angle for all rays as they propagate through an optical system, Equation (3.1). The variable D_{PM} is the diameter of the primary mirror and the variable θ_{PM} is the field angle at the primary mirror. The variable D_{DM} is the diameter of the deformable mirror and the variable θ_{DM} is the field angle at the deformable mirror. If the pupil plane is de-magnified the field angles magnify and the surface error correction becomes more difficult at the exit pupil. Therefore the field angle magnification must be taken into account when selecting the size of the deformable mirror and size of the exit pupil. Equation (3.2) shows the relationship between the field angle at the exit pupil, and the field angle at the primary mirror in terms of angular magnification where M_α is the magnification factor.

$$D_{PM}\theta_{PM} = D_{DM}\theta_{DM} \tag{3.1}$$

$$\theta_{DM} = M_\alpha \theta_{PM} \tag{3.2}$$

McComas [69]–[71] studied the field angle magnification effect and proposed a conceptual configurable adaptive optics system that could correct for on-orbit aberrations and field of view wavefront errors. He reviewed the narrow field of view theory and the limitations of narrow field of view theory using a wide FOV system. Equation (3.3) describes the residual wavefront error after the deformable mirror for a narrow FOV system. The variable $\omega_R(x,y;t)$ is the residual wavefront error, $\omega(x,y;t)$ is the wavefront error from the primary mirror incident on the deformable mirror at angle θ_0, and $d_m(x,y;t)$ is the deformable mirror correction. This assumes the wavefront entering the telescope is perfect, only the primary mirror contributes error, and the primary and deformable mirror are conjugates.

$$\omega_R(x,y;t) = \omega(x,y;t) - \frac{4\pi}{\lambda}\cos(\theta_0)d_m(x,y;t) \tag{3.3}$$

McComas reformulated the above equation in terms of optical path length, $\phi(x,y)$, and includes both field angle at the primary mirror and angular magnification due to the Lagrange invariant. The OPD is shown in equation (3.4) where $d_{PM}(x,y)$ is the surface height of the primary mirror, $d_{DM}(x,y)$ is the surface height of the deformable mirror, and θ_{PM} is the field angle at the primary mirror. The result of equation (3.4) is that a deformable mirror may not be able to correct all the field angles because as the term $M_\alpha\theta_{PM}$ approaches $\pi/2$ the deformable mirror cannot compensate.

$$\phi_R = 2d_{PM}(x,y)\cos(\theta_{PM}) - 2d_{DM}(x,y)\cos(M_\alpha\theta_{PM}) \tag{3.4}$$

The SMT has a FOR of 0.5 degrees and an angular magnification of 20. Figure 20 shows that the relative path length error at varying field angles assuming a primary mirror displacement of one wave. The path length error is relatively small because the deformable mirror is the same size as the exit pupil and both the FOR and magnification are small.

However, if a smaller diameter deformable mirror is used the exit pupil requires de-magnification. For example, a commercially available 25mm diameter MEMs deformable mirror requires us to de-magnify exit pupil diameter by an additional factor of six resulting in a field angle magnification of 120 at the deformable mirror. Figure 21 shows the increased angular magnification substantially increases the off-axis path length error. The deformable mirror can still compensate for the primary mirror at off axis FOV locations, but requires more actuator stroke.

The two angular magnification examples show how the Lagrange invariant is a design driver when choosing a deformable mirror. In both examples the term $M_\alpha\theta_{PM}$ does not approach $\pi/2$ over the FOR and the deformable mirror can compensate for field angle magnification at the edge of the FOR. However the mirror stroke must be sized for the anticipated primary mirror surface error and the field angle magnification at off axis FOV locations.

The Lagrange invariant impacts the deformable mirror wavefront control system. In the 20x magnification example the optical path length contribution due to the Lagrange invariant can be ignored because the error contribution is minimal. However, the deformable mirror needs to update correction to account for the Lagrange invariant at off axis FOV locations in the 120x magnification case. This is accomplished by including the field angle in the deformable mirror controller. Figure 20 shows the relative path length error for different field angles given a field angle magnification of 20. The contours represent the additional wavefront error at the deformable mirror for a single wave of error at the primary mirror. Figure 21 shows the relative path length error for different field angles given a field angle magnification of 120. The yellow box represents the field of view and the red box represents the field of regard.

Field angle magnification at the DM also complicates the design of the optical system after the deformable mirror. The optical components between the exit pupil and image plane must handle the magnified field angles. Optical designs become more complex and require additional components to remove large field angle aberrations.
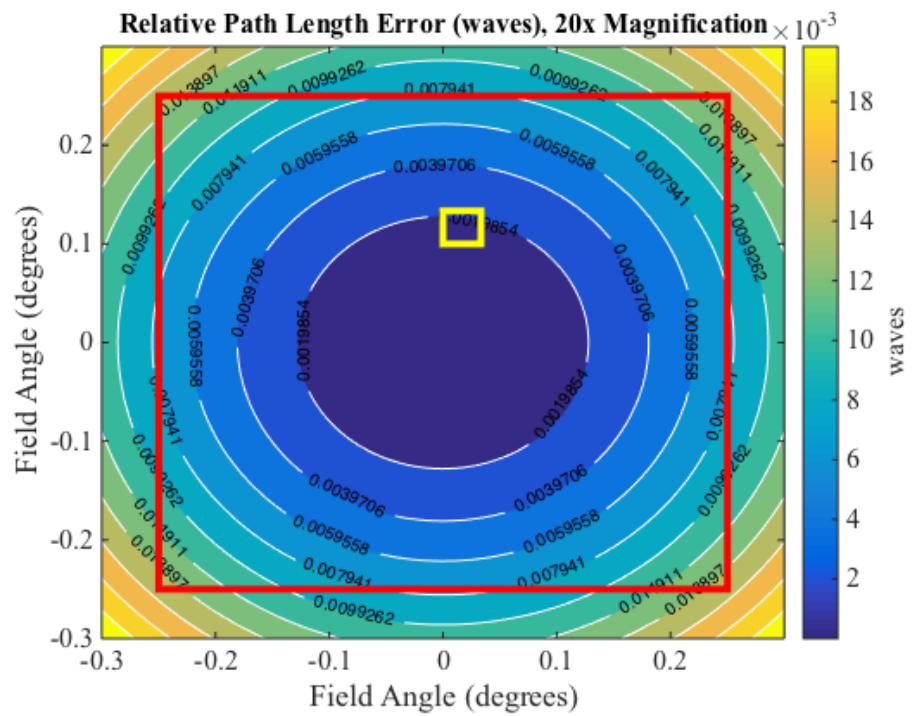
Figure 20. Relative path length error (waves) for 20x angular magnification
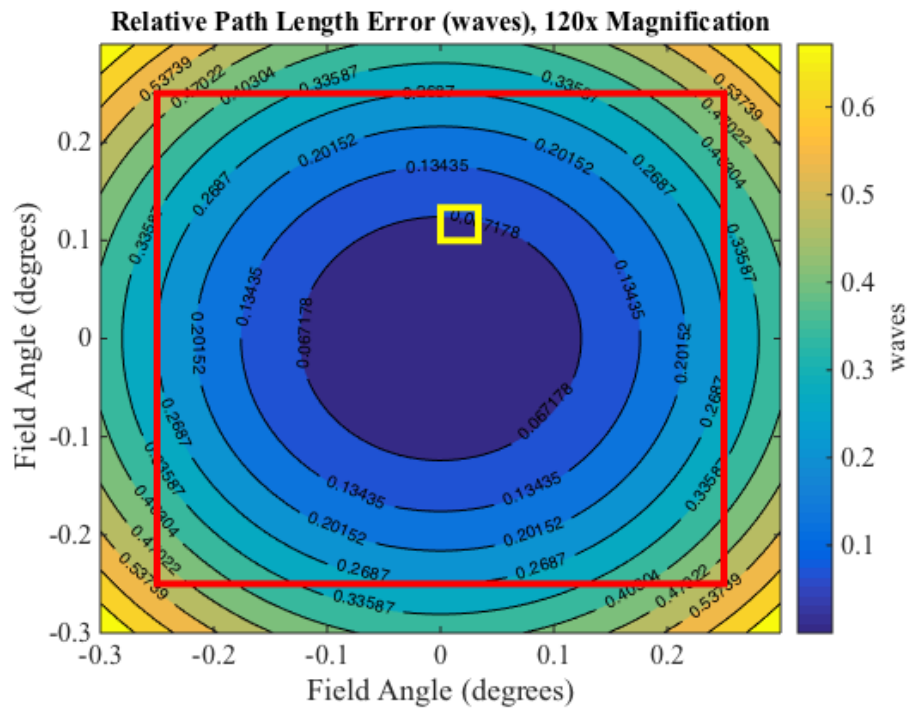
Figure 21. Relative path length error (waves) for 120x angular magnification

42

C.   PLACEMENT OF DEFORMABLE MIRROR

This section presents two possible configurations for the addition of a deformable mirror to the SMT. Option one replaces the FSM with a deformable mirror on a gimbal. Option two adds an optical relay and uses a smaller diameter deformable mirror. The first option is selected for this research because the effects of field angle magnification are relatively small. Both configurations are presented below to provide context for the selected option, and because the second option can be implemented in future work using a commercial deformable mirror.

The natural placement of the deformable mirror in the SMT optical design is at the exit pupil since the exit pupil is conjugate with the entrance pupil. However, the FSM currently resides at the exit pupil requiring the optical design to be modified. This position requires the deformable mirror size to match the exit pupil diameter, 150 mm. The FSM functionality can be maintained by placing the DM on a gimbal at the exit pupil location. Figure 16 shows the optical layout of the SMT and Figure 22 shows the proposed DM location.
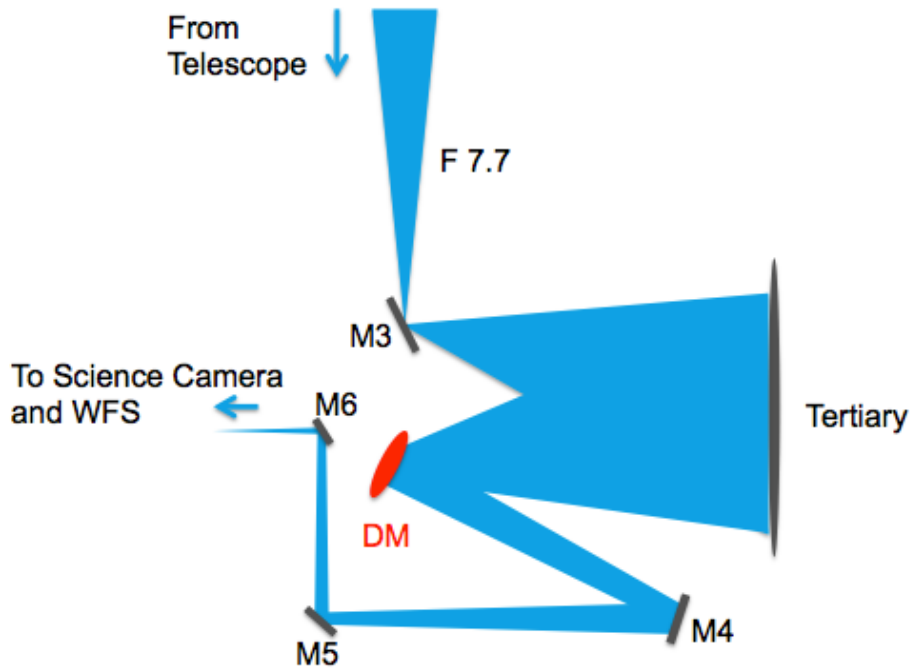
Figure 22. SMT optical layout replacing the FSM with a deformable mirror on a gimbal, from [72]

The second option relays and reduces the size of the exit pupil to accommodate a small deformable mirror. This option reduces the changes to the SMT optical layout and adds a pupil relay and deformable mirror after the FSM and after the last fold mirror, M6. This approach can match the exit pupil size to a small commercially available deformable mirror and allow use of the existing wavefront sensing system and science camera. Although the increased exit pupil de-magnification increases the field angles at the deformable mirror the proposed option can demonstrate a proof of concept using the SMT. Figure 23 shows the proposed optical layout and Figure 24 shows the details of the optical relay. The biggest challenge to this option is incorporating the optical relay into the back optics of the SMT.
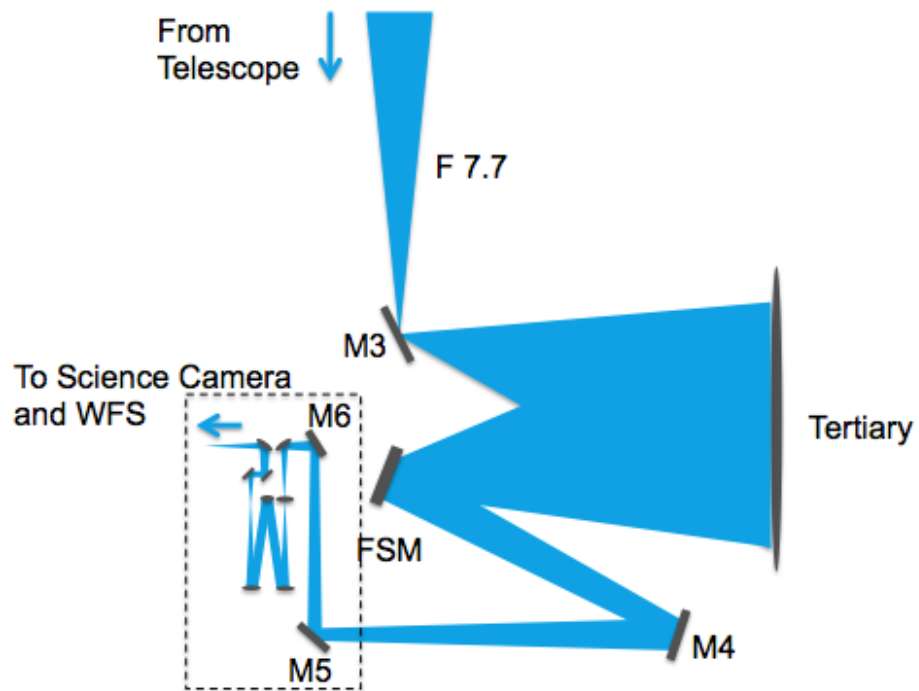
Figure 23. SMT with deformable mirror optical relay and pupil size reduced, from [72]
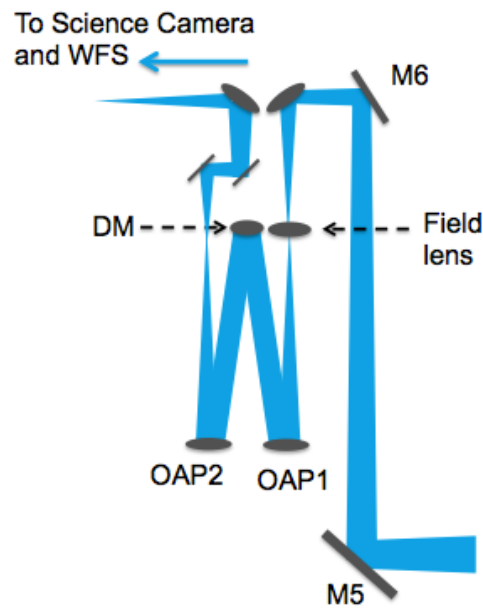
Figure 24. Layout of SMT pupil optical relay with deformable mirror, from [72]

D.   RESIDUAL WAVEFRONT ERROR MODELING

This section presents the residual error of a single SMT AHM segment used throughout this research. To demonstrate the breadth of application the residual error of the CFRP mirror mentioned in the background is also presented. These errors are representative of the residual errors found in large lightweight primary optics and include print-through, fixture error, and low order aberrations. The residual errors identified in these mirrors are used to create a generalized residual error model that can be used to simulate hypothetical primary mirror residual surface errors.

The residual wavefront error is represented as the optical path difference (OPD) from a flat wavefront. Assuming the light entering the telescope is coherent, the OPD corresponds to the phase shift of the wavefront as it passes through the imperfect optics of the telescope. The telescope residual wavefront error is measured as a two-dimensional OPD at the exit pupil.

1.   SMT AHM Residual Error

The SMT AHM segment provides a reference for expected residual surface error. Figure 25 shows the measured OPD of SMT segment 3. The RMS wavefront error is approximately 0.32 waves at 632.8 nm after applying a closed loop controller to reduce the wavefront error. The SMT residual error contains high spatial frequency print-through error caused by the segment ribs and low spatial frequency error caused by fine control actuator attachment points and mirror defects [16]. A two-dimensional Fourier transform of the SMT residual wavefront error identifies the prominent spatial frequencies. Figure 25 shows the Fourier transform log plot and the dominant spatial frequencies are below 25 cycles/aperture.
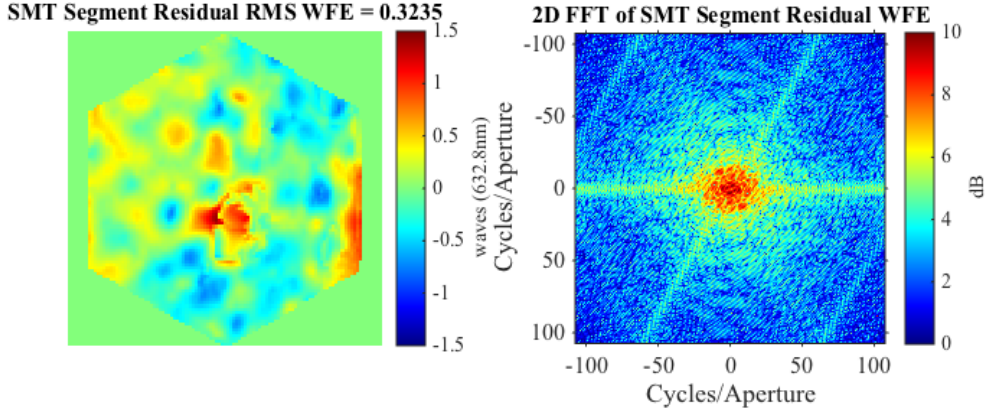
Figure 25. SMT segment residual OPD (left), two-dimensional FFT log plot of SMT residual surface error (right), from [16]

2.   Carbon Fiber Reinforced Polymer Mirror Residual Error

The 1-meter CFRP mirror developed by CMA provides a reference of expected surface error for a large CFRP mirror. The mirror has troubled areas on the surface due to manufacturing defects. For example, the center core of the substrate failed when the mirror was removed from the mandrel. The mirror is characterized using a Zygo interferometer. Figure 26 shows the measured OPD with piston, tip, and tilt removed. The interferometer measurements have dropouts in the center and in the top right quadrant due to manufacturing defects. The hexagonal back structure is also apparent as print through.
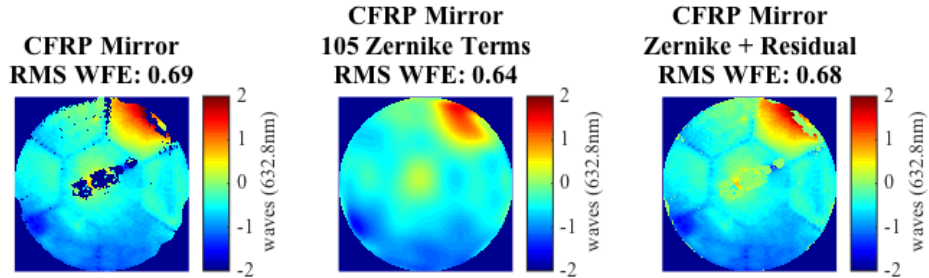
Figure 26. CFRP measured (left), CFRP Zernike fitted (center), CFRP Zernike fitted plus residual wavefront error from measurement (right).

The CFRP mirror is modeled by fitting the measured data to Zernike polynomials. This gives a good approximation of the mirror surface and fills in the discontinuities due to the interferometer dropouts. The difference between the fitted Zernike surface and the measured surface is found and the difference is added to the fitted surface. This provides a continuous model of the CFRP surface error to develop deformable mirror models to fix the residual surface error.

3.   Generalized Residual Error Model

This section presents a model developed to simulate the residual error of a hypothetical large aperture lightweight mirror. The model outputs a 2D OPD that has characteristics similar to current replicated primary mirror aberrations including low order aberrations, print through, and fixture error. The print through geometry is determined by the rib structure of the mirror substrate. The model can include hexagonal ribs or rectangular ribs, and can vary the number of ribs in the support structure to generate print-through in the OPD. Figure 27 shows an example of a simulated OPD for a hexagonal segment with hexagonal ribs, three fixture points, and astigmatism. Figure 28 shows a simulated OPD for a circular aperture with rectangular ribs. This model can be used to predict the number of tweeter actuators and actuator spacing to remove the surface errors.
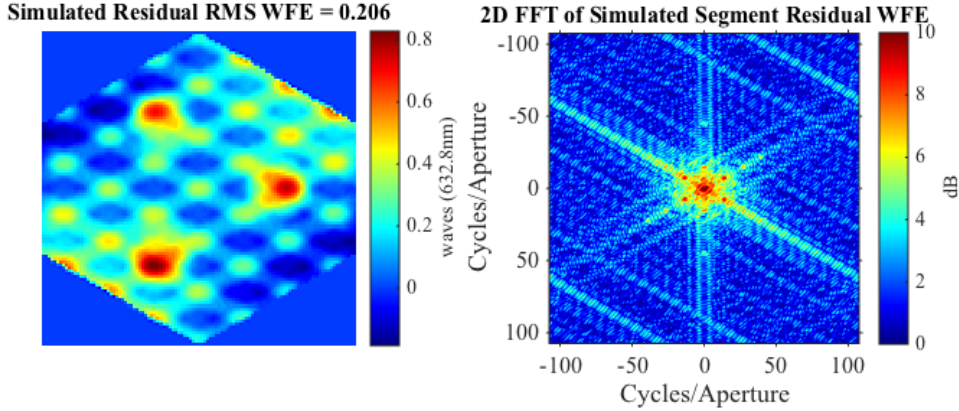
Figure 27. Simulated OPD of hexagonal mirror with hexagonal print through error, fixture error, and astigmatism (left), two-dimensional FFT log plot of simulated residual surface error (right)
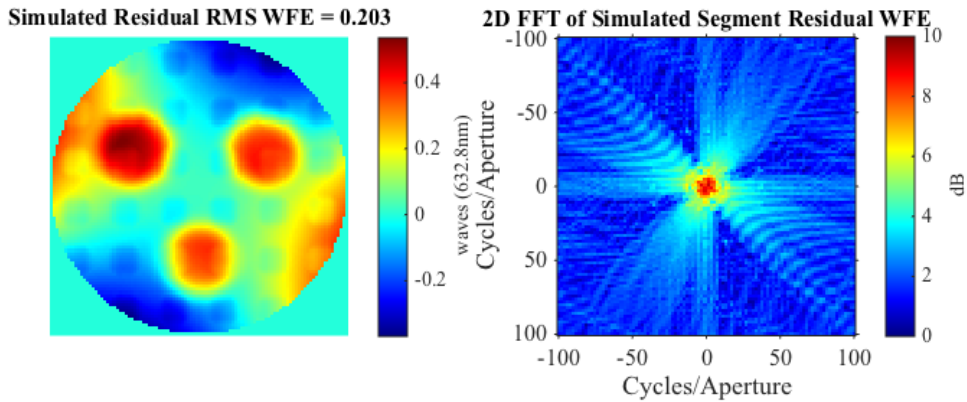
Figure 28. Simulated OPD of circular mirror with rectangular print through error, fixture error, and astigmatism (left), two-dimensional FFT log plot of simulated residual surface error (right)

E.   SMT MODEL DEVELOPMENT

This section describes the SMT model development and includes background on the original SMT state space model. The SMT model is based on the 2nd order MIMO state space model developed by the Lockheed Martin and updated by Yingling [54]. This section describes the addition of actuator and sensor modeling as well as the development of a state feedback observer used to estimate the states from the sensor outputs.

49

1.   State Space Model

The SMT optical telescope assembly includes the control system as part of the optical prescription. The state space model developed by Hom, Bampton [57], and later updated by Yingling [54] is a starting point for the research in this dissertation. The state-space model represents the structural and optical response of the telescope and includes the flexible dynamics of the six segments and the payload support structure. The models primary outputs are a 2-dimensional 282 x 282 OPD at the exit pupil plane and the edge sensor displacement of the segments relative to the SMT structure. The model secondary outputs are the wavefront sensor outputs. Sensor outputs matrices convert the OPD to Shack-Hartmann slope measurements, and phase diversity piston and slopes measurement. Table 1 presented earlier in this chapter summarizes the model inputs and outputs.

The state space model inputs and outputs reference either a local or global coordinate system. The global coordinate system is with respect to the center of telescope aperture. The local coordinate system is centered at each segment with the x-axis pointing radially away from the center of the telescope. Figure 29 and Figure 30 show the SMT global and local coordinate systems.
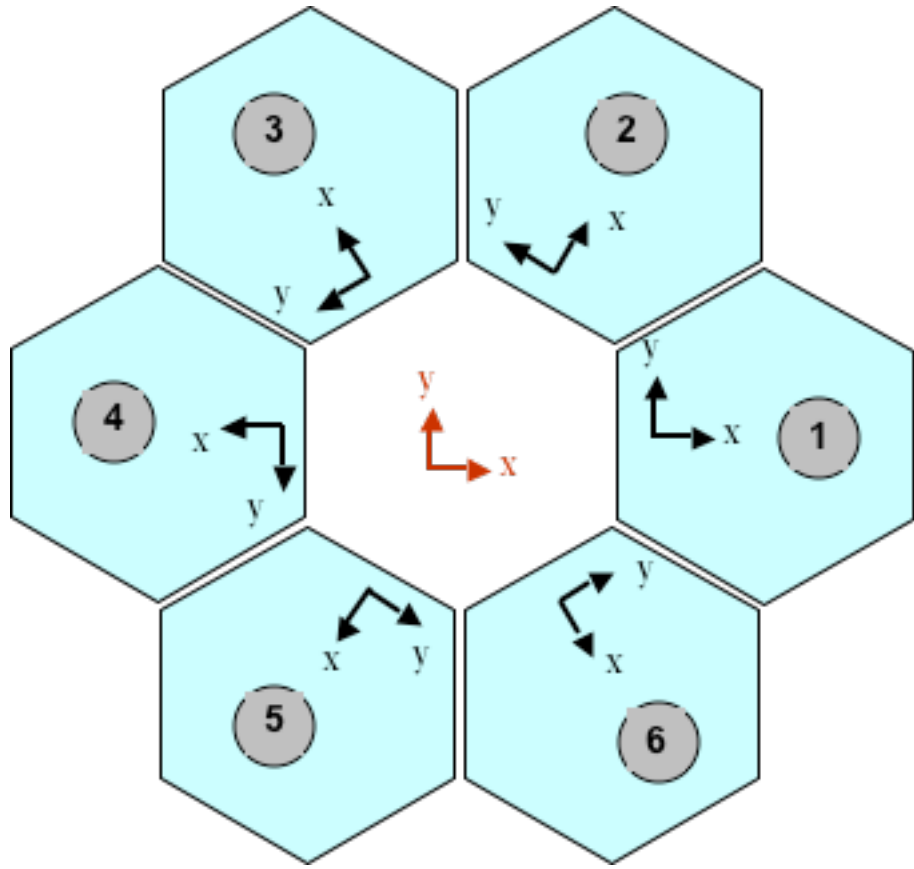
Figure 29. SMT global (red) and local coordinate systems, the z-axis points toward the observer, from [57]
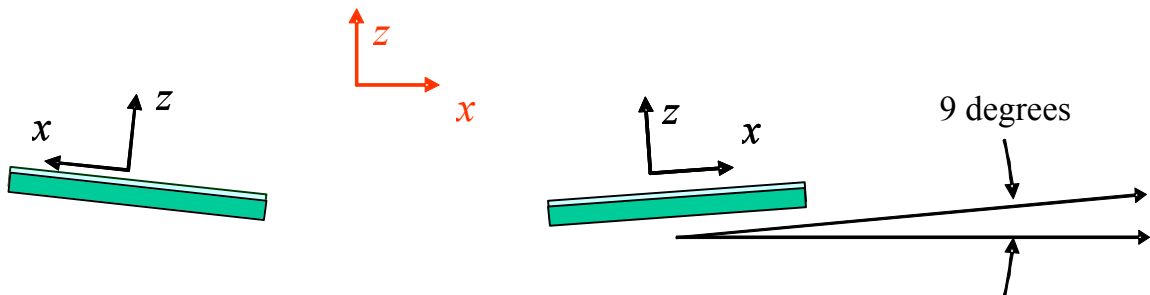
Figure 30. SMT global (red) and local (black) coordinates viewed from the side, from [57]

Hom, Bampton, and Yingling used finite element models (FEMs) of the segment and optical telescope assembly (OTA) to create a segment and an OTA state space models. To reduce model computational complexity they extracted eigenmodes within the frequency band of interest from the FEMs and truncated the high frequency modes.

They identified the truncated high frequency modes to the segment FSAs response. To capture the FSA modes they augmented the eignemodes with additional residual modes. They then built a second order state space model from the FEMs represented by A, B, C, and D matrices, Eq (3.5).

$$\left\{ \begin{array}{c} \dot{x} \\ y \end{array} \right\} = \left[\begin{array}{cc} A & B \\ C & D \end{array} \right] \left\{ \begin{array}{c} x \\ u \end{array} \right\} \tag{3.5}$$

Generalized modal coordinates represent the states, Equation (3.6). Equation (3.7) shows the structure of the A matrix where A_{11} is a zero matrix, A_{12} is an identity matrix, A_{21} and A_{22} are diagonal matrices, equations (3.10) and (3.11), of modal frequencies where ω_i is the frequency and ξ_i is the damping ratio of the ith mode.

$$\{x\} = \left\{ \begin{array}{c} q \\ \dot{q} \end{array} \right\} \tag{3.6}$$

$$[A] = \left[\begin{array}{cc} A_{11} & A_{12} \\ A_{21} & A_{22} \end{array} \right] \tag{3.7}$$

$$A_{11} = [0] \tag{3.8}$$

$$A_{12} = [I] \tag{3.9}$$

$$A_{21} = \left[\begin{array}{cccc} -\omega_1^2 & 0 & \cdots & 0 \\ 0 & -\omega_2^2 & \cdots & 0 \\ \vdots & \vdots & \ddots & \vdots \\ 0 & 0 & \cdots & -\omega_n^2 \end{array} \right] \tag{3.10}$$

$$A_{22} = \left[\begin{array}{cccc} -2\zeta_1\omega_1 & 0 & \cdots & 0 \\ 0 & -2\zeta_2\omega_2 & \cdots & 0 \\ \vdots & \vdots & \ddots & \vdots \\ 0 & 0 & \cdots & -2\zeta_n\omega_n \end{array} \right] \tag{3.11}$$

Equation (3.12) shows the structure of the B matrix. B_1 is a zero matrix and B_2 represents the mode shapes at the actuator locations. Equation (3.13) shows the C matrix structure where C_1 represents the modes shapes at the sensor locations and C_2 is a zero matrix. The D matrix is nominally a zero matrix because the states only change due to structural interactions [54].

$$[B] = \left[\begin{array}{c} B_1 \\ B_2 \end{array} \right] \tag{3.12}$$

$$[C] = \left[\begin{array}{cc} C_1 & C_2 \end{array} \right] \tag{3.13}$$

Representing the high frequency FSA modes statistically further reduced complexity of the state space model. This was accomplished by representing the residual modes associated with the segment FSAs as static influence functions. The influence functions were removed from the dynamic model and represented using the D matrix. The B matrix then represents only normal mode sensitivity to specific actuator input and the C matrix represents the normal modes shapes. The dynamic state space model from equation (3.5) is rewritten into two state space equations below.

$$\{\dot{x}(t)\} = [A]\{x(t)\} + [B]\{u(t)\} \tag{3.14}$$
$$\{y(t)\} = [C]\{x(t)\} + [D]\{u(t)\} \tag{3.15}$$

A static influence matrix model from the dynamic model is found by assuming a steady state response, $\{\dot{x}(t)\} = 0$. Substituting equation (3.16) into equation (3.17) directly relates the inputs to the measured output. The matrix Γ is the analytical influence matrix from the static model. The static model is used in cases where the telescope structural dynamics are slow compared to the FSA response. An example is a case of thermal disturbances where the dynamics are slow allowing and structural dynamics are neglected while controlling the face sheet actuators. This quasi-static approach simplifies the control of the segment face sheets as long as the bandwidth is low frequency; $f \ll 1Hz$ [54].

$$0 = [A]\{x(t)\} + [B]\{u(t)\} \Rightarrow \{x(t)\} = -[A]^{-1}[B]\{u(t)\} \tag{3.16}$$
$$\{y(t)\}_{Steady\_State} = [C]\{x(t)\} + [D]\{u(t)\} = -[C][A]^{-1}[B]\{u(t)\} + [D]\{u(t)\} \tag{3.17}$$
$$\Gamma = [D] - [C][A]^{-1}[B] \tag{3.18}$$
$$\{y(t)\} = \Gamma\{u(t)\} \tag{3.19}$$

2.   Actuator Models

MathWorks Simulink is used to perform computer simulation of the state space model and quasi-static state space model. The state space opto-mechanical model models the structural dynamics of the SMT. Time delays and noise are added to the CCA, FCA, FSA, and FSM inputs of the opto-mechanical model to simulate the actuators. The FSM torque inputs to the optical mechanical model are found by using an additional 2nd order model and the jitter sensor inputs. The state space model is updated to include the plant noise where $\{v(t)\}$ is the plant noise and [G] is the noise gain matrix.

$$\{\dot{x}(t)\} = [A]\{x(t)\} + [B]\{u(t)\} + [G]\{v(t)\} \tag{3.20}$$

3.   Sensor Models

The jitter sensor model uses the OPD output matrix and a jitter matrix to compute the jitter outputs. The outputs are the x and y slopes measured in radians of the OPD in global coordinates. These outputs combine with the FSM reaction torques in the x and z moments and the FSM angle commands in the x and z rotations both in global coordinates to control the FSM.

The SMT Shack-Hartmann wavefront sensor model converts the OPD output to Shack-Hartmann wavefront sensor outputs by multiplying the OPD output matrix by the wavefront sensor matrix, WFS. This matrix multiply approximates the gradient of the wavefront measured by the Shack-Hartmann wavefront sensor. Each segment has 61 lenses that produce 61 slopes measurements in the x direction and 61 slope measurements in the y direction. The WFS matrix multiply approximates the slopes using central differencing based on the location of the lens on the OPD in both the x and y direction. Equations (3.21) and (3.22) find the slopes from the OPD given the displacement values at pixels i and j. The pixels i and j correspond to the Shack-Hartmann lens locations superimposed on the OPD, Figure 31.

$$S_x(i,j) = \frac{OPD_{i+1,j} - OPD_{i-1,j}}{2\Delta x} \tag{3.21}$$

$$S_y(i,j) = \frac{OPD_{i,j+1} - OPD_{i,j-1}}{2\Delta y} \tag{3.22}$$

The Shack-Hartmann wavefront sensor provides a large capture range of the segment surface figure, but cannot determine segment piston error.   The lenslet developed for the SMT only has 61 lenslets per a segment. There are fewer lenslets than actuators and high order surface aberrations cannot be measured. Figure 31 shows the Shack-Hartmann lens locations overlaid on a SMT segment with the face sheet actuator locations represented by red dots. This sensor can initially correct the surface figure and the phase diversity wavefront sensor supports fine surface figure control.

54
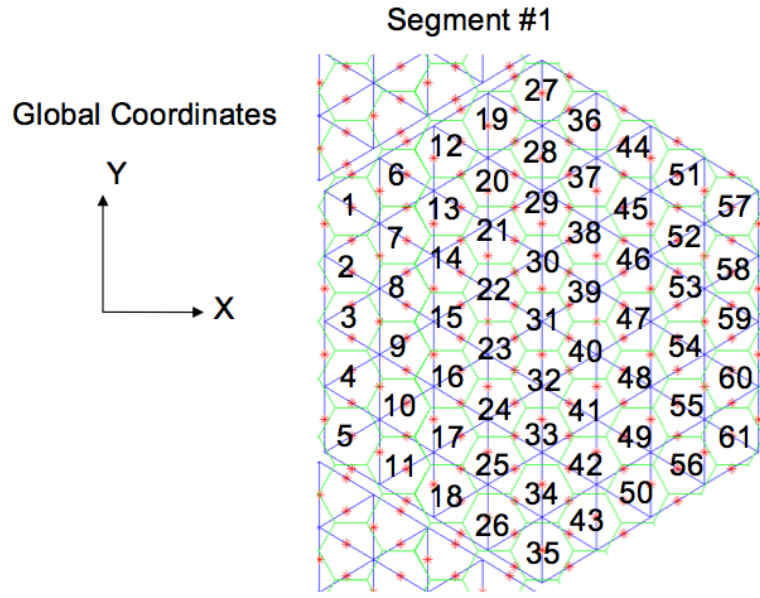
Figure 31. Shack-Hartmann wavefront sensor lens locations on single SMT segment, from [57]

The SMT phase diversity sensor model computes the local segment tip, tilt, and piston from the OPD output using a matrix multiply. This approach simplifies the model by not simulating the phase retrieval process. However, the phase diversity sensor can retrieve the entire phase of the wavefront and not just tip, tilt, and piston. The model is updated to include a phase retrieval algorithm. To generate a point-spread function at the image plane the OPD output is used. Defocus is added to the image to use the Gerchberg-Saxton routine to retrieve the phase. Figure 32 shows a phase retrieval example. The top row is generated from the state space model output OPD, the second row is the estimated point spread function and pupil estimate using a phase retrieval algorithm, and the third row is the difference between the estimate and the model output. The sensor models output both the sensor data and include wavefront reconstruction. The model outputs the reconstructed wavefront as an OPD image and modal coefficients.
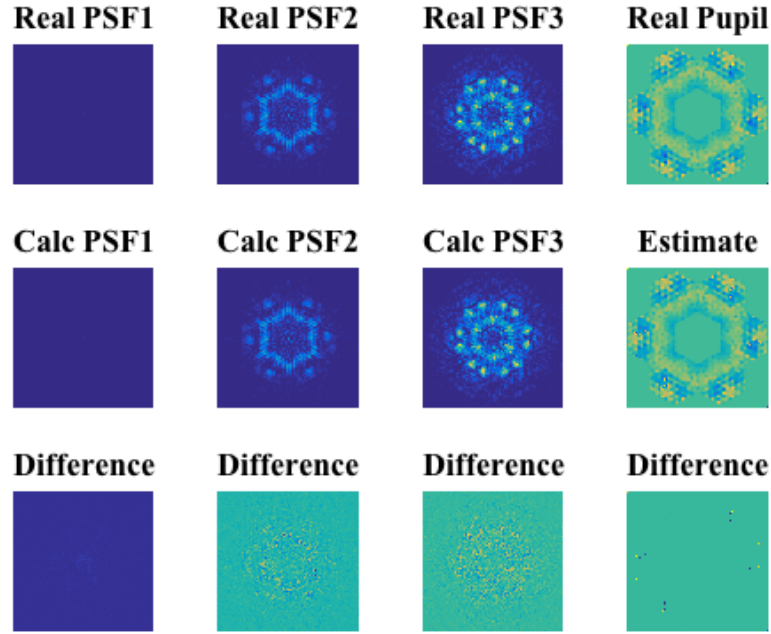
Figure 32. Example of phase retrieval from OPD using
Gerchberg-Saxton algorithm

The sensors are further modeled by adding noise and a time delay to the Simulink model. Gaussian readout noise is added to the OPD output to simulate sensor noise in the Shack-Hartmann wavefront sensor. Similarly Gaussian readout noise is added to the PSF images in the phase diversity sensor simulation. To simulate the sensor bandwidth time delays are added to the sensor output. The output state equation is updated to include measurement noise shown below where $\{w(t)\}$ is the measurement noise and $[H]$ is the measurement noise gain.

$$\{y(t)\}=[C]\{x(t)\}+[D]\{u(t)\}+[H]\{w(t)\} \tag{3.23}$$

4.   Observer

A full state observer estimates the state variables based on the measurements of the sensor model outputs and the control variables. The observer in this model uses modal coefficients sensor outputs to represent the reconstructed OPD. The state variables of the state space model are generalized modal coordinates and the output is the OPD. The observation error is defined as the difference between the measured output and the estimated output. The observer model is defined in equation (3.24) where $\tilde{x}$ is the

56

estimated state and $C\tilde{x} + Du$ is the estimated output. Collecting the states, controls, and outputs gives equation (3.25).

$$\{\dot{\tilde{x}}\} = [A]\{\tilde{x}\} + [B]\{u\} + [K_e](\{y\} - [C]\{\tilde{x}\} - [D]\{u\})$$ (3.24)

$$\{\dot{\tilde{x}}\} = ([A] - [K_e][C])\{\tilde{x}\} + ([B] - [K_e][D])\{u\} + [K_e]\{y\}$$ (3.25)

The matrix K_e is the observer gain matrix. This gain matrix weights the correction term involving the difference between the measured output and the estimated output. The error vector is defined by (3.26) and the observer error equation is given by (3.27). The matrix K_e is selected such that $[A-K_eC]$ is a stable matrix and the error vector converges to zero. This is accomplished by finding the steady state gain, K_e, using the MATLAB *kalman.m* function. The gain matrix K_e provides the optimal solution to the steady state observer estimation problem given the state equations (3.20) and (3.23) with known inputs and Gaussian plant noise and measurement noise. The gain matrix K_e is used to find the state estimate, $\{\tilde{x}\}$, that minimizes the steady state error covariance shown in equation (3.28).

$$\{e\} = \{x\} - \{\tilde{x}\}$$ (3.26)

$$\{\dot{e}\} = ([A] - [K_e][C])\{e\}$$ (3.27)

$$P = \lim_{t \to \infty} E\left(\{x - \tilde{x}\}\{x - \tilde{x}\}^T\right)$$ (3.28)

F.   DEFORMABLE MIRROR SIZING AND MODELING

This section determines the tweeter deformable mirror actuator count and spacing required to compensate for the primary mirror residual error. The actuator count and spacing is used to model tweeter deformable mirror using an influence matrix. First the methodology used for sizing the deformable mirror is presented. Next deformable mirror models are presented to correct the residual error of the SMT AHM segment and the 1-meter CFRP mirror. Finally a model of the Boston Micromachine Corporation (BMC) Multi-DM used in the experimental setup presented in Chapter VI is described.

1.   Sizing the Deformable Mirror

The deformable mirror actuator count and spacing depends on the residual error being corrected. The desire is to reduce the residual RMS wavefront error to $\lambda/15$ waves RMS. Scholl and Lawrence [73] investigated the feasibility of using a deformable mirror

to correct quasi-static changes of on-orbit primary mirrors and showed that to achieve a Strehl ratio of 0.95 the actuator spacing corresponded to approximately half the Nyquist frequency. The first step to sizing the deformable mirror is to determine the dominant spatial frequencies using the 2D FFT residual error plots. This spatial frequency information determines the number of actuators and actuator spacing of the tweeter in order to spatially filter the dominant frequencies.

Next the deformable mirror influence function is modeled. Two common approaches to modeling a continuous surface normal deformable mirror actuator influence functions is to use a cubic function or Gaussian function [48]. This research uses a Gaussian function to model the actuator influence to present a generalized deformable mirror instead of a specific mirror technology like bimorph piezo-electric or MEMs. The Gaussian function was chosen for simplicity but does not model deformable mirror edge constraints as noted by [74]. Equation (3.29) represents a two-dimensional Gaussian influence function where r_s is the actuator spacing, a is the actuator coupling coefficient, b is the Gaussian index, and S is the stroke of the mirror deflection. This function was modified to generate a 3D response that represents the 2D OPD output of a single actuator.

$$IF_{Gaussian}(r) = S\left(\exp\left(\ln(a)\left(\frac{|r - r_i|}{r_s} \right) \right)^b \right) \tag{3.29}$$

The actuators were modeled over a square grid with the actuator spacing matching the dominant spatial frequency found using the 2D FFT. The actuator spacing was assumed to be constant over the mirror. To represent the hexagonal SMT aperture shape or circular CFRP mirror shape an aperture mask was applied to the square actuator grid and the unused actuators were removed. The influence function stroke was set to 2.5 times the RMS wavefront error. Figure 33 shows an example of a rectangular actuator grid with a SMT segment hexagonal mask, and Figure 34 shows an example of a rectangular actuator grid with the SMT pupil plane mask. The deformable mirror influence matrix model is built from the individual influence function responses.

58
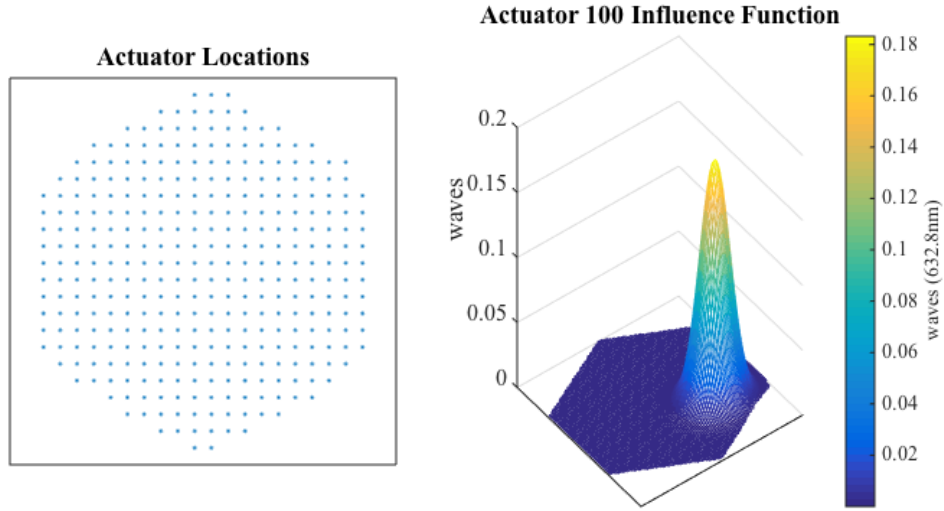
Figure 33. Deformable mirror model with 333 actuators in rectangular grid
(left), model influence function for actuator 100 (right)
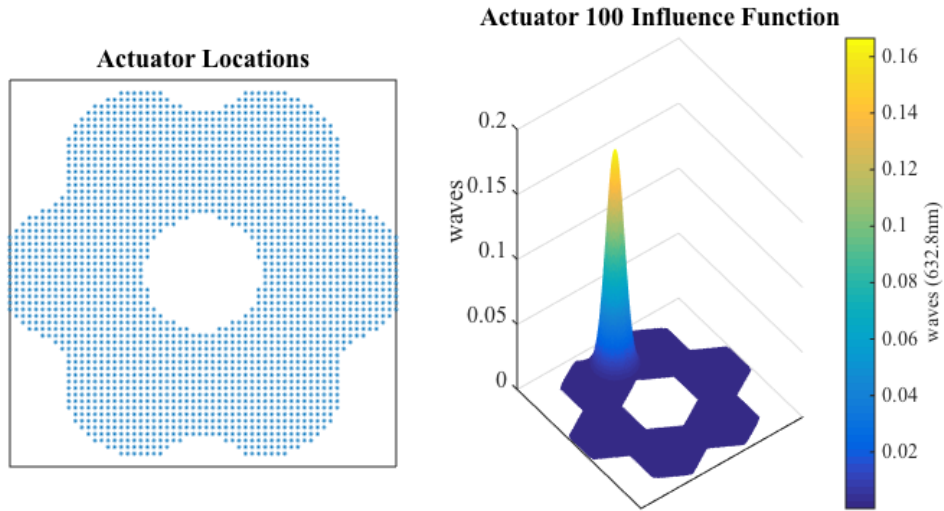
Figure 34. Deformable mirror model with 1778 actuators in rectangular grid
and SMT pupil plan mask (left), model influence function for actuator 100 (right)

2.   Deformable Mirror Model for SMT AHM

A 2D Fourier transform of the SMT residual wavefront error identified the prominent spatial frequencies. Figure 25 shows the Fourier transform log plot and the dominant spatial frequencies are below 25 cycles/aperture. The corresponding actuator spacing results in a 25 x 25 actuator grid for the tweeter. The actuator spacing, response function from equation (3.29), and the SMT hexagonal mask results in an influence

matrix model with a total of 543 active actuators. The actuator stroke is set to 2.5 times the RMS wavefront error.

The tweeter deformable mirror model is included in a simulated control loop to correct the residual SMT AHM residual error model. The control loop is a global iterative constrained minimization controller and presented in Chapter IV. The closed loop controller can use either the measured OPD or SVD modal coefficients as feedback. The SVD modes represent the spatial modes of the woofer-tweeter mirror system. Figure 35 shows the error history using OPD feedback and SVD modal feedback including the first 25 SVD modes, 50 SVD modes, 75 SVD modes, and 100 SVD modes. The 543 channel tweeter achieves a RMS wavefront error below $\lambda/15$ and reduces the peak-to-valley wavefront error below 1 wave. The simulation also shows that including higher order SVD modes in the feedback improves the wavefront. The two-dimensional FFT log plot, Figure 36, shows that the deformable mirror model successfully removed the dominant spatial frequencies.
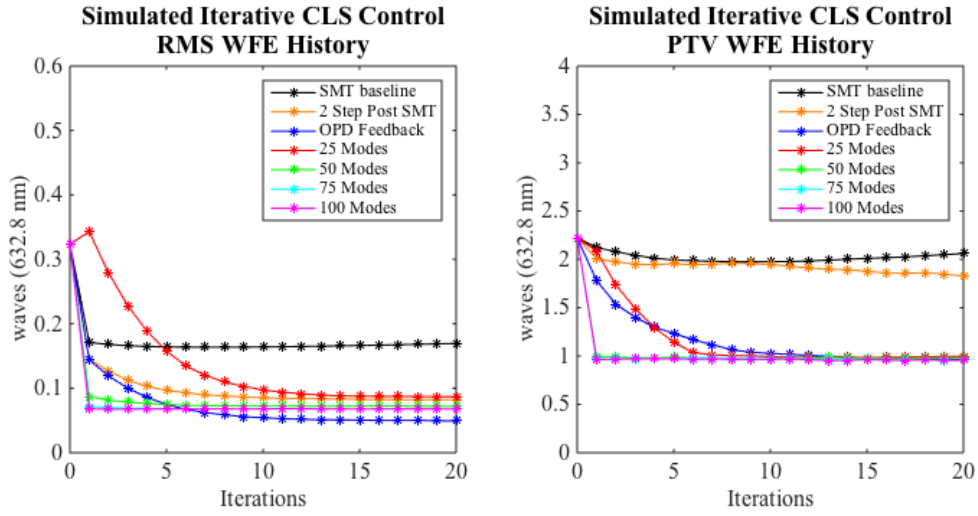
Figure 35. Simulated 543-channel tweeter with global constrained least squares controller, RMS wavefront error history (left), and peak-to-valley wavefront error history (right), from [16]
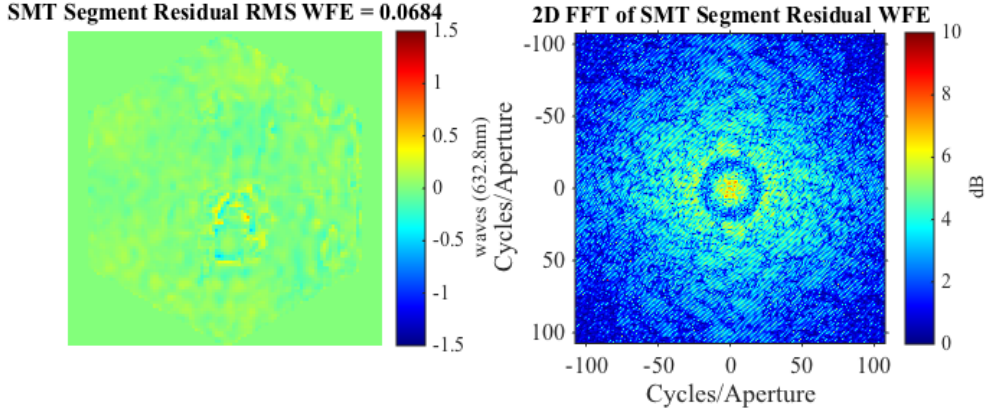
Figure 36. 2D FFT log plot of simulated dual deformable mirror residual surface

3.   Deformable Mirror Model for CFRP Mirror

The same deformable mirror sizing approach used for the SMT AHM mirror is used for the CFRP mirror. A 2D Fourier transform of the SMT residual wavefront error identified the prominent spatial frequencies contributing to the residual error. Figure 37 shows the Fourier transform log plot and the dominant spatial frequencies are below 75 cycles/aperture. The corresponding actuator spacing results in a 75 x 75 actuator grid for the tweeter [16]. This actuator count is very large and greater than the actuator count of commercially available deformable mirrors.

Instead of correcting with an unrealistic deformable mirror model the deformable mirror sizing process was incorporated into a simulation where the number of actuators was considered a variable. This allowed multiple deformable mirror models to be tested against the CFRP mirror residual wavefront. This simulation used equal actuator spacing and the response function from equation (3.29). Figure 38 shows a plot of predicted residual wavefront error versus deformable mirror actuator count for the CFRP mirror, and Figure 39 shows the wavefront error after using a 437 actuator deformable mirror. These results show significant amount of wavefront error, but a significant amount of improvement is seen using as little as a 32-actuator deformable mirror as shown in Figure 38. The addition of more actuators continues to improve the wavefront, but the high spatial frequency aberrations require an impractical number of actuators to further reduce

61

the wavefront error. A better approach is to further improve the CFRP mirror high spatial frequency surface errors and allow the deformable mirror to correct the lower spatial frequencies.
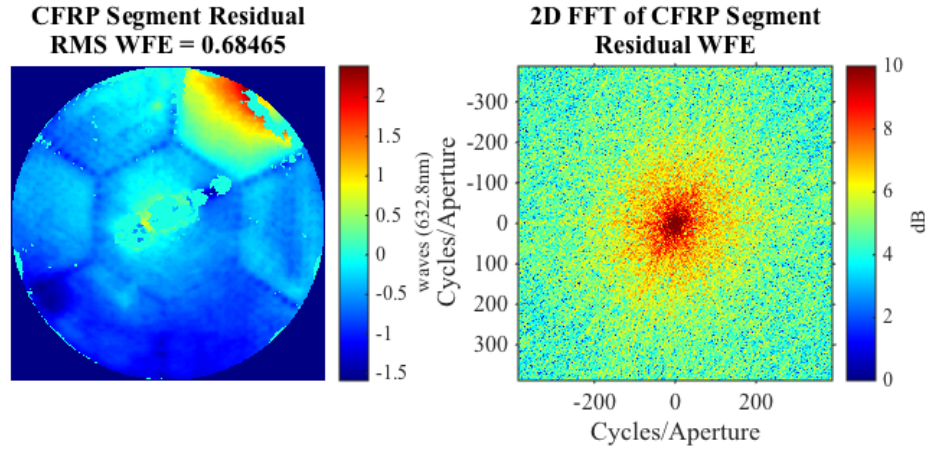
Figure 37. CFRP mirror residual error (left) and two-dimensional FFT log plot of 1-m CFRP mirror residual surface error (right)
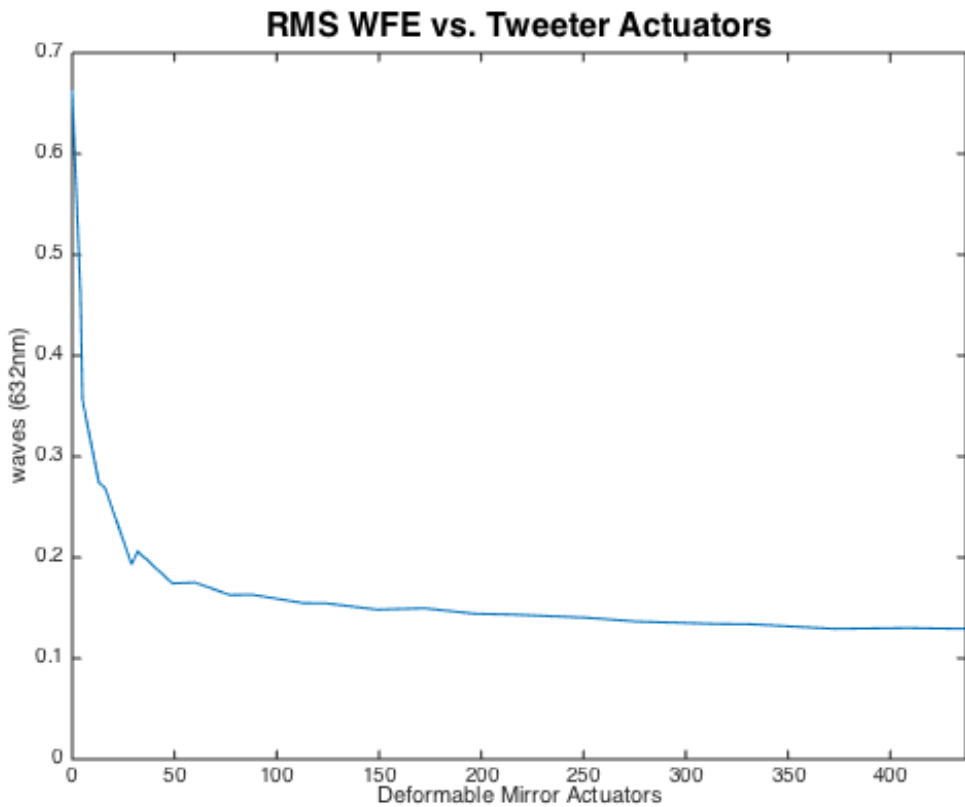
Figure 38. CFRP mirror rms wavefront error versus number of deformable mirror actuators
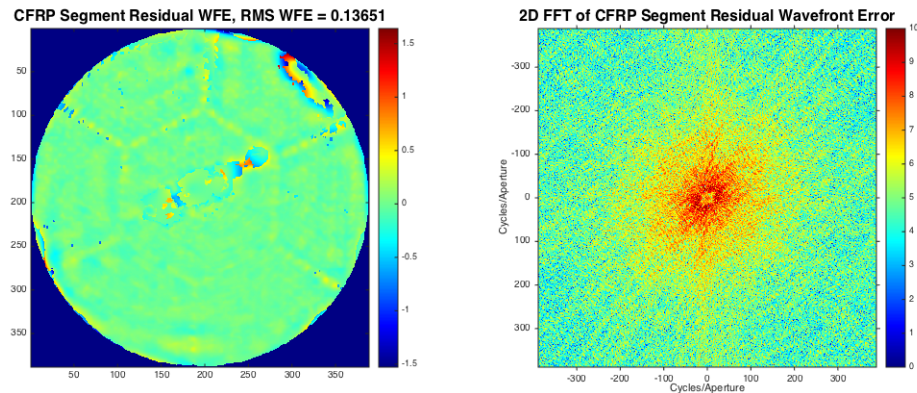
Figure 39. CFRP mirror residual error after correction using deformable mirror with 437 actuators (left), and 2D FFT log plot of corrected CFRP mirror showing low frequencies removed (right)

The majority of the CFRP mirror residual error is attributed to the discontinuities in the OPD caused by the measurement dropouts, and the substrate hexagonal print-through. Future versions of CFRP mirrors may fix these problems and the mirror may be closely modeled using a Zernike approximation. Figure 40 and Figure 41 show the Zernike approximated OPD and 2-dimensional FFT before and after correction using 176 actuators. Figure 42 shows that the simulation achieves λ/20 RMS wavefront error using a deformable mirror with as few as 150 actuators.
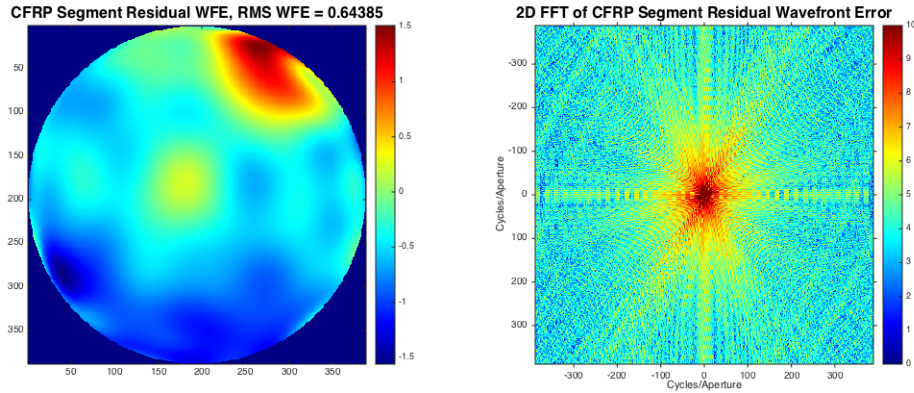
Figure 40. CFRP mirror Zernike approximation residual error (left) and 2D FFT log plot of 1-m CFRP mirror Zernike approximation residual surface error (right)
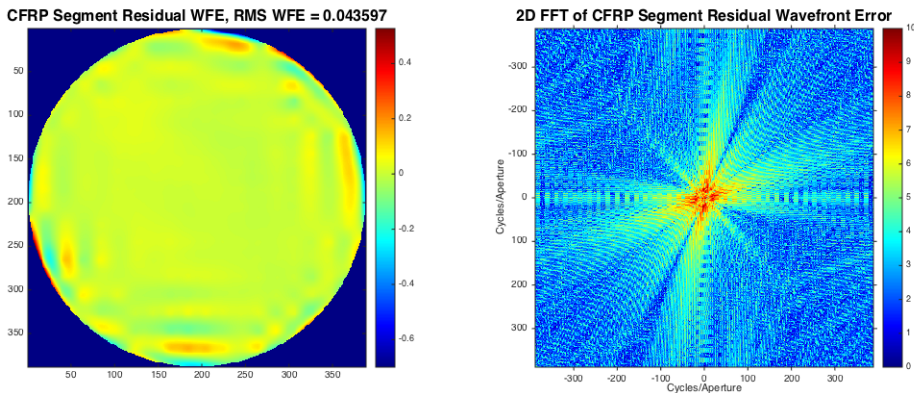
Figure 41. CFRP mirror Zernike approximation residual error after correction (left), and 2D FFT log plot of corrected CFRP mirror Zernike approximation showing low frequencies removed (right)
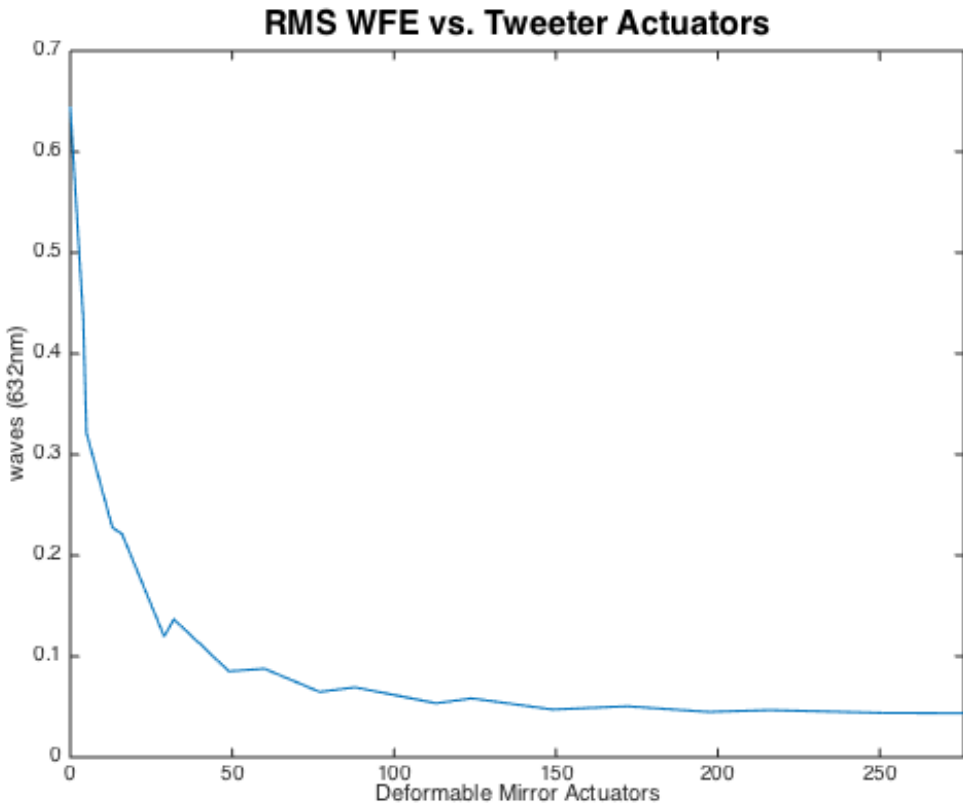
Figure 42. CFRP mirror RMS wavefront error approximated with 105 Zernike modes versus number of deformable mirror actuators

4. Boston Micromachine Corporation (BMC) Multi-DM Model

In addition to the analytical deformable mirror models a Boston Micromachine Corporation (BMC) Multi-DM with 140 actuators, a 3.3mm by 3.3mm square aperture, and 1.5μm of stroke was modeled. This deformable mirror is used in the experimental test bed described in Chapter VI. The mirror model is an experimentally derived influence matrix. The BMC deformable mirror actuators were mapped to the SMT segment and the unused actuators were masked and removed them from the influence matrix. Based on the location of the deformable mirror in the experimental test bed, 61 of the 140 actuators had influence over the SMT segment wavefront.

G.   SMT WOOFER-TWEETER MODEL

Two woofer-tweeter models were developed. The SMT woofer-tweeter model represents the entire SMT system while the SMT segment woofer-tweeter model represents a single segment woofer-tweeter model. Both models place the deformable mirror at the exit pupil and assume segment phasing is complete. The models are described in more detail in the following sections.

1.   SMT Woofer-Tweeter Model

The SMT and deformable mirror system model combines the SMT quasi-static state space model and the deformable mirror model. The model output is the sum of the two mirror OPDs and the input is vector of actuator inputs for the SMT FSAs. The quasi-static approach takes advantage of the fact the structural dynamics are slow compared to the response of the FSAs and the deformable mirror. The response bandwidth of the SMT segment and the deformable mirror are assumed to be the same. The assumption is valid because the wavefront sensor measures the combined contribution of both mirrors and is slower than the mirrors response bandwidth.

The SMT model uses the sensor outputs to reconstruct the wavefront of the individual segments and recombines the segments to form the entire aperture. In a similar fashion portions of the deformable mirror are mapped to a particular SMT segment to individually correct the residual error of the segments. The model allows for the SMT FSAs and deformable mirror actuators to be commanded either in serial or parallel depending on the controller.

Zero mean Gaussian plant noise and sensor noise is introduced into the model. Plant noise is modeled as a disturbance on the actuator inputs to the quasi-static model. The Shack-Hartmann sensor noise is introduced at the model OPD output, and the phase diversity noise is introduced after converting the OPD pupil image to the image plane. The manufacturer's actuator and sensor variances are used to model the noise.

2.   SMT Segment Woofer-Tweeter Model

The woofer-tweeter deformable mirror model represents the experimental woofer-tweeter system presented in Chapter VI. The model reduces the complexity of the larger system model by only modeling one of the six SMT AHM segments. This is suitable because the system level fine phase controller corrects the surface of individual segments. The single SMT segment and BMC deformable mirror are modeled using experimental influence matrices. The experimental influence matrices built using equation (2.6) where the columns represent the influence function.   The influence matrices represent the physical response of the system. The influence functions are represented as either the measured OPD, or SVD modal coefficients. The influence matrix composed of OPD influence functions result in an over-determined system.

The experimental influence matrices are examined to determine how well the influence matrix can correct the mirrors. The SMT AHM and BMC deformable mirror influence matrix normalized singular values are shown in Figure 43 and can identify poorly observable or controllable modes. Small singular values can cause large gains when the influence matrix is inverted and included in a feedback controller. To prevent the model from causing large feedback gains, modes represented by normalized singular values of 0.1 or less are removed. These modes represent less than 10% of the peak magnitude and are not well corrected by the mirrors. These modes also represent high spatial frequencies. For the SMT AHM this includes SVD modes greater than 12 and for the BMC deformable mirror it includes modes greater than 40. Depending on the simulation the modal feedback is removed above these modes or the influence matrix is truncated to prevent the small singular values from generating large gains in the control matrix. Zero mean Gaussian plant noise is used in the system level model.
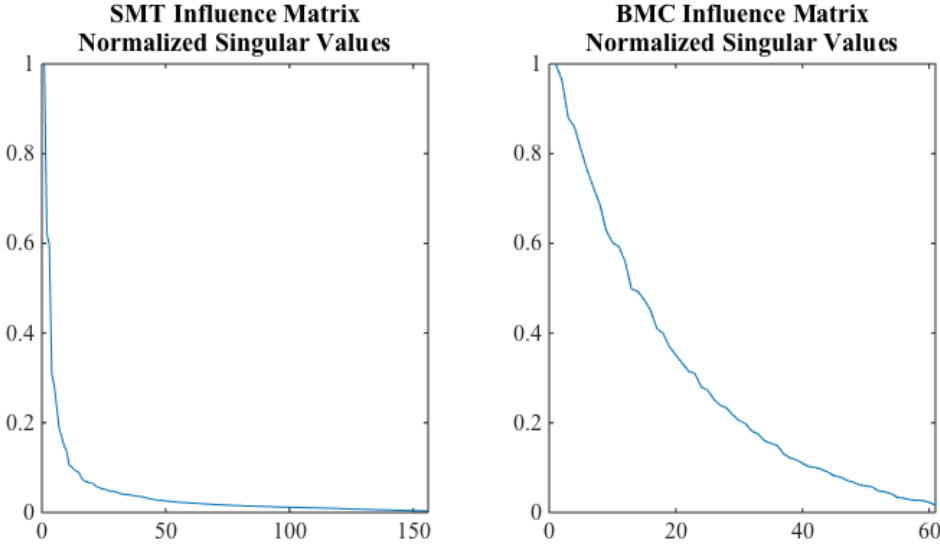
Figure 43. SMT AHM and BMC deformable mirror influence matrix
singular values

The sensor is modeled as the laser interferometer used in the experimental setup. The laser interferometer measures the wavefront error at the pupil plane. The laser interferometer is modeled as the OPD output from the SMT and deformable mirror model with zero mean Gaussian sensor noise. The laser interferometer output standard deviation is very small at 0.002 waves (632.8 nm) RMS.

H.   CONCLUSION

This chapter presented the models used to simulate the SMT, the deformable mirror, and woofer-tweeter system. The system level SMT dynamic model is used to simulate coarse alignment and coarse phasing control, while the fine phasing control design is based on the quasi-static model. The residual error model is used to identify dominant residual surface error in order to select the number and spacing of the tweeter actuators. The analytical models developed in this chapter are the basis for the control design in Chapter IV and the simulation performed in Chapter V.

IV.   SPACE TELESCOPE WAVEFRONT CONTROL

This chapter develops the control techniques for a space telescope with a segmented active primary mirror and an additional deformable mirror in the optical assembly. First the chapter presents SMT incremental wavefront control techniques including coarse alignment, coarse phasing, and fine phasing techniques. Next the chapter presents techniques to improve fine phasing residual error. This includes using an additional deformable mirror in a woofer-tweeter configuration in order to improve the fine phasing residual wavefront error, and updating the SMT AHM segment model. Existing closed loop woofer-tweeter control techniques are presented and a woofer-tweeter gradient control technique is introduced. Open-loop woofer-tweeter control techniques are also introduced. Finally an adaptive influence matrix technique is presented as a means to improve fine phasing residual wavefront error by improving the SMT AHM segment model.

A.   SMT WAVEFRONT CONTROL

In preparation for the woofer-tweeter fine phasing control this section reviews the wavefront sensing and control architecture of the SMT.   State feedback control techniques are discussed as a means to incrementally phase the telescope segments and improve the wavefront error.   The incremental control approach includes segment stacking, coarse alignment, coarse phasing, and fine phasing.

1.   SMT Wavefront Control Approach

The SMT model developed in Chapter III presents a traditional MIMO control problem. The traditional approach to a MIMO control problem uses modern control techniques like a linear quadratic regulator (LQR) or linear quadratic Gaussian (LQG) controller. Correia et al. [75] proposed an LQG control approach for future large aperture ground-based astronomical telescopes where the dynamics of the mirrors cannot be ignored. A similar state-feedback control approach is applied to the SMT using multiple control loops to perform and maintain coarse alignment, coarse phasing, and fine

phasing. This control approach uses the dynamic and quasi-static models developed in the previous chapter.

The SMT control approach is an incremental approach that first aligns the segments, then phases the segments, and then improves the wavefront error caused by surface imperfections on the primary mirror segments. Figure 44 shows the incremental alignment and wavefront control approach for the SMT. Segment alignment begins after telescope deployment.

After telescope deployment the segments are set in place using actuator settings determined during ground testing. The initial telescope wavefront errors are expected to be on the order of millimeters. The telescope begins the incremental segment phasing routines by pointing the telescope toward a star to serve as a coherent light source. The wavefront error of the SMT incrementally improves until the total wavefront error of the telescope is less than $\lambda/15$ rms for 0.6 μm light.

State feedback control is used for the coarse alignment, coarse phasing, and the FCA fine phasing control. These controllers are simulated with the SMT dynamic model. The FSA control is simulated using the SMT quasi-static model. After initial alignment and phasing the coarse phasing and fine phasing controllers provide maintenance control to maintain the optical quality of the telescope and prevent error growth.
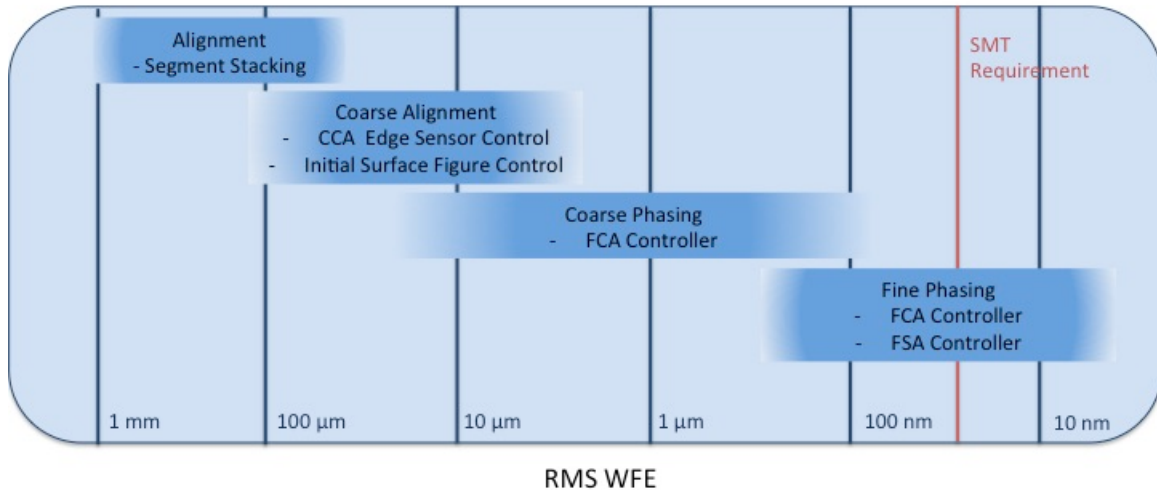
Figure 44. SMT incremental alignment and wavefront control approach

2. Segment Stacking

The first alignment step identifies the SMT segments on the camera focal plane. If a segment sub-image is not on the focal plane the segment is steered using the CCAs until the sub-image appears on the focal plane. Identifying the sub-images may require deliberate misalignment in order to identify them individually at the focal plane. To associate the sub-images to a segment they are individually moved and new images are taken and compared to the previous images. Figure 45 shows the initial unaligned sub-images and Figure 46 shows a composite history of segment identification. The centroid location of the segment sub-image on the focal plane provides feedback to the stacking control law. The stacking control law actuates the CCAs to drive the six sub-images to the center and reduces the alignment error from millimeters to 10s of micrometers.
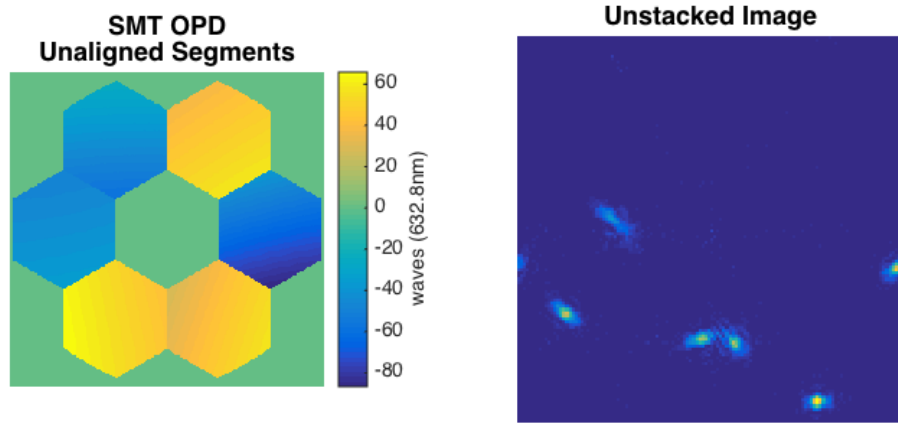
Figure 45. Unaligned SMT segments OPD at exit pupil (left), and unstacked segment images at image plane (right)
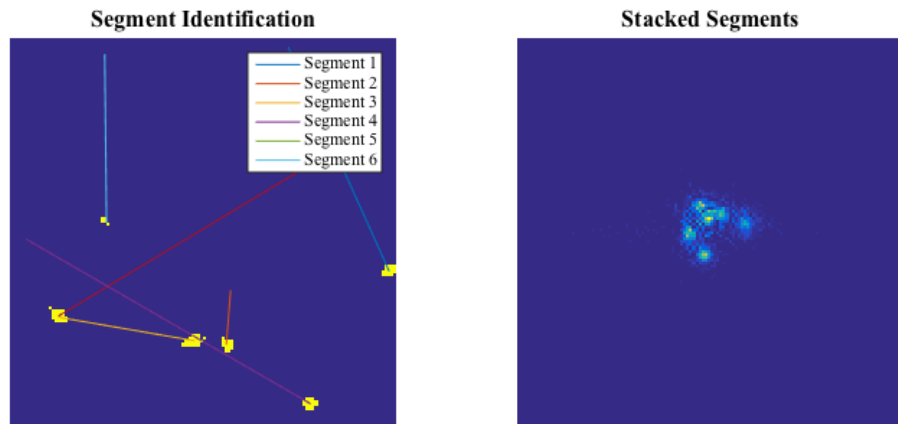
Figure 46. SMT sub-image segment identification (left), and stacked segment sub-images (right)

3.   Coarse Alignment

Coarse alignment coarsely aligns the segments using the edge sensors and the CCAs. The SMT development program showed that the edge sensors originally used on the program were not accurate enough to phase the segment edges. NASA JPL developed a laser truss metrology system to aid in the phasing of segmented telescopes. The laser truss metrology system could provide continuous feedback to the segment hexapod actuators to capture and maintain phasing.

72

The SMT model uses the edge sensors to build a LQG state feedback controller to drive the edge sensor error to zero. The edge sensors output is a differential displacement in the global z direction between the segment and the center core structure. The model introduces plant noise at the actuator and edge sensor measurement. The state space model from Chapter III is modified to only include edge sensor measurements and CCA commands. The state equations are updated to include zero mean Gaussian plant noise, w, and sensor noise, v. The matrices G and H are the respective covariance matrices. We use a Kalman estimator to predict the state where L is the Kalman gain, equation (4.3).

$$\{\dot{x}\} = [A]\{x\} + [B]\{u\} + [G]\{w\} \tag{4.1}$$

$$\{y\} = [C]\{x\} + [D]\{u\} + [H]\{w\} + \{v\} \tag{4.2}$$

$$\{\dot{\tilde{x}}\} = [A]\{\tilde{x}\} + [B]\{u\} + [L](\{y\} - [C]\{\tilde{x}\} - [D]\{u\}) \tag{4.3}$$

The state feedback control law (4.4) minimizes the quadratic cost function (4.5) subject to the system dynamics, (3.14). The Q matrix weights the error while the R matrix weights the amount of control expended. The Q and the R matrices are both positive definite. To find the optimal gain K the linear control law is substituted into the dynamics and cost function and then the optimization problem is solved [76]. The matrix K must ensure that the eigenvalues of [A-BK] have real and negative parts to ensure the system is stable.

$$\{u\} = -[K]\{x\} \tag{4.4}$$

$$J = \int_{0}^{\infty} \left(\{x\}^T [Q]\{x\} + \{u\}^T [R]\{u\} \right) dt \tag{4.5}$$

$$\{\dot{x}\} = [A - BK]\{x\} \tag{4.6}$$

After coarse alignment a Shack-Hartmann wavefront sensor measurement is taken and an initial surface correction is applied to the segment surface using the adaptive optics control approach like (2.10). The Shack-Hartmann sensor has a large capture range and does not measure segment piston. Tip and tilt are removed from the measurement to prevent the saturation of the FSA actuators. The initial segment correction improves the focal plane measurements and further reduces the wavefront error.

4. Coarse Phasing

The coarse phasing control loop further improves phasing using the FCAs. Both the edge sensors and phase diversity wavefront sensor provide feedback. The phase diversity sensor removes bias and drift from the edge sensor. However, the segments must be phased within the capture range of the phase diversity sensor. A state feedback controller and Kalman estimator are used in a similar manner as the coarse alignment controller where the state space model is modified to only input FCA commands and output edge sensor measurements.

The SMT system depends on the edge sensors and coarse controllers to align the segments within the capture range of the phase diversity sensor which is less than 1 wave peak-to-valley [11]. In this simulation the edge sensor models are used. However on more recent segmented optical telescope programs like ATLAST and OPTIIX the preferred sensor technique is DFS. Once the segments are aligned within the capture range of the phase diversity sensor, the phase diversity measurements provide more accurate tip, tilt, and piston measurements (< 6 nm).

5. Fine Phasing

The fine phasing control loops include the FSAs and the FCAs. The FSAs primarily control the surface of the segment. The FCA actuators are updated to offload piston, tip, and tilt from the FSAs. The fine phasing control loops use the Shack-Hartmann wavefront sensor and phase diversity wavefront sensor. The Shack-Hartmann wavefront sensor measures the low spatial frequency surface errors at high rates, while the phase diversity wavefront sensor also measures high spatial frequency surface error and piston error at low rates.

The wavefront is incrementally improved by first reducing the piston, tip, and tilt errors using the FCAs and phase diversity sensor. Next the lower spatial frequency surface errors are improved using the FSAs and Shack-Hartmann wavefront sensors. The segment wavefront errors are further improved using the FSAs and the phase diversity sensor with the Gerchberg-Saxton phase retrieval algorithm. This phase retrieval

algorithm captures the segment surface errors that are unobserved by the Shack-Hartmann wavefront sensor.

The FCA controller uses the dynamic SMT model and the FSA controller uses the quasi-static model. To capture realistic residual surface error of the SMT segments the model uses measured SMT segment data for the segment face sheet initial conditions. This data is taken at the SMT biased position. The FCA fine phase controller uses the segment piston, tip, and tilt measurements from the phase retrieval process in a state feedback controller. The FSA controllers use integral control using an influence matrix calibrated to the specific segment.

Another FSA fine phasing approach is to apply open loop control voltages determined from a constrained minimization. This approach assumes that the influence matrix model accurately predicts the surface figure of the SMT segment and that the SMT segment maintains the surface figure over an extended period of time. This approach has the advantage of not requiring continuous feedback and preventing FSA saturation. Solving a constraint based minimization may not be practical onboard the spacecraft. However, solving the minimization on the ground and periodically updating the FSA control signals is feasible.

B.   FINE PHASING IMPROVEMENTS

This section introduces three approaches to improve the SMT fine phasing wavefront error. The first approach uses an additional deformable mirror in a closed loop woofer-tweeter configuration to correct residual wavefront error. The second approach uses an additional deformable mirror in an open loop optimal woofer-tweeter configuration to correct residual wavefront error. The third approach addresses variation between the SMT AHM segment model and the physical system. An adaptive influence matrix technique is introduced to improve the performance of the SMT AHM model and improve the fine phasing residual wavefront error.

1. Woofer-Tweeter Closed-Loop Control

This section presents the closed control of the additional deformable mirror in a woofer-tweeter configuration with an SMT segment as part of the fine phasing control loop. Existing closed loop woofer-tweeter control techniques are described with consideration to the SMT application, and a new woofer-tweeter gradient control technique is introduced. The woofer-tweeter mirrors are controlled simultaneously using the feedback from the Shack-Hartmann wavefront sensor and phase diversity phase retrieval. The woofer-tweeter control techniques are developed and modeled using the quasi-static SMT segment woofer-tweeter model developed in Chapter III. The woofer-tweeter control techniques presented are as follows: serial control, global control, offload control, modal control, and optimal control.

a. *Serial Control*

The serial woofer-tweeter controller uses two sequential iterative constrained minimization controllers to correct the woofer and then correct the tweeter. This technique does not simultaneously control the woofer and tweeter. First the woofer correction is applied until a steady state wavefront error is reached and then the tweeter correction is applied.

b. *Global Control*

A simple technique to controlling the woofer-tweeter system is to build a global influence matrix and control the system as a single device as suggested in [38]. The global influence matrix concatenates the woofer influence matrix ($m \times n_w$) and tweeter influence matrices ($m \times n_t$) into one matrix. This is possible because the SMT segment influence matrix and deformable mirror influence matrix have the same number of rows since the influence matrices are measured from the same wavefront sensing system. The result is a single influence matrix for the woofer-tweeter system, equation (4.7).

$$[\Gamma_G] = \begin{bmatrix} \Gamma_{SMT} & \Gamma_{Tweeter} \end{bmatrix} \qquad (4.7)$$

76

(1)   Integral Control

A standard adaptive optics integral control technique can use the global influence matrix to form a control matrix by taking the pseudo inverse, equation (4.8). Hampton et al. [38] consider this method impractical because the ratio of actuator motion to control signal for the woofer can be significantly higher than that of the tweeter causing woofer measurement noise to be much greater than tweeter noise. However, the SMT woofer-tweeter system combines two mirrors with similar stroke and control voltages, and bandwidth reducing the likelihood of this concern. The active SMT segments and the Figure 47 shows a block diagram of this control approach where Γ represents the global influence matrix.

$$\{u_{k+1}\} = g[\Gamma_G]^\dagger \{e_k\} + \{u_k\} \tag{4.8}$$
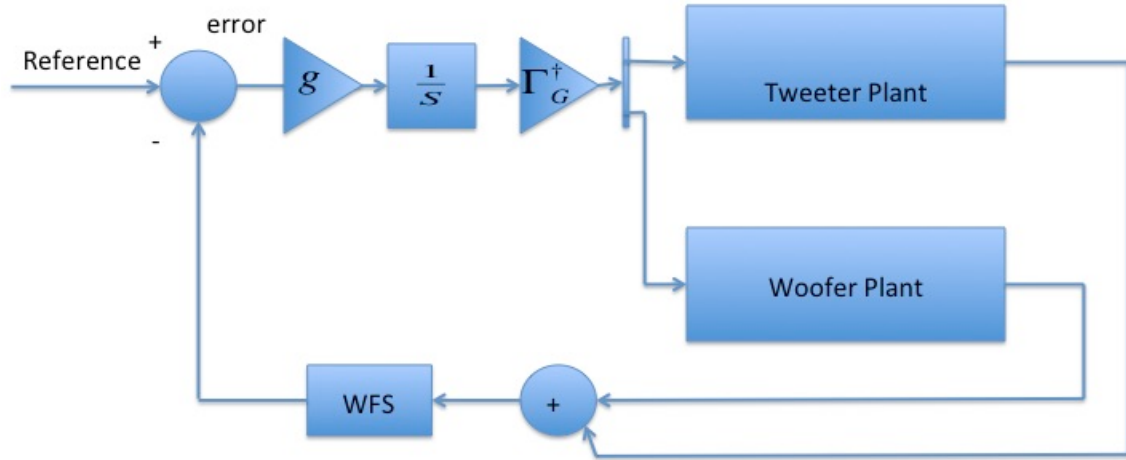
Figure 47. Global woofer-tweeter control block diagram

(2)   Global Iterative Constrained Minimization

Integral feedback control can saturate the segment actuators and second deformable mirror actuators. To prevent actuator saturation an iterative constrained optimization approach minimizes the wavefront and ensures the control signals remains within the limits of the actuators. Equation (4.9) represents the woofer-tweeter system as a single step linear model. The output is in terms of wavefront measured in optical path

difference, $\{\phi\}$, and $\{\phi_0\}$ is wavefront that represents the initial condition. A constrained minimization approach uses the quadratic cost function in equation (4.10) subject to the lower bounds and upper bounds of available control. This technique is a least squares problem with inequality constraints. An open loop or closed loop controller can apply the resulting control signal. The simulation and experiment use iterative feedback control since there is uncertainty between the model and the plant. Equation (4.11) updates the control signal iteratively using the solution to the constrained minimization. This requires the constrained minimization to be solved at each step with new lower and upper bounds represented by $u_{c,k}$. The gain μ is chosen between 0 and 1 [16].

$$\{\phi\} = [\Gamma_G]\{u\} + \{\phi_0\} \tag{4.9}$$

$$\arg\min \ J(u) = \frac{1}{2}\left[\left([\Gamma_G]\{u\} + \{\phi_0\}\right)^T \left([\Gamma_G]\{u\} + \{\phi_0\}\right) \right]$$
$$\text{subject to: } lb \leq \{u\} \leq ub \tag{4.10}$$

$$\{u_{k+1}\} = \mu\{u_{c,k}\} + \{u_k\} \tag{4.11}$$

(3)   Gradient Control

Another global woofer-tweeter control technique uses a local gradient approach. A similar approach was shown by Zhu et al. [77] to control a single micro-machined deformable mirror using Zernike coefficients. This work uses a woofer-tweeter global influence matrix, Γ_G, represented by singular value decomposition (SVD) mode shape coefficients. The global influence matrix is transformed to a modal influence matrix, $\hat{\Gamma}_G$, using the singular value decomposition.

$$[\Gamma_G] = [U][\Sigma][V]^T \tag{4.12}$$

$$[\hat{\Gamma}_G] = ([\Gamma_G][V])^\dagger [\Gamma_G] \tag{4.13}$$

SVD modal coefficients represent the wavefront using equation (4.14). The variable a_c is the wavefront correction and a_{aber} is the wavefront aberration caused by the imperfect mirror surface.

$$\{a\} = \{a_c\} + \{a_{aber}\} \tag{4.14}$$

$$\{a_c\} = [\hat{\Gamma}_G]\{u\} \tag{4.15}$$

$$\{a\} = [\hat{\Gamma}_G]\{u\} + \{a_{aber}\} \tag{4.16}$$

78

Equation (4.17) defines a cost function as the square of the wavefront error and equation (4.18) defines the wavefront error. The variable y is the measured wavefront and the variable y_0 is the desired flat wavefront.

$$J = \{y - y_0\}^T \{y - y_0\} \tag{4.17}$$

$$\{y - y_0\} = [\Gamma_G][V]\{a\} = [\tilde{\Gamma}_G]\{a\} \tag{4.18}$$

$$J = \left([\tilde{\Gamma}_G]\{a\}\right)^T \left([\tilde{\Gamma}_G]\{a\}\right) \tag{4.19}$$

$$J = \left([\tilde{\Gamma}_G]\left([\hat{\Gamma}_G]\{u\} + \{a_{aber}\}\right)\right)^T \left([\tilde{\Gamma}_G]\left([\hat{\Gamma}_G]\{u\} + \{a_{aber}\}\right)\right) \tag{4.20}$$

Equation (4.21) takes the partial derivative of the cost function with respect to the control variable u, and equation (4.22) simplifies the previous equation. Next the partial derivative of the cost function is taken with respect to the control variable u, equation (4.21), and reduces to equation (4.22). The gradient of the cost is incorporated into a deepest decent algorithm to iteratively reduce the variance of the wavefront. The gradient control update equation is shown in equation (4.23). The steepest decent approach includes the positive small scalar gain α that is greater than zero. There are many techniques to choose the value of α to produce a minimum for the function J. However, a fixed step is the simplest and produces reliable results shown later in Chapter VI. For this controller the gain α is set between zero and the reciprocal of the largest eigenvalue of $[\tilde{\Gamma}_G]^T[\tilde{\Gamma}_G]$ which is also the largest squared singular value.

$$\frac{\partial J}{\partial u} = \left(2[\hat{\Gamma}_G]^T[\hat{\Gamma}_G]\{u\} + 2[\hat{\Gamma}_G]^T\{a_{aber}\}\right)[\tilde{\Gamma}_G]^T[\tilde{\Gamma}_G] \tag{4.21}$$

$$\frac{\partial J}{\partial u} = 2[\hat{\Gamma}_G]^T\left([\tilde{\Gamma}_G]^T[\tilde{\Gamma}_G]\{a\}\right) \tag{4.22}$$

$$\{u_{k+1}\} = \{u_k\} - 2\alpha[\hat{\Gamma}_G]^T\left([\tilde{\Gamma}_G]^T[\tilde{\Gamma}_G]\{a_k\}\right) \tag{4.23}$$

$$0 < \alpha < \frac{1}{\lambda_1} \tag{4.24}$$

A benefit of this control technique is that the square term, $[\tilde{\Gamma}_G]^T[\tilde{\Gamma}_G]$, in equation (4.23) is an SVD modal weighting matrix. The feedback vector of SVD modal coefficients $\{a\}$ is weighted by the square of the singular values of $\tilde{\Gamma}_G$, shown in equation (4.25) and equation (4.26) since U is a unitary matrix. This is beneficial because the weighting matrix is specific to the performance of the deformable mirrors.

Additionally the weighting matrix can be adjusted to remove specific modes or weight them differently.

$$\left[\tilde{\Gamma}_G\right]=\left[\Gamma_G\right][V]=[U][\Sigma] \tag{4.25}$$

$$\left[\tilde{\Gamma}_G\right]^T\left[\tilde{\Gamma}_G\right]=[\Sigma]^T[U]^T[U][\Sigma]=[\Sigma]^T[\Sigma] \tag{4.26}$$

c.   *Offload Control*

Another woofer-tweeter control technique considers the woofer and tweeter separately and implements an offload control technique [48], [67], [78]. This approach deliberately offloads stroke and spatial correction based on the correlation between the mirrors. The singular values of the two mirrors are used to identify the mirror to offload. For example, Figure 48 shows the zonal and modal normalized singular value plot of the SMT segment and BMC-140 influence matrices. In this case the BMC-140 deformable mirror influence matrix singular values indicate the mirror can better recreate more spatial modes than the SMT segment. Therefore the BMC-140 is considered the tweeter and the low spatial modes are offloaded from the tweeter onto the woofer. This technique spatially separates the control between the woofer and tweeter using an offload matrix, O. The offload matrix is the projection matrix of the tweeter onto the woofer. The offload matrix is found by taking the pseudo inverse of the woofer influence matrix, Γ_W, and multiplying it by the tweeter influence matrix, Γ_T. Each column of the offload matrix represents one influence function of the tweeter in woofer space. When used with an integral controller the control update is first determined for the tweeter. The tweeter control signal updates the tweeter and updates the woofer by projecting the tweeter control signal into the woofer control space by multiplying the offload matrix, O, by the tweeter control signal, equation (4.28) where $\{u_t\}$ is the tweeter control vector and $\{u_w\}$ is the woofer control vector. Figure 49 shows the offload matrix included in an integral feedback controller.

$$[O]=\left[\Gamma_W\right]^T\left[\Gamma_T\right] \tag{4.27}$$

$$\{u_w\}=[O]\{u_t\} \tag{4.28}$$
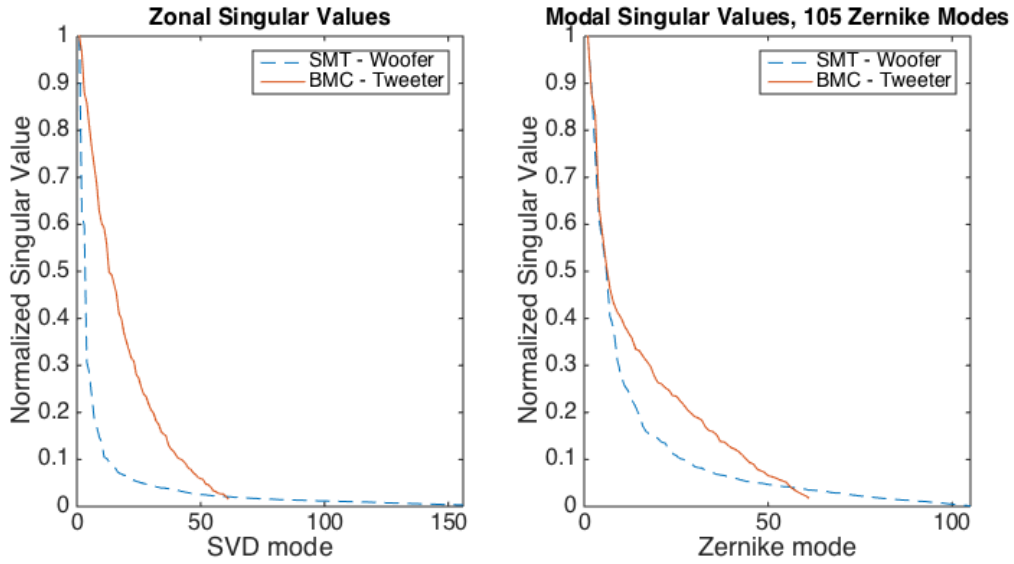
Figure 48. Influence matrix singular values, OPD influence matrix (left),
Zernike coefficient influence function (right)
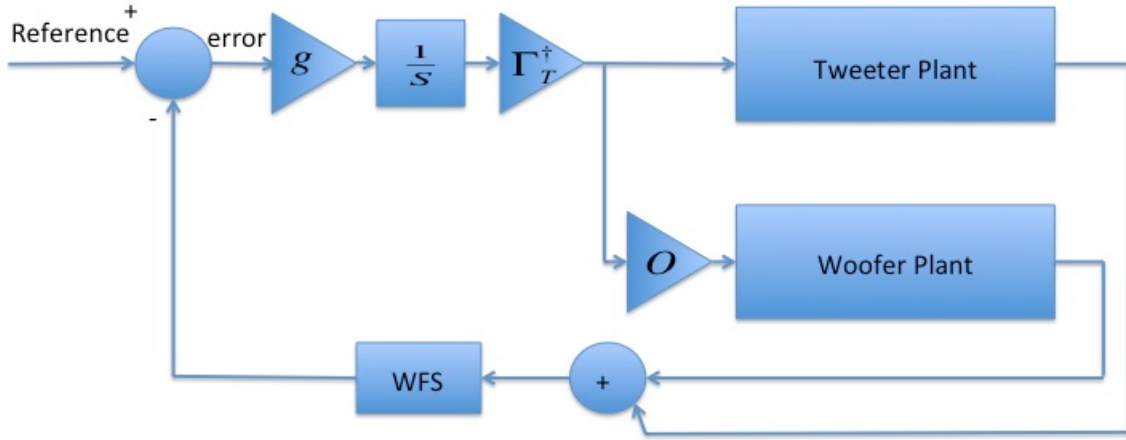
Figure 49. Offload woofer-tweeter control block diagram

d.   *Modal Control*

The modal woofer-tweeter control techniques separate the wavefront errors based on spatial modes like Zernike modes or SVD modes and assign the modes to either the woofer or tweeter.   This section presents several modal control techniques including modal coefficient control, confinement correction, and distributed modal control.

(1)   Modal Coefficient Control

A simple spatial mode control technique is modal coefficient control (MCC). This technique represents the wavefront error in terms of modal coefficients and splits the error signal between the woofer and tweeter by modal coefficients. Zernike polynomials typically represent the wavefront error because it is a common basis for both mirrors. Modal controllers use modal influence matrix models to represent the deformable mirrors. The SVD modal approach is used with SMT system because Zernike modes are not orthogonal over the hexagonal shape of the segments. Figure 50 shows the modal control block diagram.

The wavefront error represented by ϕ, is broken into two separate wavefronts, ϕ_1 and ϕ_2. The wavefront is represented using Zernike polynomials where a_n is the coefficient, and Z_n is the Zernike term. In this example ϕ_1 represents the low order modes corrected by the woofer and ϕ_2 represents the high order modes.

$$\phi = \phi_1 + \phi_2 \qquad (4.29)$$

$$\phi_1 = \sum_{n=1}^{k} a_n Z_n \qquad (4.30)$$

$$\phi_2 = \sum_{n=k+1}^{l} a_n Z_n \qquad (4.31)$$

The controller sends the low order modes to the woofer and high order modes to the tweeter. Two separate modal woofer and tweeter influence matrices are used to command the woofer and tweeter mirrors using an integral modal feedback controller. This control technique spatially separates the control between the two mirrors. A downside to this technique is that the mirrors cannot share stroke to correct the same mode. Therefore the deformable mirrors need to be independently sized to correct the anticipated errors.
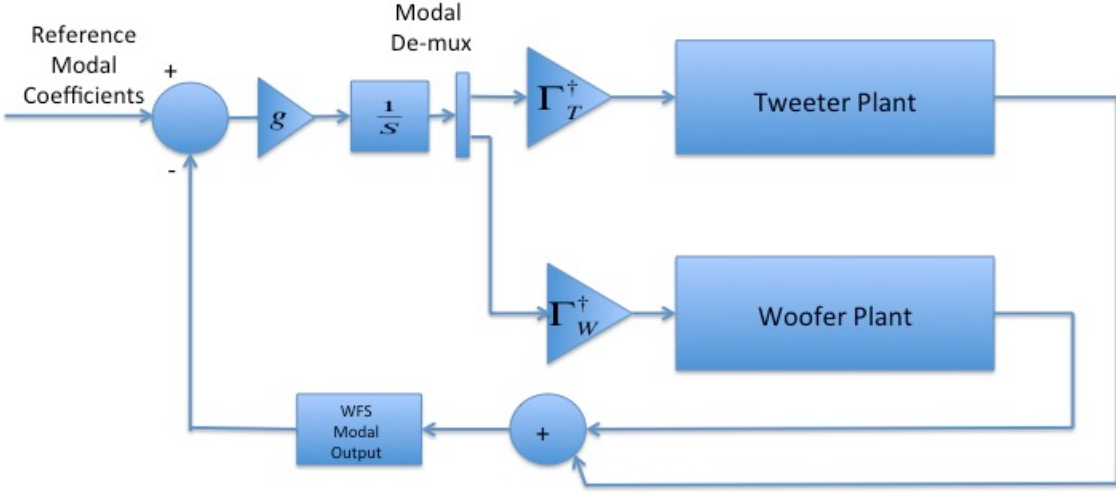
Figure 50. Modal control block diagram

(2) Confinement Correction Algorithm

Another modal control technique is the confinement correction algorithm from [79]. This technique skips the modal estimation of the wavefront error by directly splitting the gradient sensor error between the woofer and tweeter using a direction gradient method. This is accomplished by building a tweeter influence matrix that concatenates a gradient response influence matrix and modal influence matrix. The resulting tweeter command voltages are used to compute the high order gradient error corrected by the tweeter and compute the low order gradient error to be corrected by the woofer. This technique also uses integral feedback control.

The matrix H is used to convert the OPD outputs to slopes using the 61 lenslet Shack-Hartmann wavefront sensor geometry. This results in 122 outputs, 61 slopes in the x and y-axis. The influence matrices are transformed to sensor space by multiplying by H. The gradient and modal tweeter reconstruction matrix used in the confinement correction algorithm is found by concatenating the sensor space influence matrix, Γ_{T_Slopes}, and the modal influence matrix, $\hat{\Gamma}_T$. Figure 51 shows the block diagram of the confinement correction algorithm. The confinement correction controller measures the

residual error between the error signal and tweeter correction and sends the residual error to the woofer.

$$\{s\} = [H][OPD] \tag{4.32}$$

$$[\Gamma_{W\_Slopes}] = [H][\Gamma_W] \tag{4.33}$$

$$[\Gamma_{T\_Slopes}] = [H][\Gamma_T] \tag{4.34}$$

$$[\Gamma_{T\_CCA}] = \begin{bmatrix} \Gamma_{T\_Slopes} \\ \hat{\Gamma}_T \end{bmatrix} \tag{4.35}$$
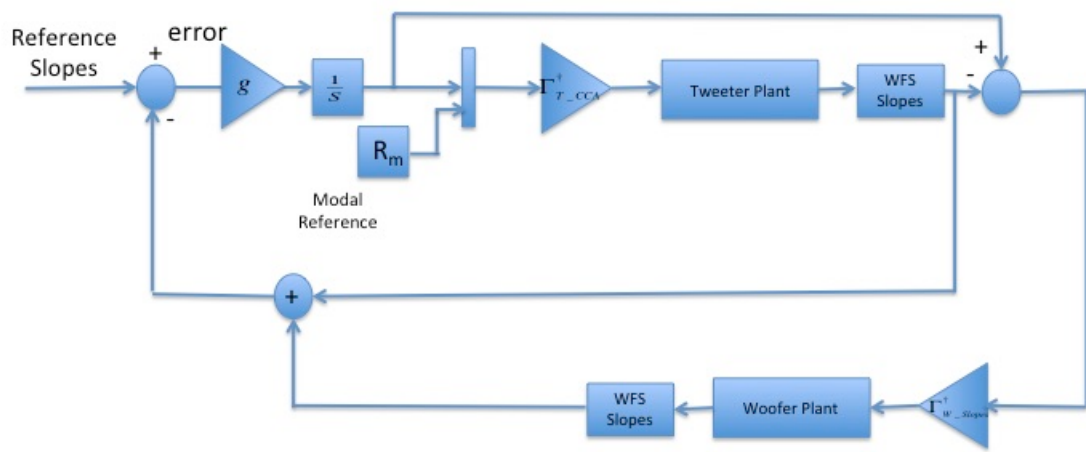
Figure 51. Confinement correction algorithm controller block diagram

(3) Distributed Modal Control

Another technique is to remove modes from the influence matrices using projection matrices. Several techniques to separate woofer-tweeter modes using distributed modal control (DMC) have been proposed in [39], [66], [79]. This section presents a technique by presented by Conan et al. [66].

Specific modes like tip, tilt, and piston can be removed from the influence matrices to reduce the likelihood of saturation due to these modes. This can also decouple the woofer and tweeter modes by removing the influence functions of one mirror from the other. The resulting influence matrices are inverted to form two reconstruction matrices used in an integral feedback controller.

Removing the woofer modes from the tweeter prevents the tweeter from reproducing woofer modes. A projection matrix of the tweeter in woofer space, P_t, is found using equation (4.36) where the tweeter is projected into woofer space. The tweeter DM modal basis is then found using equation (4.37). The woofer modes are removed from the tweeter using equation (4.38) resulting in a new influence matrix Γ_{T_WR}. In a similar manner one can remove the tweeter modes from the woofer, however as seen in the example singular value plot, Figure 48, the woofer's influence on higher order modes is negligible.

$$[P_T] = [\Gamma_W]^\dagger [\Gamma_T] \tag{4.36}$$

$$[B_T] = [I] - [P_T]^\dagger [P_T] \tag{4.37}$$

$$[\Gamma_{T\_WR}] = [\Gamma_T][B_T] \tag{4.38}$$

Removing the woofer modes from the tweeter helps prevent tweeter saturation. In most AO applications the tweeter operates at a higher bandwidth than the woofer causing the tweeter to apply the initial correction and then allowing the woofer to slowly remove the lower order modes. This causes the tweeter to initially saturate. However, this method does not allow the woofer and tweeter to share dynamic range for modes covered by both mirrors. This is undesirable for AO systems where the combined stroke of the woofer and tweeter is required.

2. Woofer-Tweeter Open-Loop Control

The global iterative constrained minimization previously discussed presents the idea of applying an optimal control approach to the SMT and deformable mirror control system. However, this technique assumes the quasi-static model of the SMT segments and deformable mirror is an accurate representation of the physical hardware. The constrained quadratic cost function was already presented and used in the iterative constrained least squares controller to prevent actuator saturation while minimizing the RMS wavefront error. This section presents other cost functions.

RMS wavefront error is a good characterization of optical quality. Peak-to-valley wavefront error is also important especially when trying to reduce wavefront discontinuities between segment edges or reducing the wavefront error to within the

85

capture range of a wavefront sensor. Peak-to-valley wavefront error is introduced into the cost function below where ϕ is the wavefront represented as a vector from equation (4.9), and c_1 and c_2 are weighting coefficients.

$$\arg\min J(u) = \frac{1}{2}\left(c_1\left(\{\phi\}^T\{\phi\}\right) + c_2\left(\max\left(\{\phi\}\right) - \min\left(\{\phi\}\right)\right)\right)_2^2$$

$$\text{subject to: } lb \leq \{u\} \leq ub$$

(4.39)

The cost function can be reformulated to include a cost for peak-to-valley wavefront error as well as other control constraints. Previous work by Redding [80] investigated adding actuator penalties to the cost function. These penalties are intended to preserve actuator stroke by penalizing the deviation of the new control signal from the previous control signal, v_Δ, and the magnitude of the control change.

$$\arg\min J(u) = \frac{1}{2}\left(c_1\left(\{\phi\}^T\{\phi\}\right) + c_2\left(\max\left(\{\phi\}\right) - \min\left(\{\phi\}\right)\right) + c_3\left(\{v_\Delta\}^T\{v_\Delta\}\right) + c_4\left(\{u\}^T\{u\}\right)\right)$$

$$\text{subject to: } lb \leq \{u\} \leq ub$$

(4.40)

The cost function above is re-written in terms of the control variable u using the SMT and deformable mirror influence matrices. The control signal is found at the stationary point where the derivative of J is equal to zero and the constraints are met. These points are found using MATLAB's *lsqlin.m* function for the constrained least squares problem described previously, and *fmincon.m* for the nonlinear cost functions.

3.   Adaptive Influence Matrix

The SMT active mirrors are considered linear systems and use traditional adaptive optic control techniques like an influence matrix to relate actuator inputs to sensor outputs. The model may vary from the physical hardware, or there may be regions of operation where the active mirror behavior is not linear. This research proposes an approach to improve correction of an active space telescope primary mirror by iteratively updating the influence matrix. This approach may be advantageous for improving wavefront error on orbit without having to recollect influence functions saving precious collection time.

The adaptive influence matrix technique is developed using a modal influence matrix. The influence matrix and sensor outputs are represented as SVD modal

86

coefficients. Equation (4.41) is the SVD factorization of the influence matrix. Equation (4.42) makes the influence matrix orthogonal and equation (4.43) converts the influence matrix to SVD modal coefficients. Equation (4.44) converts the measured output to modal coefficients.

$$[\Gamma] = [U][\Sigma][V]^T \tag{4.41}$$

$$[\hat{\Gamma}] = [\Gamma][V] \tag{4.42}$$

$$[\tilde{\Gamma}] = [\hat{\Gamma}]^\dagger [\Gamma] \tag{4.43}$$

$$\{a\} = [\hat{\Gamma}]^\dagger \{y\} \tag{4.44}$$

The influence matrix update begins by predicting the output using equation (4.45) and measuring the output. The prediction and measurement error is computed using equation (4.46). A quadratic cost function compares the measured wavefront output and predicted wavefront output error, equation (4.47). The gradient of the cost function with respect to the influence matrix, equation (4.48), is used to update the influence matrix. The influence matrix is using updated using equation (4.49) where the gradient is multiplied by a small gain and added to the previous influence matrix. The gain μ is empirically chosen to be small in order to slowly change the influence matrix. This process is repeated several times incrementally reducing the cost function J. The control algorithm uses the updated influence matrix.

$$\{\hat{a}_j\} = [\tilde{\Gamma}]\{u_j\} \tag{4.45}$$

$$\{z_j\} = \{a_j\} - \{\hat{a}_j\} \tag{4.46}$$

$$J = \{z_j\}^T \{z_j\} \tag{4.47}$$

$$\left[\frac{\partial J}{\partial \tilde{\Gamma}_j}\right] = -2\{a_j\}\{u_j^T\} + [\tilde{\Gamma}_j]\left(2\{u_j\}\{u_j\}^T\right) \tag{4.48}$$

$$[\tilde{\Gamma}_{j+1}] = [\tilde{\Gamma}_j] + \mu\left[\frac{\partial J}{\partial \tilde{\Gamma}_j}\right] \tag{4.49}$$

The influence matrix update is equivalent to multiplying the static modal influence matrix by a weighting matrix, equation (4.50). The modal basis of the feedback is not updated. Equation (4.51) shows the updated influence matrix included in the controller update equation from in Chapter II where the error is represented in SVD modal coefficients.

$$[\tilde{\Gamma}_{j+1}] = [\tilde{\Gamma}_j][Q_j] \tag{4.50}$$

87

$$\{u_{k+1}\} = g_1\left[\tilde{\Gamma}_{j+1}\right]^\dagger\left(\{a_0\} - \{a_k\}\right) + \{u_k\} \tag{4.51}$$

C.   CONCLUSIONS

This chapter presented the current segmented mirror telescope wavefront sensing and control approach for the SMT and described the coarse alignment, coarse phasing and fine phasing techniques. Existing woofer-tweeter control techniques were discussed and a new gradient woofer-tweeter control technique using singular value weighting was introduced. A new influence matrix update technique was also presented to improve wavefront correction due to variations between the model and physical system.   The controller developments presented in this chapter along with the models presented in Chapter III allow computer simulation of the control techniques for the SMT and the SMT segment woofer-tweeter system. The results from these simulations are presented in the next chapter.

V.   SIMULATION RESULTS

This chapter presents the simulation results of the models and controllers developed in the earlier chapters. First the chapter presents a wavefront sensing and control simulation results for the entire SMT using measured SMT segment surface error data in the initial conditions. Next segment level fine phasing is conducted because it represents the experimental setup in Chapter VI. The segment fine phasing controllers include an integral controller, iterative minimization controller, and gradient controller. The segment level control simulation results show that the wavefront error could be improved using a deformable mirror. The chapter then presents the fine phasing improvement results including closed loop woofer-tweeter control, open loop woofer-tweeter control, and the adaptive influence matrix model update technique. These results are presented to assess the capability of the controllers prior to applying them to the experimental test bed in the next chapter.

A.   SMT WAVEFRONT CONTROL

These results show the predicted wavefront error at each control step from coarse alignment to fine phasing. The simulation is different from previous SMT control simulations because wavefront sensing and control had been simulated from deployment through fine phasing using measured segment surface figure error data in the initial conditions. Including the actual segment surface errors demonstrates the wavefront sensing and control challenges of the current SMT system and reinforces the need to improve the primary mirror surface error. For example, this simulation shows that the current SMT Shack-Hartmann wavefront sensor does not have enough spatial resolution to reduce the segment surface error within the capture range of the phase diversity sensor (< 1 wave peak-to-valley). The simulations also predicted that even with a better sensor the current SMT segments could not reduce the peak-to-valley error to perform phase retrieval using the phase diversity sensor. These results support the need to either improve the existing SMT segments or add an additional deformable mirror to the optical path.

The SMT wavefront sensing and control simulation is broken into the three sequential control approaches: coarse alignment control, coarse phasing control, and fine phasing control. The SMT wavefront sensing and control simulation begins after segment stacking. The resulting RMS wavefront error after segment stacking is on the order of 100s of μm. Figure 52 shows a pre-stacking OPD with a RMS wavefront error of 49.8 waves and the post staking OPD with a RMS wavefront error of 48.5 waves. The stacking process drives the tip and tilt of the segments so their sub-images overlap. The coarse alignment phase continues to align the segments in tip and tilt as well as removes the piston mismatch between the segments.
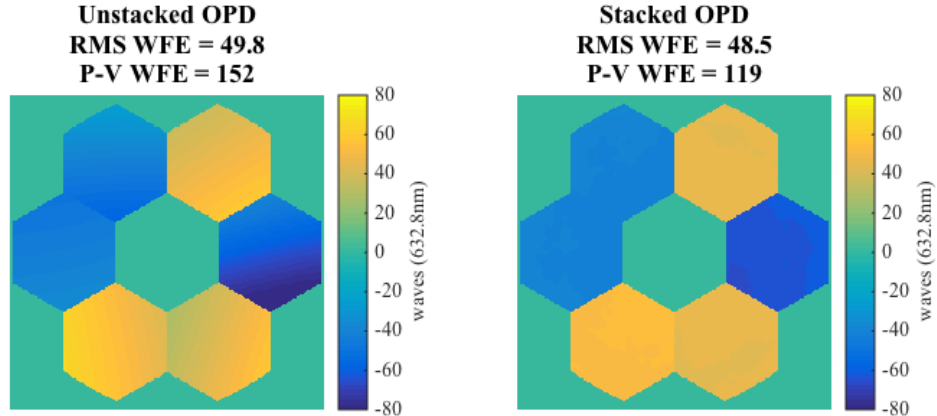

Figure 52. Alignment and segment stacking OPD before (left) and after (right)

1. Coarse Alignment

The stacked sub-image in Figure 53 shows a large amount of blurring at the focal plane. This is due to the segment piston error and surface imperfection of the individual segments. An initial surface correction is applied to the segments using the Shack-Hartmann wavefront sensor and the segment FSAs. The Shack Hartmann wavefront sensor does not observe the piston mode allowing us to correct for the SMT segment surface without correcting the piston. Figure 54 shows the resulting OPD after surface correction and the image at the focal plane with much less scattering shown in the previous figure. Figure 55 shows the OPD with piston removed before and after surface figuring using the Shack-Hartmann wavefront sensor.
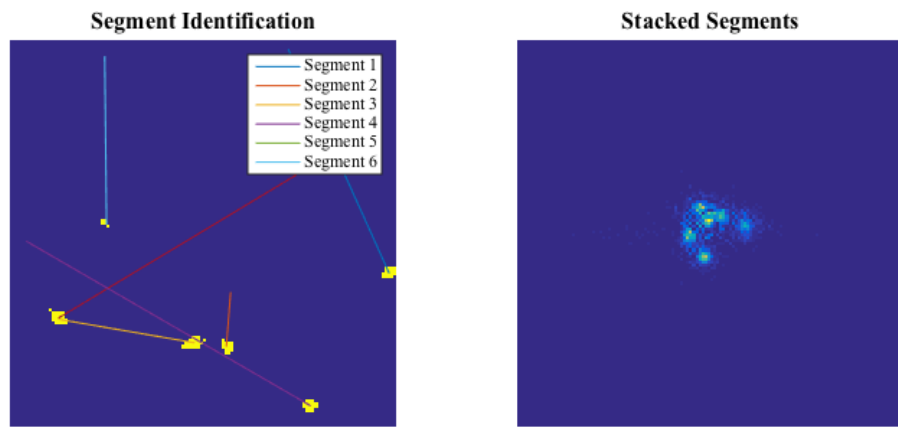
Figure 53. Segment identification (left) and stacked segment sub-images (right)
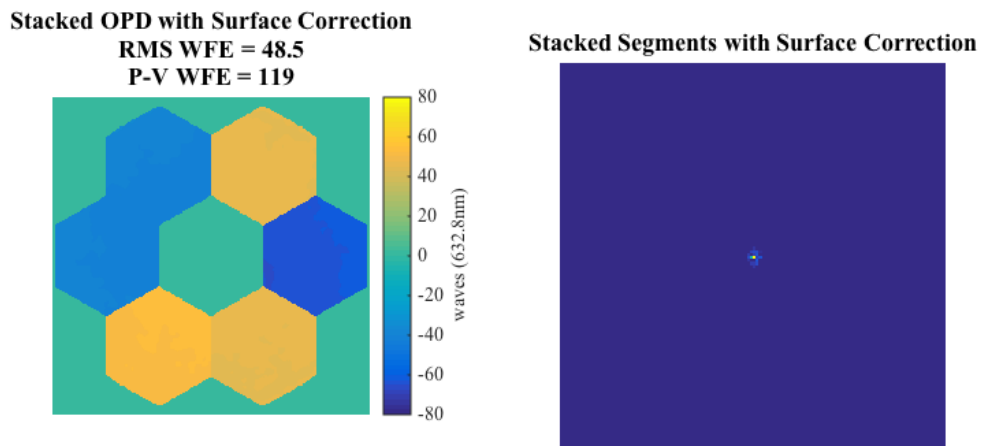
Figure 54. Initial segment surface correction using the Shack-Hartmann
wavefront sensor and segment FSAs
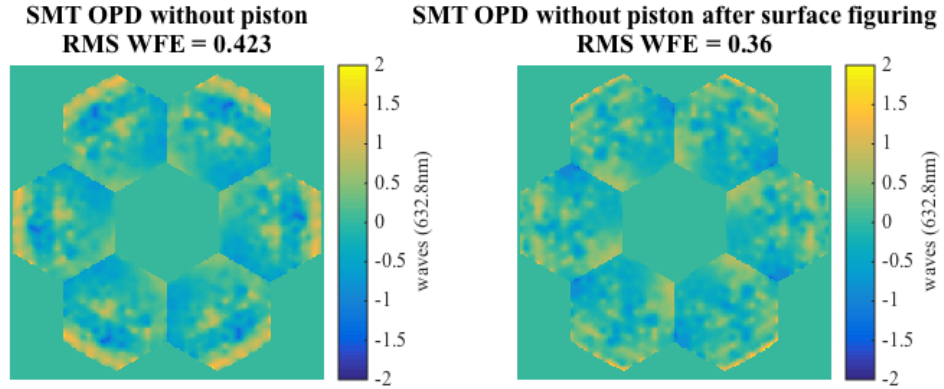
Figure 55. OPD with piston removed before surface figuring (left) and after surface figuring (right)

The next step uses the CCAs with feedback from the edge sensors. The dynamic model and LQG controller developed in Chapter III and IV are used to drive the edge sensor error toward zero. The Q matrix is set as a diagonal matrix of the dynamic model's A matrix singular values. This places greater emphasis on the higher order mode shapes when correcting the SMT surface. The R matrix is set equal to the identity matrix. Figure 56 shows the resulting OPD after coarse alignment along with a time history of the edge sensor displacements.
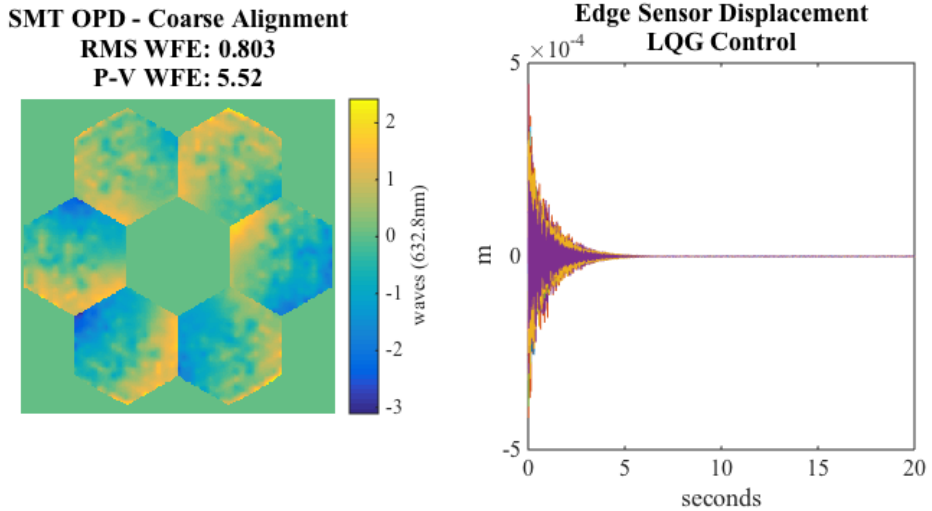
Figure 56. OPD after coarse alignment using CCAs (left), edge sensor displacement history during LQG control (right)

2. Coarse Phasing

The coarse phasing step begins after the coarse alignment and assumes the CCA coarse alignment continues to track the steady state edge sensor displacements. The coarse phasing uses the FCA with feedback from the edge sensors to further align the segments. Figure 57 shows that the coarse phasing continues to improve both the RMS wavefront error and peak-to-valley wavefront error due to the fine control steps of the FCAs.
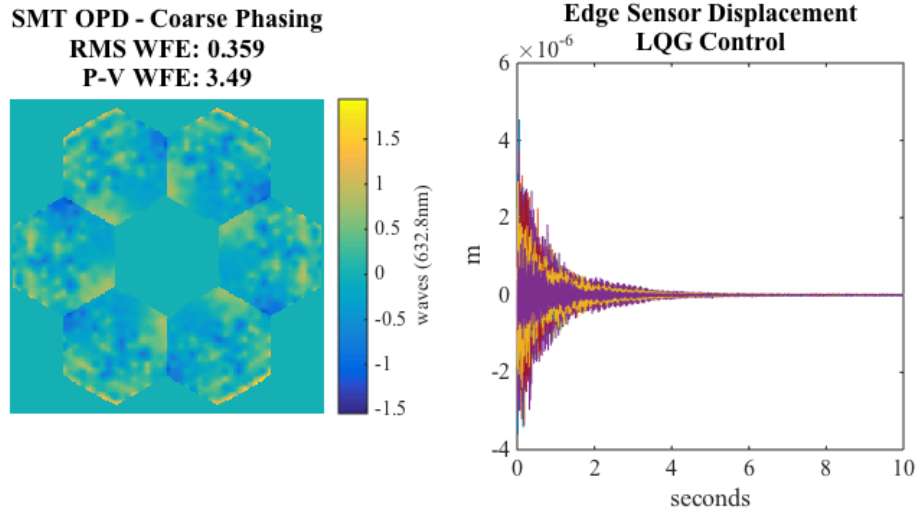
Figure 57. OPD after coarse phasing use FCAs (left), edge sensor displacement history during LQG control (right)

3. Fine Phasing

The fine phasing routine uses both the Shack-Hartmann wavefront sensor and phase diversity sensor to measure the OPD. This simulation uses the SMT segment quasi-static model and the control inputs are found using a constrained least squares routine. The peak-to-valley wavefront error is high due to surface imperfections of the AHM segments. This does not prevent phasing the segment edges. Figure 59 shows the piston, tip, and tilt of the wavefront prior to fine phasing and the edges are phased to within $\lambda/4$. However, the surface peak-to-valley wavefront error exceeds 1 wave and is not within the capture range of the phase retrieval algorithm. In this simulation we ignore this problem by feeding back the OPD output of quasi-static dynamic model to predict the performance of the segments.

There are two problems causing the high peak-to-valley wavefront error. The first is the capability of the SMT AHM mirror and the second is the Shack-Hartmann mask spatial resolution. The Shack-Hartmann spatial resolution is not sufficient to estimate the segment high spatial frequency residual errors. However, when using the OPD from the quasi-static dynamic model as feedback, the peak-to-valley wavefront

94

error still exceeds 1 wave. This shows that the current system segments do not have the actuator density to correct the segment residual errors.
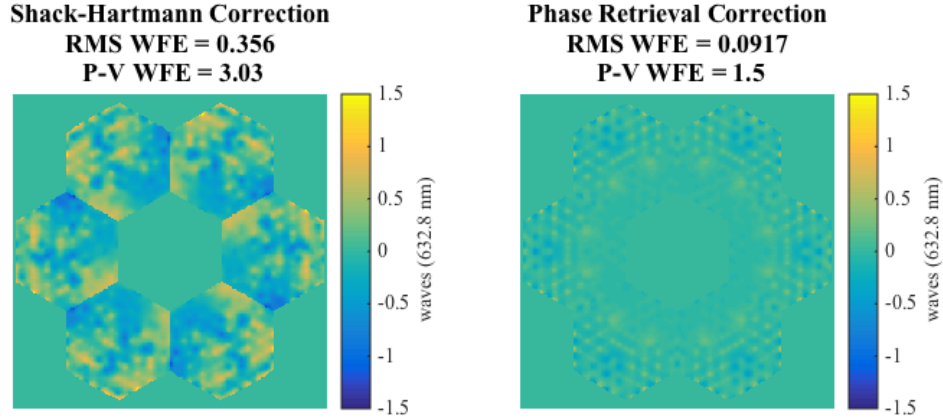
Figure 58. OPD after surface correction using Shack-Hartmann wavefront sensor (left), OPD after surface correction using phase retrieval
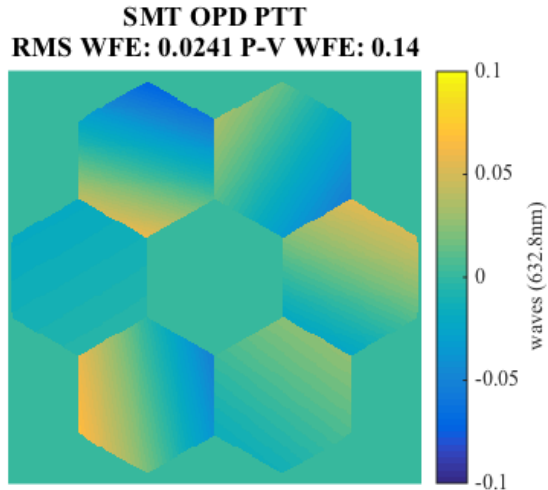
Figure 59. SMT OPD piston, tip, tilt only prior to fine phasing

B.   SMT SEGMENT CONTROL SIMULATION

The SMT test bed can only measure a single AHM segment in the experimental setup.   Therefore this section presents control simulations of a single segment using integral control, iterative constrained minimization control, and gradient control. These simulations are used as a baseline to compare the performance of the single segment

woofer-tweeter simulations. The results below show the constrained minimization and gradient control technique outperforms the integral controller. The controllers are simulated using 100 Monte-Carlo runs where the noise is varied. The update gain for the integral control and iterative minimization was 0.2.

Figure 60 shows the mean error history with the standard deviation represented as error bars. The integral controller and iterative constrained minimization technique have similar results with the integral controller experiencing integral windup toward the end of the simulation and the constrained minimization outperforming the integral controller. The gradient control technique shows improved performance over the other two controllers. Despite the improved performance of the gradient control technique the overall surface error is still about $\lambda/5$ waves RMS requiring more surface error improvement supporting the addition of a deformable mirror to the optical telescope assembly.
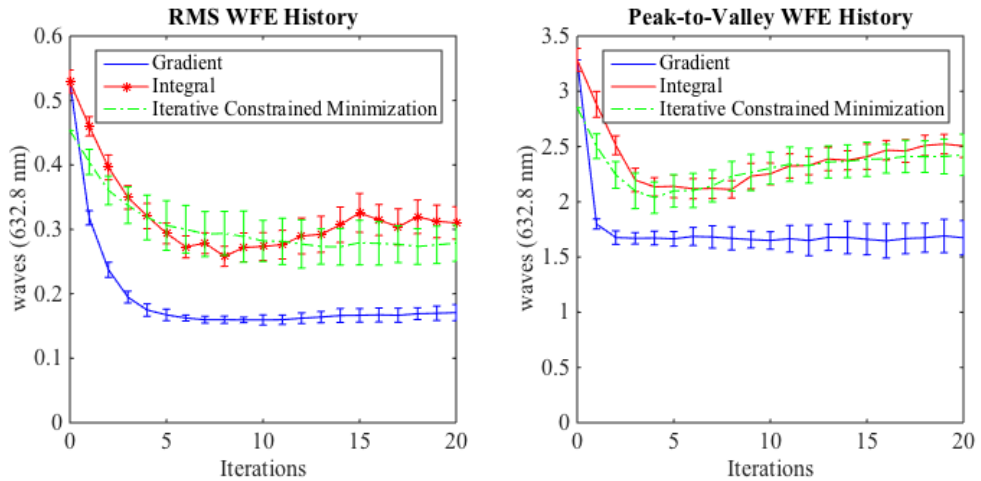

Figure 60. Simulated SMT segment error history using gradient control,
integral control, and iterative constrained minimization

This was the first time the gradient control technique was simulated with a SMT AHM segment. The baseline simulation results show that the gradient control technique improved the steady state SMT AHM mean RMS surface error by 38% and mean peak-

to-valley surface error by 32% compared to the SMT iterative minimization controller. These simulation results are significant because current AHM control does not use gradient control techniques.

C.   FINE PHASING IMPROVEMENT SIMULATION

This section presents three simulated approaches to improve the SMT fine phasing wavefront error. These simulations assume that coarse alignment, and coarse phase are complete. The first approach simulates an additional deformable mirror in a closed loop woofer-tweeter configuration. The second approach simulates open loop optimal control techniques to correct residual surface error with the woofer-tweeter system. The third simulates the adaptive influence matrix technique to improve the performance of the SMT AHM model and improve the fine phasing residual wavefront error.

1.   Woofer-Tweeter Closed-Loop Control

This section presents the closed loop simulated feedback woofer-tweeter controllers from Chapter IV. The results show that the global woofer-tweeter controller and the gradient controller outperform the traditional modal and offload woofer-tweeter control techniques for the woofer-tweeter configuration. The simulation results also show the global woofer-tweeter controllers significantly improve wavefront error compared to a serial sequential woofer-tweeter constrained minimization controller.

The woofer-tweeter system simulated is a single SMT segment configured as the woofer and the BMC 140 actuator deformable mirror as the tweeter. Only 61 of the 140 BMC deformable mirror actuators are used as described in Chapter III. The simulations used a static bias as the initial condition of the SMT segment. The influence matrix models from Chapter III are used to model the woofer-tweeter system. Saturation limits are placed on the SMT FSAs and the BMC deformable mirror actuators limiting the available actuator stroke. Plant noise and sensor noise are introduced by adding zero mean Gaussian noise to the actuator inputs and OPD output.

The woofer-tweeter controllers are compared against the SMT controller simulations presented earlier, a serial woofer-tweeter controller, and a tweeter only controller. The serial woofer-tweeter controller applies iterative constrained minimization control to the woofer, and then applies iterative constrained minimization control to the tweeter. The tweeter only controller is similar to the results presented in [64].

The controllers are simulated using 100 Monte Carlo runs and the mean steady state RMS and peak-to-valley wavefront error are presented. Appendix A contains error history plots showing the mean error with standard deviation error bars for the different controller simulations. Figure 61 shows the different controller steady state mean RMS wavefront error, and Figure 62 shows the steady state mean peak-to-valley wavefront error.
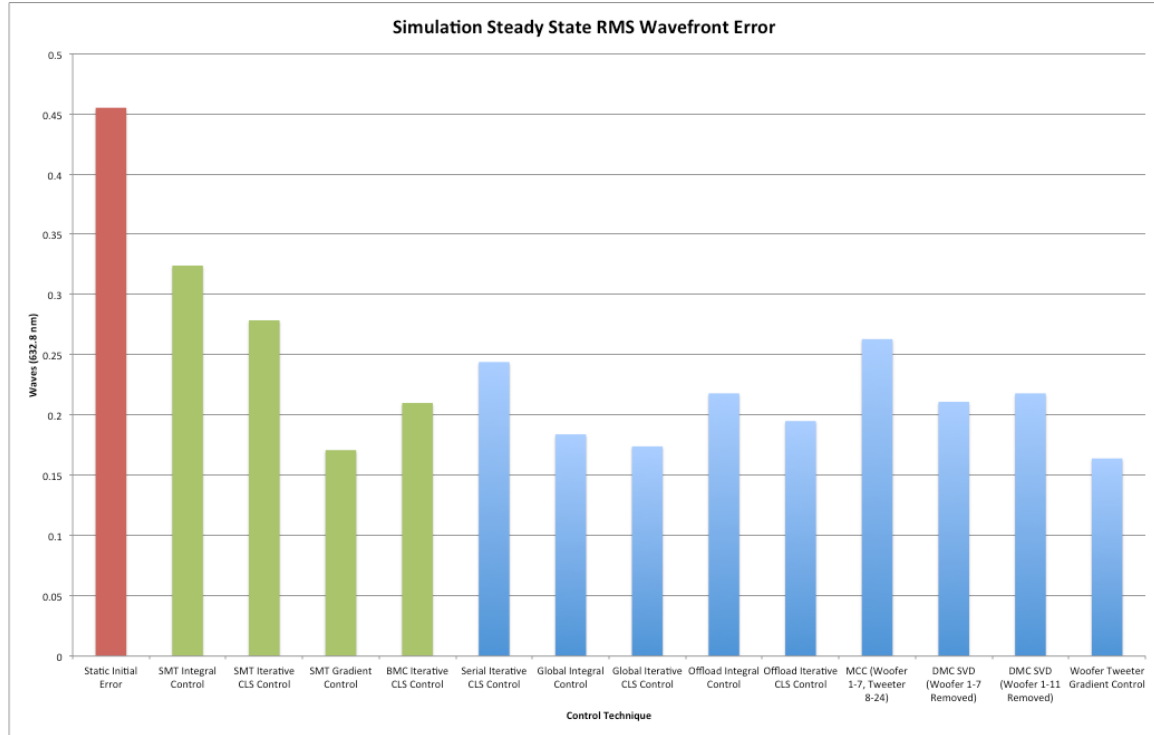

Figure 61. Simulation of feedback controllers for woofer-tweeter system, RMS steady state mean wavefront error the initial error is shown in red, single mirror control shown in green, and woofer-tweeter control shown in blue

98
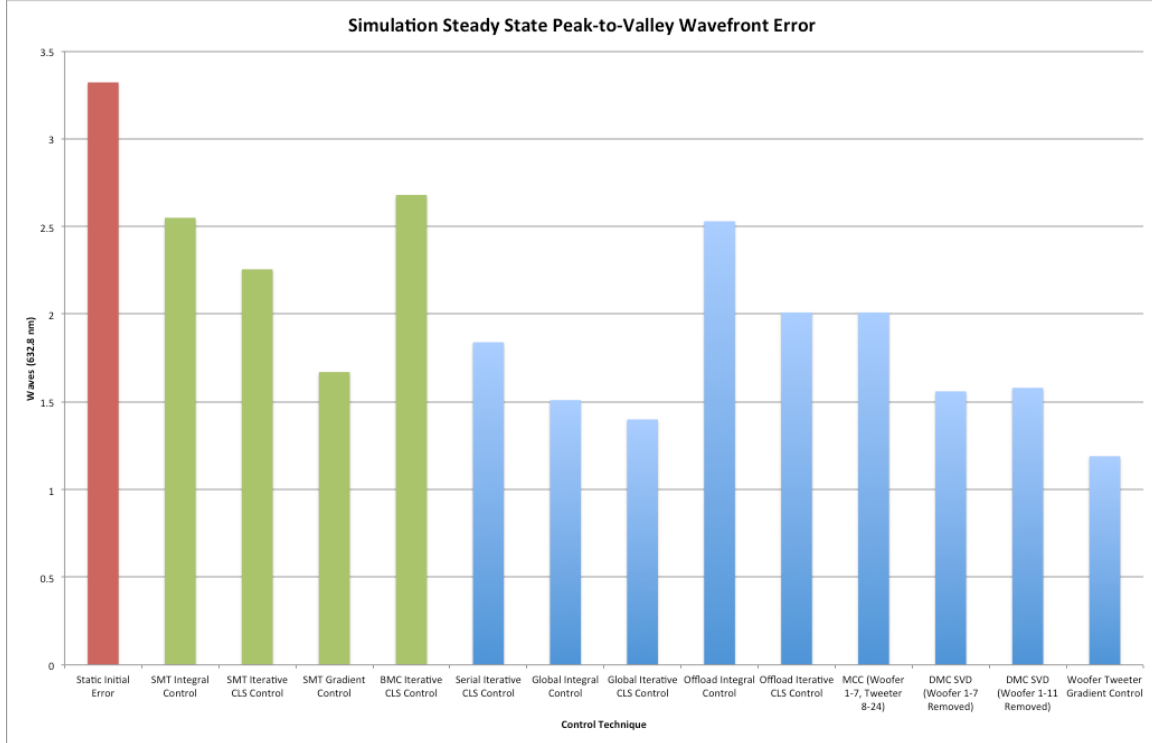
Figure 62. Simulation of feedback controllers for woofer-tweeter system, peak-to-valley steady state mean wavefront error the initial error is shown in red, single mirror control shown in green, and woofer-tweeter control shown in blue

a. *Serial Simulated Control*

The serial woofer-tweeter controller uses two sequential iterative constrained least squares control loops to correct the woofer and then correct the tweeter. Figure 63 shows the simulated serial woofer-tweeter controller error history where the SMT segment applied correction and then the deformable mirror applied correction. The final wavefront error plot above shows that that the serial woofer-tweeter controller improves the RMS wavefront error more than the SMT integral and constrained minimization control techniques. However the serial woofer-tweeter controller does not perform as well as the SMT gradient control or the tweeter only control when comparing RMS wavefront error.

The under performance of the serial controller compared to tweeter controller indicates that the initial condition of the controller can impact performance. The tweeter only control and the tweeter portion of the serial control are the same, but the initial

99

conditions are different. The wavefront error after applying the woofer controller has high spatial frequency errors that are not present at the SMT biased position. The BMC-140 tweeter cannot correct these errors. These results show that a better control strategy can be applied to reduce the overall wavefront error.
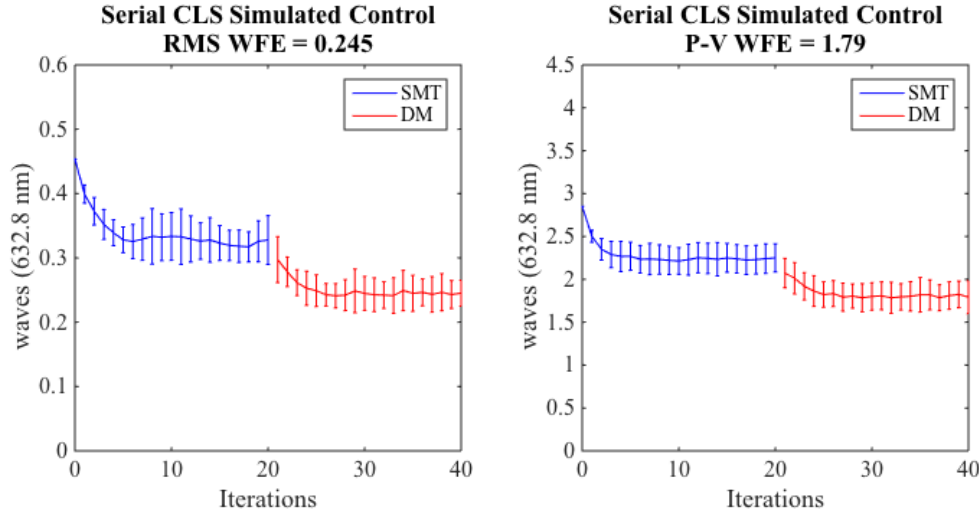

Figure 63. Simulated woofer-tweeter serial control

b. *Global Simulated Control*

The global influence matrix control techniques included the global integral controller, global iterative constrained minimization controller and the woofer-tweeter gradient controllers. All three global influence matrix controllers showed significant improvement in wavefront error compared to a serial woofer-tweeter constrained minimization control approach. The woofer-tweeter gradient controller was the only global controller to outperform the SMT gradient controller in both residual RMS and peak-to-valley wavefront error. Figure 64 compares the error history of the simulated global influence matrix control results.
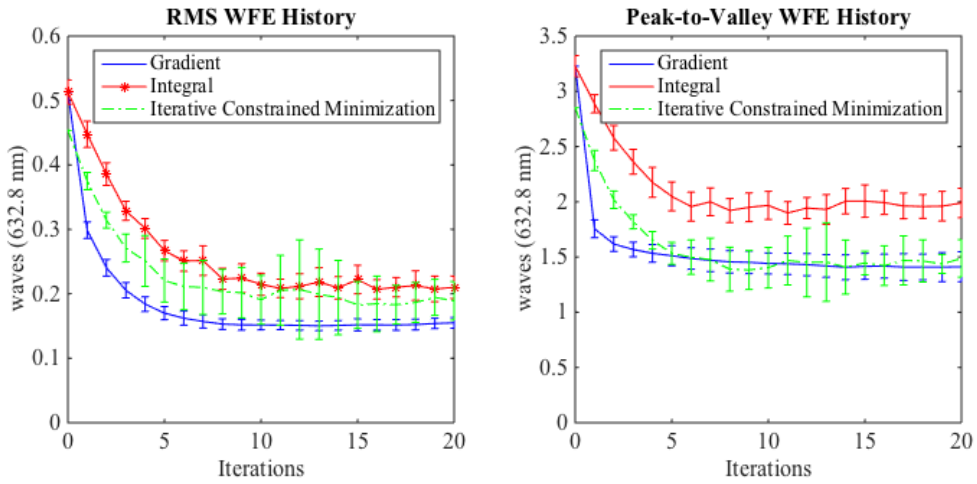
Figure 64. Simulated woofer-tweeter error history using gradient control, integral control, and iterative constrained minimization

c. *Offload Simulated Control*

The offload controllers did improve the RMS wavefront error compared to the serial woofer-tweeter controller, but did not perform as well as the global woofer-tweeter controllers. The offload control technique projected the tweeter commands into the woofer commands. The result was a controller that could not take full advantage of the woofer capabilities limiting the total stroke of the system resulting in poor performance in this simulation.

d. *Modal Simulated Control*

The modal coefficient control (MCC) technique did not reduce the RMS wavefront error below the baseline serial woofer-tweeter controller. The MCC controller used Zernike modes as a common basis and spatially separated the correction based on Zernike modes. This approach did not allow the two mirrors to work together to correct the same mode shapes reducing the overall correction capability available from the two mirrors.

The distributed modal control (DMC) technique was simulated for two scenarios. The first simulation removed the first 7 woofer SVD modes from the tweeter, and the second scenario removed the first 11 woofer SVD modes from the tweeter. These two

101

simulations performed better than the offload and MCC techniques because the controller used the full capability of the woofer. Removing more woofer modes from the tweeter improved the performance by making more tweeter stroke available to remove higher spatial frequency errors.

The coefficient confinement algorithm (CCA) was not simulated because the simulation used the Shack-Hartmann wavefront sensor as feedback to measure the wavefront slopes. Figure 65 shows that the controller drives the Shack-Hartmann wavefront slopes toward zero. However, the resulting wavefront obtained from the quasi-static model shows significant residual wavefront error, Figure 66. This is because the spatial resolution of the Shack-Hartmann wavefront sensor was not high enough to accurately estimate the SMT segment and deformable mirror response between the lenslet locations.
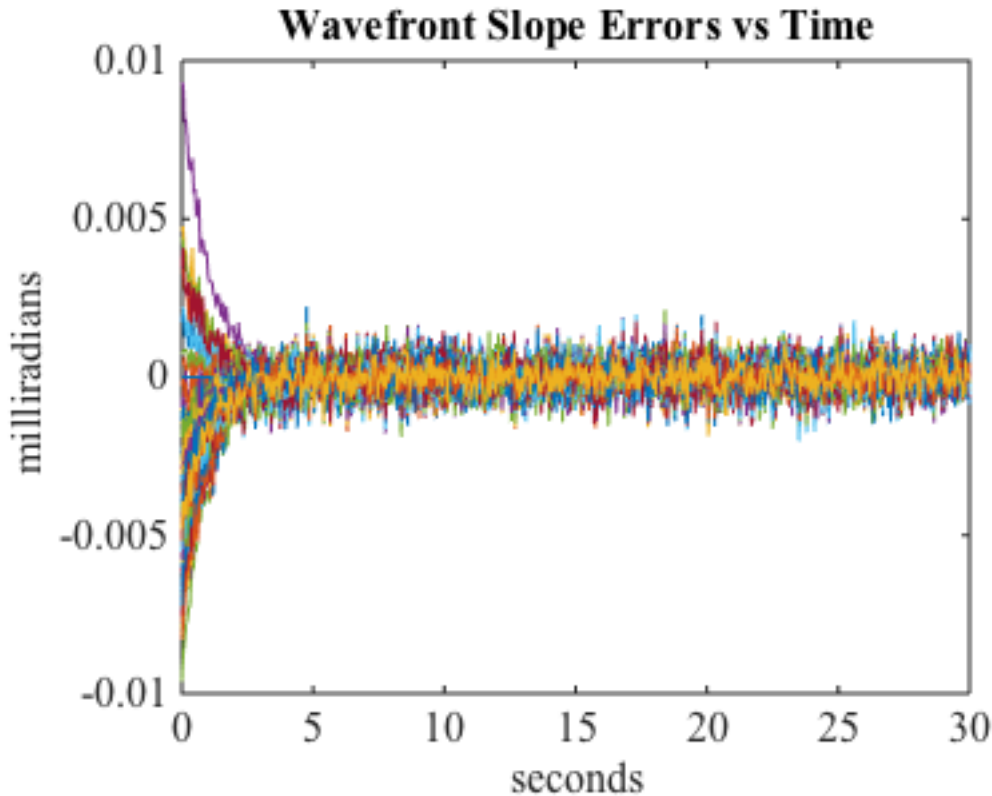
Figure 65. Coefficient Confinement Algorithm (CCA) slope error history
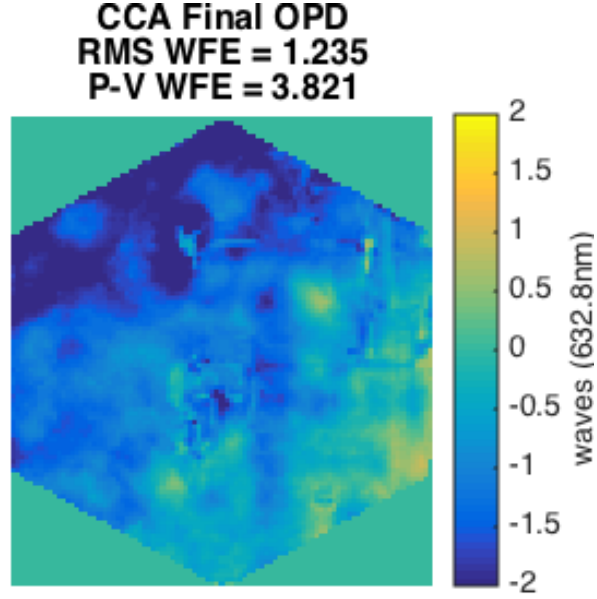
Figure 66. Final wavefront error (waves) after apply CCA to the SMT woofer-tweeter simulation

2. Woofer-Tweeter Open-Loop Control Simulation

This section presents the simulation results from the open loop control approaches applied to a single SMT AHM segment and the woofer-tweeter system. Three open loop minimization controllers were simulated with cost functions shown below. These are the cost functions presented in Chapter IV with the exception of (5.3) where the penalty on the change in the control signal was removed to simplify the minimization. The variable ϕ is the wavefront represented as a vector from equation (4.9). Then minimization for the SMT uses the SMT segment influence matrix, and the woofer-tweeter minimization uses the global influence matrix.

$$\arg\min J(u) = \frac{1}{2}\left(\{\phi\}^T\{\phi\}\right)$$

$$\text{subject to: } lb \leq \{u\} \leq ub$$

(5.1)

$$\arg\min J(u) = \frac{1}{2}\left(c_1\left(\{\phi\}^T\{\phi\}\right) + c_2\left(\max(\{\phi\}) - \min(\{\phi\})\right)\right)$$

$$\text{subject to: } lb \leq \{u\} \leq ub$$

(5.2)

$$\arg\min J(u) = \frac{1}{2}\left(c_1\left(\{\phi\}^T\{\phi\}\right) + c_2\left(\max(\{\phi\}) - \min(\{\phi\})\right) + c_3\left(\{u\}^T\{u\}\right)\right)$$

$$\text{subject to: } lb \leq \{u\} \leq ub$$

(5.3)

The solution to the first cost function (5.1) was used as the initial guess to the minimization routine for the other two cost functions. The simulations applied equal weights to the wavefront errors and a smaller weight to control penalty so the cost is not dominated by control. However, these weights can change to achieve different results. Figure 67 and Figure 68 show the simulated open loop results for both the SMT correction and global woofer-tweeter correction. The results for cost function (5.1) closely matched the SMT and woofer-tweeter iterative least squares results as expected. The results using cost function (5.2) also matched the weighting where the RMS wavefront error was worse than using cost function (5.1), but the peak-to-valley wavefront error was improved. Cost function (5.3) results were slightly worse than the previous cost function because control was penalized.

Including the peak-to-valley penalty in the cost function was an improvement beyond previous work [80], and relevant to the SMT since the current peak-to-valley wavefront error is outside the capture range of the phase diversity sensor. However, the simulation predicted that the experimental woofer-tweeter system does not have enough actuators to reduce the peak-to-valley below 1 wave.
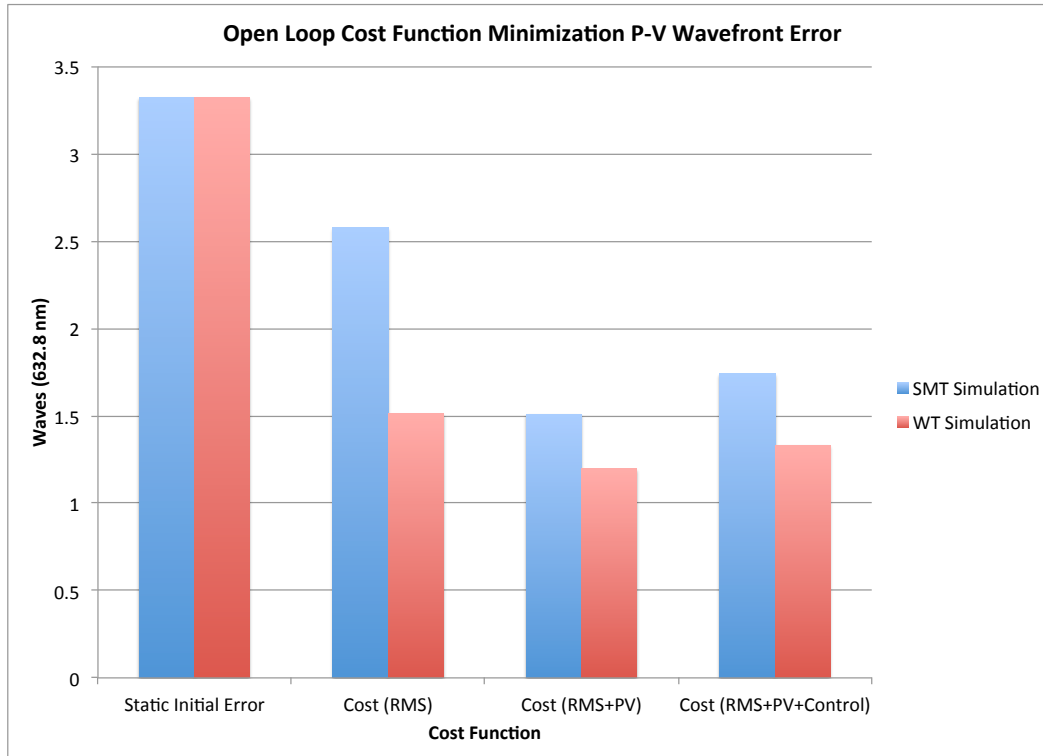
Figure 67. Open loop cost function minimization control RMS wavefront error
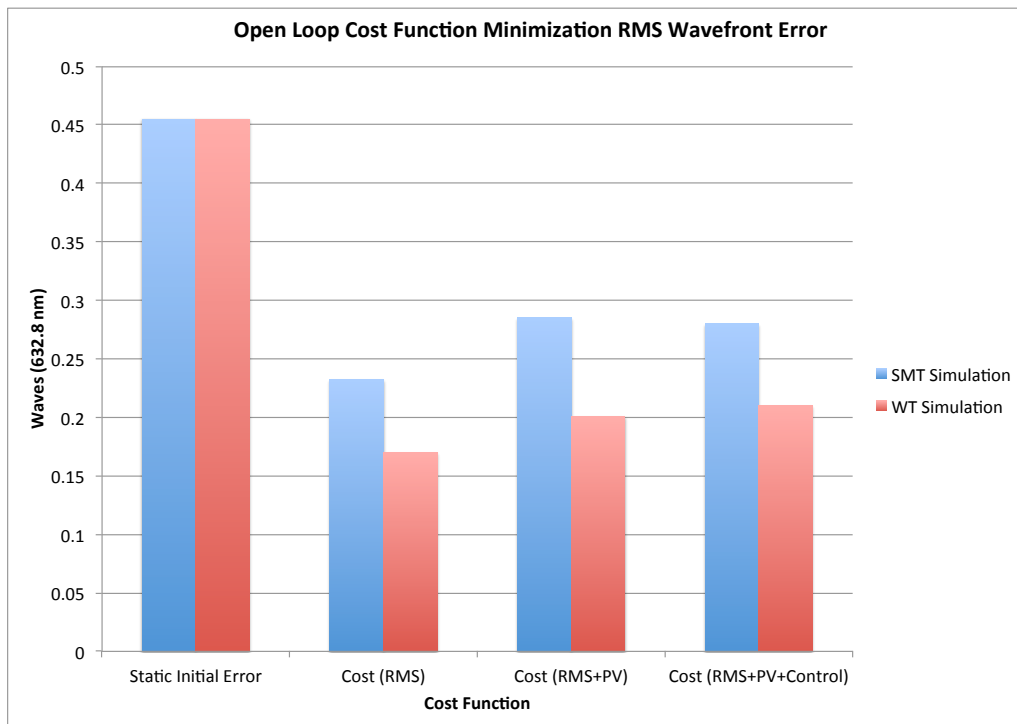
Figure 68. Open loop cost function minimization peak-to-valley wavefront error

3.   Adaptive Influence Matrix

The adaptive influence matrix can improve performance when the SMT AHM model varies from the physical hardware. To simulate the adaptive influence matrix two SMT AHM experimental influence matrices were used. The influence matrices were measured using the approach described in equations (2.5) and (2.6).   One influence matrix was measured at voltages of +/-25 volts, and another at +/-20 volts. If the mirror response was linear and there was no uncertainty in the system the influence matrices would be the same. The two influence matrices are compared by projecting the influence functions of one influence matrix onto the influence functions of the other.   If the influence matrices were the same the projection matrix should be the identity matrix. Figure 69 shows the projection matrices $\Gamma_{\pm25}^{\dagger}\Gamma_{\pm20}$.
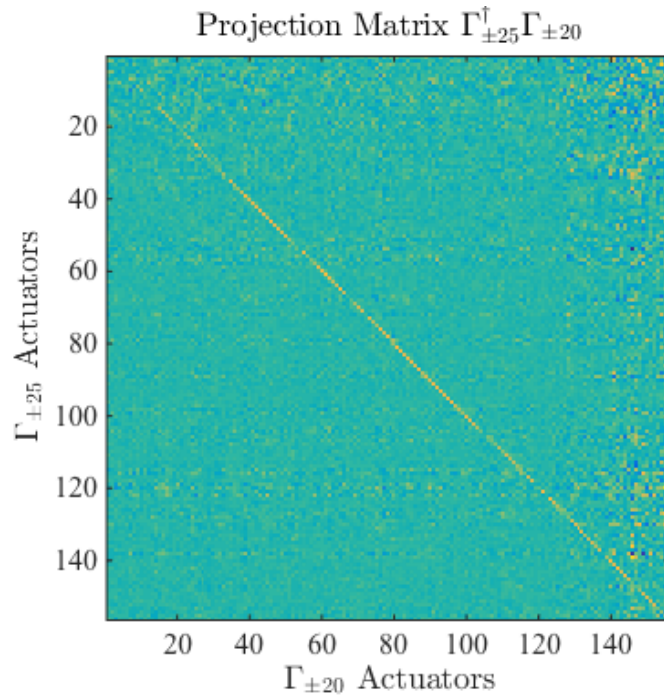

Figure 69. Projection matrix of +/- 20 volt influence matrix on +/-25 volt influence matrix

The simulation assumed the influence matrix used to control the mirror is $\Gamma_{\pm25}$, and the plant was $\Gamma_{\pm20}$. This represented uncertainty between our influence matrix and

106

our plant. The simulation ran using the SMT modal integral controller and includes the updated influence matrix. Figure 70 shows the error history without updating the influence matrix, with updating the influence matrix, and if the influence matrix matches the plant. The simulated results show that updating the influence matrix improved the RMS wavefront error, but slightly increased the peak-to-valley wavefront error. A challenge was choosing the influence matrix update gain and number of iterations to not change the influence matrix too much that the reconstruction gain matrix ($\Gamma_j^\dagger$) saturated the control voltages.
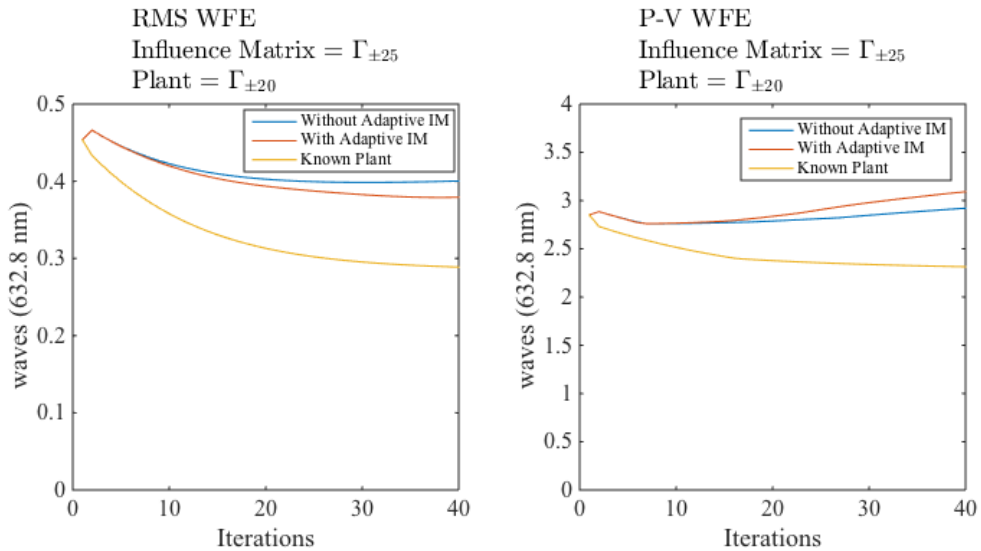

Figure 70. Error history of SMT AHM modal integral control simulation with adaptive influence matrix

D.   CONCLUSIONS

The SMT wavefront control simulation and SMT segment wavefront control simulation show that the current SMT system cannot meet the fine phasing performance required of an optical telescope. This supports the addition of a deformable mirror in a woofer-tweeter configuration to improve the residual wavefront error. The following woofer-tweeter control techniques all improved the RMS wavefront error more than the current SMT AHM constrained minimization controller: serial control, global control, offload control, and modal control.

THIS PAGE INTENTIONALLY LEFT BLANK

VI. EXPERIMENTAL RESULTS

This chapter presents experimental results from the SMT woofer-tweeter test bed. The chapter begins by describing the experimental test bed at the Naval Postgraduate School. The influence functions are developed experimentally and the SMT AHM is experimentally characterized using a three-point linearity test and by comparing influence functions over the actuator range. Next the SMT segment control results are presented including an integral controller, iterative minimization controller, and gradient controller. The SMT segment experimental results are used evaluate the woofer-tweeter results. The chapter then presents the fine phasing improvement experimental results including closed loop woofer-tweeter control, open loop woofer-tweeter control, and the adaptive influence matrix model update.

A. EXPERIMENTAL SETUP

The SMT test bed does not have a large diameter coherent light source to serve as a reference. This prevents the use of the telescope wavefront sensors. To overcome this the SMT test bed uses a center of curvature test to measure the SMT primary mirror surface error shown in Figure 71. The center of curvature test consists of a 4D Technologies Corp. PhaseCam 4020 laser interferometer with an f/3 diverging lens, a null corrector, the SMT primary mirror, and a hexapod to align the interferometer and null corrector along the SMT principle axis [16]. This experimental setup does not use the SMT optics after the primary mirror, but the primary mirror is the main source of wavefront error in the SMT system.

Adding a deformable mirror to the center of curvature test bed tests the woofer-tweeter configuration. This is achieved by adding pupil relay optics to the center of curvature test in a double pass configuration. Figure 72 shows the center of curvature test bed layout with the deformable mirror. The telescope pupil plane is relayed from the f/3 objective to the deformable mirror and then relayed to the interferometer. The entire SMT pupil plane does not fit on the deformable mirror surface. Therefore, only one segment is viewed and controlled at a time.
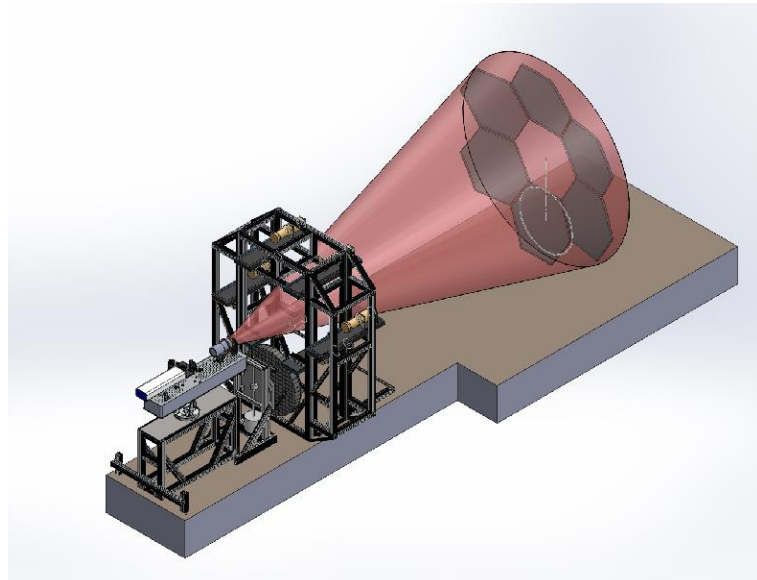
Figure 71. Center of curvature test bed, from [64]
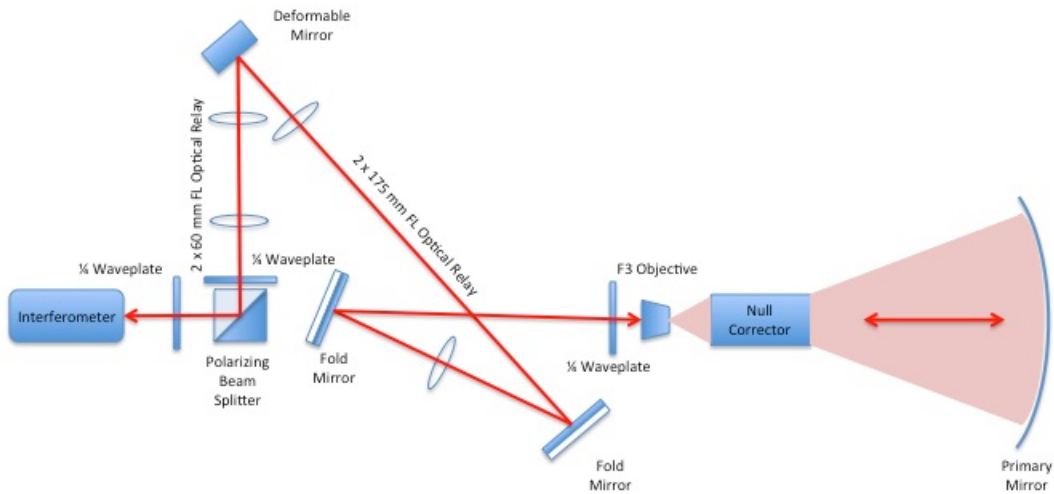
Figure 72. SMT center of curvature experimental layout, from [16]

The laser interferometer is tolerant of small structural vibrations and minor air turbulence in the test bed setup. The interferometer measures the wavefront error of the light reflected by the primary mirror in a double pass configuration and includes error contributions of all the components in the optical path. The interferometer generates a wavefront measurement averaging 10 measurements at approximately 1 Hz. The sensor

bandwidth is sufficient for the closed loop control to correct static surface errors of the primary mirror and low bandwidth disturbances [16].

The second deformable mirror is a Boston Micromachines Corporation (BMC) continuous surface 140-actuator MEMs deformable mirror. The mirror has a 3.3mm by 3.3mm square aperture, and a maximum actuator stroke of 1.8µm. The woofer-tweeter configuration uses the top SMT segment in this experiment. The BMC deformable mirror position is adjusted to place the pupil plane image of the top SMT segment on the deformable mirror. The BMC deformable mirror actuators are experimentally mapped to the SMT segment with 61 actuators having measured influence over on the SMT segment wavefront. Figure 73 shows the BMC deformable mirror actuator locations with respect to the SMT segment actuator locations at the pupil plane [16].
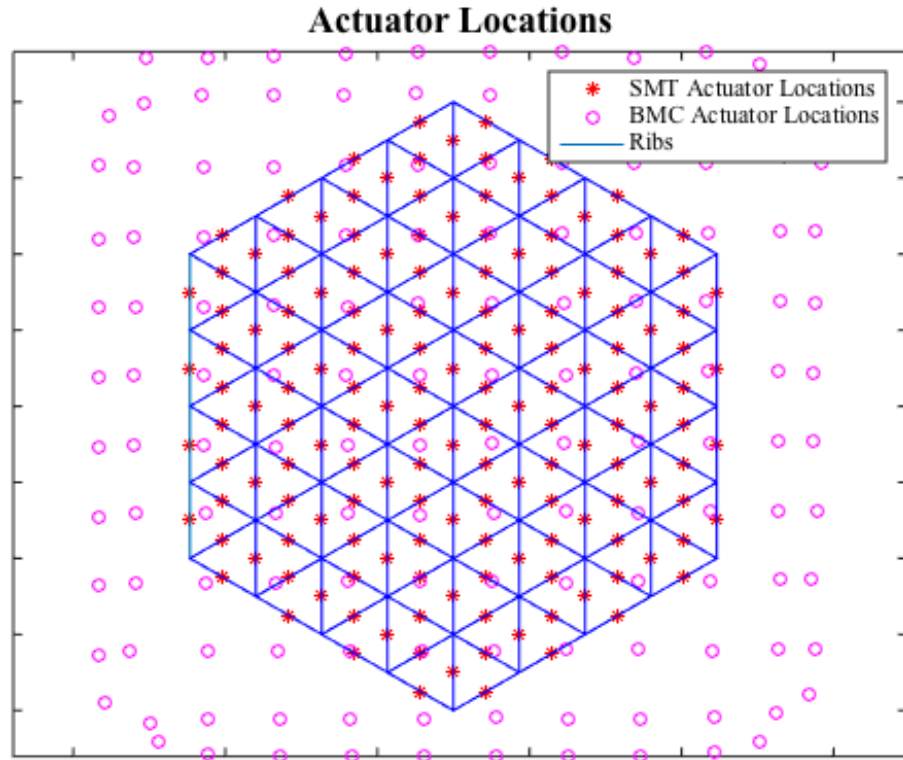

Figure 73. Deformable mirror actuator locations projected onto SMT segment

The SMT AHM and BMC deformable mirror actuators have non-linear regions. The SMT AHM actuator actuators are electrostrictive lead magnesium niobate (PMN) with a range between 0-100V and have a quadratic non-linear response. However the actuator response is near linear between the operating ranges of 20V-80V. The BMC deformable mirror actuator voltage range is from 0V-202V. The relationship between voltage and displacement for the BMC MEMs mirror is quadratic. Watson showed a linear relationship between voltage and displacement can be approximated between 20V and 180V for this particular mirror [65]. Limiters were applied to prevent commanding the mirrors outside these ranges.

A closed loop control system is built by connecting the laser interferometer, SMT AHM segment, and deformable mirror to a control computer. The laser interferometer measurements are used as feedback. The control computer uses MATLAB to retrieve the interferometer measurements and commanded the SMT segments and the deformable mirror actuators. Wavefront residual piston, tip, and tilt were removed from the wavefront measurements after aligning the optical setup. This allowed testing the woofer-tweeter fine phasing techniques without actively compensating for piston, tip, and tilt with the SMT FSAs and deformable mirror actuators.

B.   EXPERIMENTAL SYSTEM CHARACTERIZATION

Deformable mirrors are modeled as static linear devices as described in the previous sections. However data from the SMT test bed shows that the AHM mirror response does not perfectly match the linear model. This section describes the experimental influence matrices and shows actuator coupling. A three-point linearity test is presented to compare positive and negative influence functions and shows that the mirror response is not linear. Finally the influence functions are measured and compared at different voltages for a single actuator showing different responses. These variations and non-linear responses support the use of feedback control to command the SMT AHM and the woofer-tweeter system.

1.   Experimental Influence Matrices

The influence matrices were experimentally derived for the SMT segment and BMC-140 mirror using the PhaseCam 4020 interferometer to measure the mirror OPD after poking individual actuators from a biased position in both a positive and negative direction. The woofer influence function was measured by poking the actuators +/- 30V from the 50V bias. The tweeter influence function was measured by poking the actuators +/-80V from the 101V bias. Figure 74 shows the influence function coupling for the woofer influence matrix, Γ_W, and the tweeter influence matrix, Γ_T. The SMT actuator influence is highly coupled while the BMC Multi-DM actuator influence is coupled to local actuators. This is due to the surface parallel actuators of the SMT and the surface perpendicular actuators of the BMC Multi-DM.
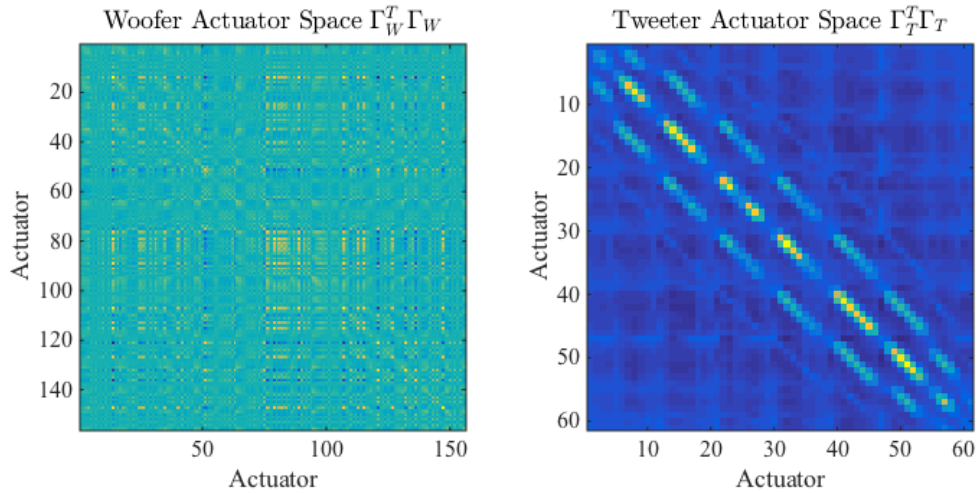
Figure 74. Woofer actuator space (left) and tweeter actuator space (right)

2.   SMT Three Point Linearity Test

The active mirror under study is a 1-meter hexagonal SiC AHM mirror with 156 face sheet actuators. The actuators are epoxied to the structural ribs of the SiC substrate in a surface parallel configuration at the 50V bias position. Activating a single actuator produces a local and global response on the mirror surface.

The linear response of the AHM actuators is investigated using a three-point linearity test. This test identifies actuators that have significantly different negative and positive responses by comparing the negative and positive influence functions measured from the 50V bias with the actuators at the extremes of their linear range. Equation (6.1) and equation (6.2) shows the positive and negative influence function respectively and the superscript represents the control voltage during the sensor measurement. The maximum absolute value of the influence function represents the maximum deflection of the surface caused by the actuator. To compare the deflections between the positive and negative influence functions the ratio between the largest and smallest deflection are taken. Figure 75 shows the ratios for the 156 face sheet actuators and ratios greater than 1 indicate a non-linear response. Measurement errors, actuator bias position errors, and anomalies in the actuator to substrate bond can cause the positive and negative influence functions to be different. The results show that 25 actuators have a response one standard deviation outside the sampled 156 actuators.

$$b_i^+ = \frac{y_i^{80} - y_i^{50}}{30}$$ (6.1)

$$b_i^- = \frac{y_i^{50} - y_i^{30}}{30}$$ (6.2)
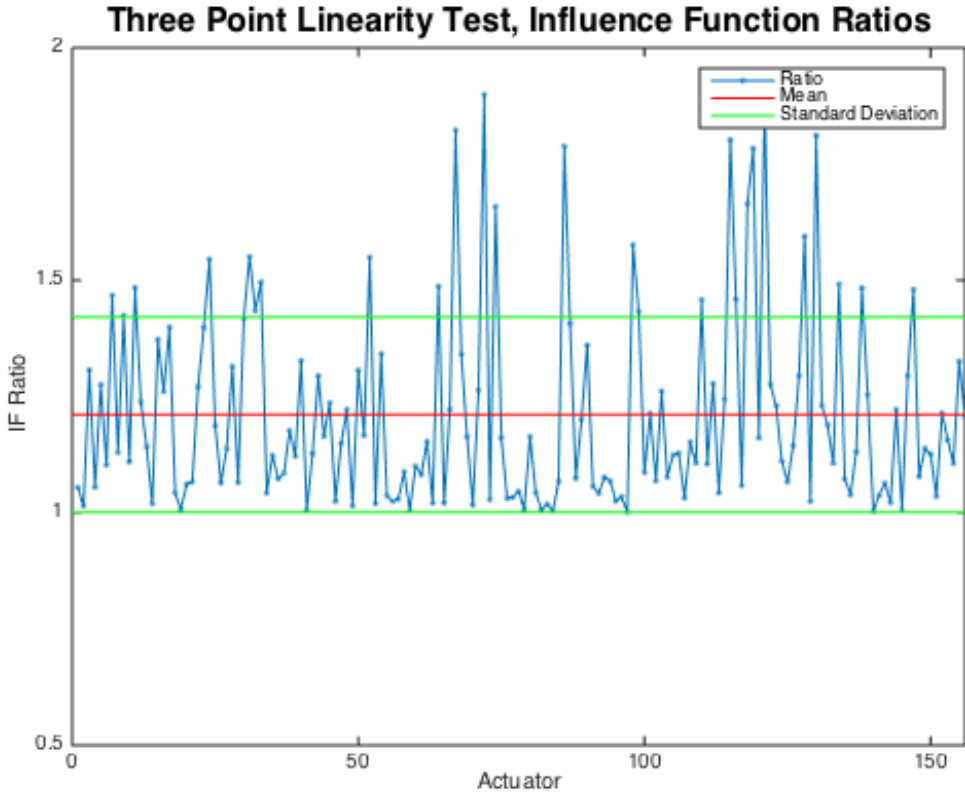
Figure 75. Three point linearity test

The experimentally derived influence functions average the positive and negative response. The linear model does not capture what actuators generate more mirror response in the positive direction or the negative direction. Therefore it is expected that the physical system behave differently than the linear model.

3.   Influence Function Comparison

Figure 76 shows influence functions of actuator 156 taken at varying voltages over the linear range of the actuators. The influence functions should be identical for a linear system. However, the normalized mirror responses are different when taken at different voltages from the bias. The influence function measured at +/-5V and +/-10V has a different global response than the influence functions measured at higher voltages. The influence functions measured at +/-25 and +/-30 volts are almost identical. The mirror center imperfections are also noticeable in for the influence functions taken at lower voltages. This could be due to the age of the SMT segments and changes in the

115

surface coatings, substrate properties, and the actuator epoxy.   The results show that the measured mirror surface response is not linear over the voltage range.   These results further support the use of feedback control to compensate for in accuracies in the linear model.
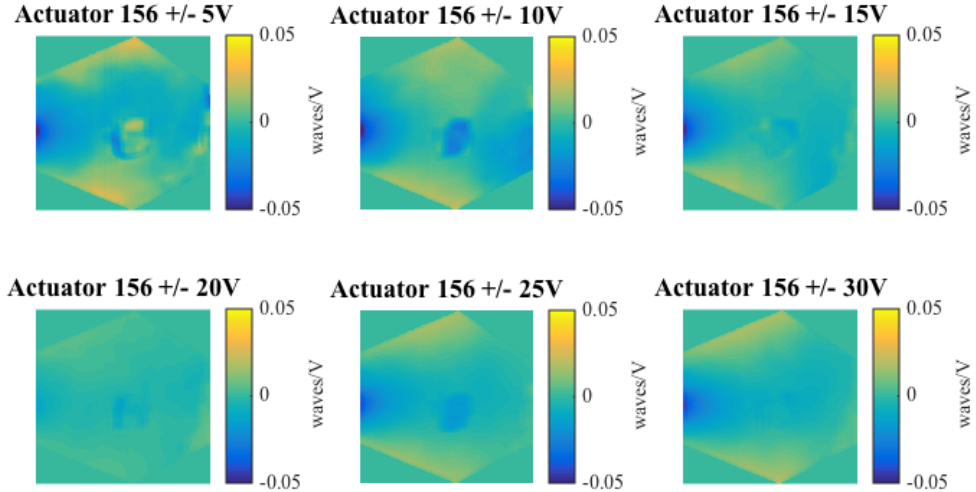

Figure 76. Influence function comparison for actuator 156

C.   SMT SEGMENT CONTROL EXPERIMENTAL RESULTS

This section presents experimental control results of a single SMT AHM segment using integral control, iterative constrained minimization control, and gradient control. These experimental results are used to compare the performance of the experimental woofer-tweeter results. The results below show the constrained minimization and gradient control approach outperforms the integral controller. The SMT segment was initialized to the biased position and the update gain for the integral control and iterative minimization was 0.2.

The SMT AHM closed loop experiments produced similar performance to the simulation. The constrained minimization control and gradient control outperform the integral control with the gradient controller improving the RMS wavefront error slightly more than the iterative constrained minimization, Figure 77. The final wavefront error of the constrained minimization control and the gradient control is similar because the

116

constrained minimization and gradient approach cost functions are both minimizing the quadratic wavefront error, but using different approaches and constraints.

The improved RMS wavefront error performance using the gradient controller is significant because the current AHM control techniques update the control signal by minimizing $\|\Gamma u - y\|^2$ with or without constraints. However, the gradient approach finds a local minimum through a steepest descent algorithm. Figure 78 compares the final control voltages of the three controllers and the gradient approach has the fewest actuators approaching the saturation limit (+/- 30 volts). Additionally the gradient approach has the lowest quadratic control cost, Figure 79.
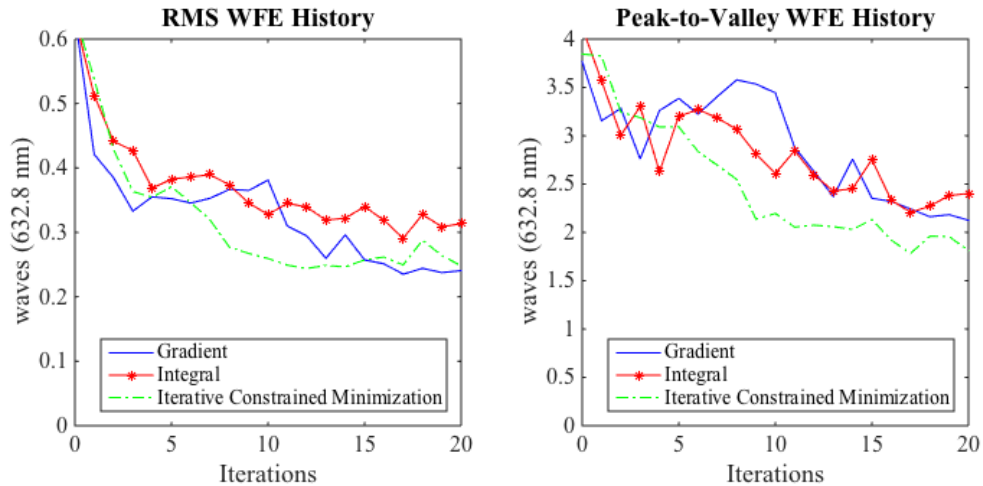

Figure 77. Experimental SMT segment error history using gradient control, integral control, and iterative constrained minimization
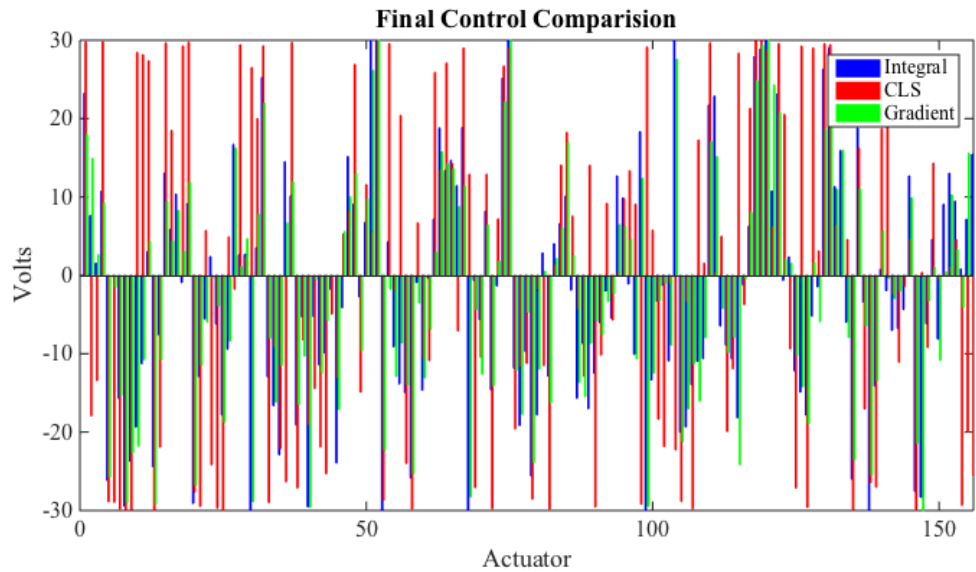
Figure 78. Final control comparison between SMT iterative constrained least squares and gradient control
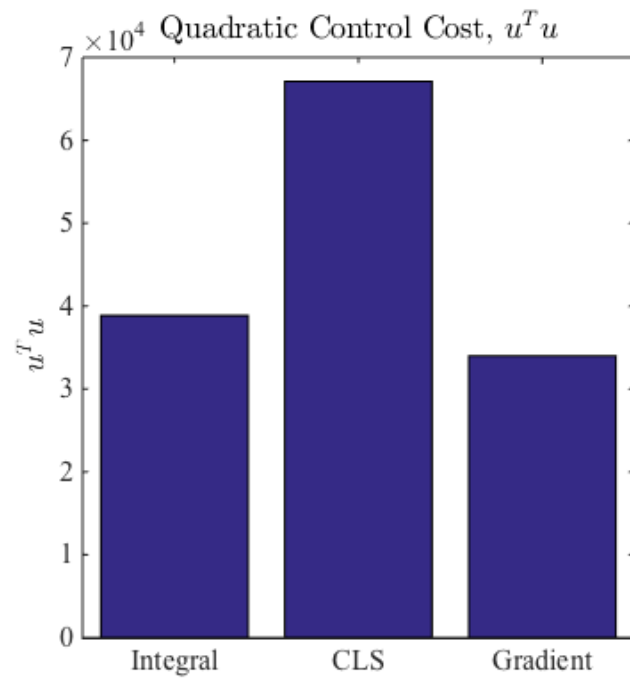

Figure 79. SMT AHM quadratic final control cost

D. EXPERIMENTAL FINE PHASING IMPROVEMENT

This section presents experimental results based on the fine phasing improvement approaches introduced in Chapter IV and simulated in Chapter V. This section first presents the experimental results from using the woofer-tweeter system with the closed loop woofer-tweeter control techniques recommended in Chapter V. Next the section presents the experimental results of the open loop woofer-tweeter optimal control techniques. Finally the experimental results comparing a controller using an updated influence matrix are compared to a controller using a standard influence matrix.

1. Woofer-Tweeter Closed-Loop Control

This section presents the experimental closed loop woofer-tweeter controller results. The results show that the global woofer-tweeter control approaches and the gradient control approaches outperform the traditional modal and offload woofer-tweeter control approaches for the experimental woofer-tweeter configuration. The experimental results also show the global woofer-tweeter controllers significantly improve wavefront error compared to a serial sequential woofer-tweeter constrained minimization controller. Figure 80 and Figure 81 summarize the steady state RMS and peak-to-valley wavefront error for the feedback control approaches respectively. Appendix B contains experimental error history plots showing the RMS and peak-to-valley wavefront error for the different controller experiments.

Setting the SMT segment 3 to the biased position initialized the woofer-tweeter experiments. The starting RMS wavefront error was approximately 0.57 waves. Similarly, setting the BMC deformable mirror to the pre-calibrated flat position initialized the experiment and resulted in 0.02 waves RMS of wavefront error over the SMT mask. To integral controller gain was set to 0.2 and number of iterations was set to 20. The experimental results are slightly different than the predicted results due to differences between the model and the experimental hardware performance.

119
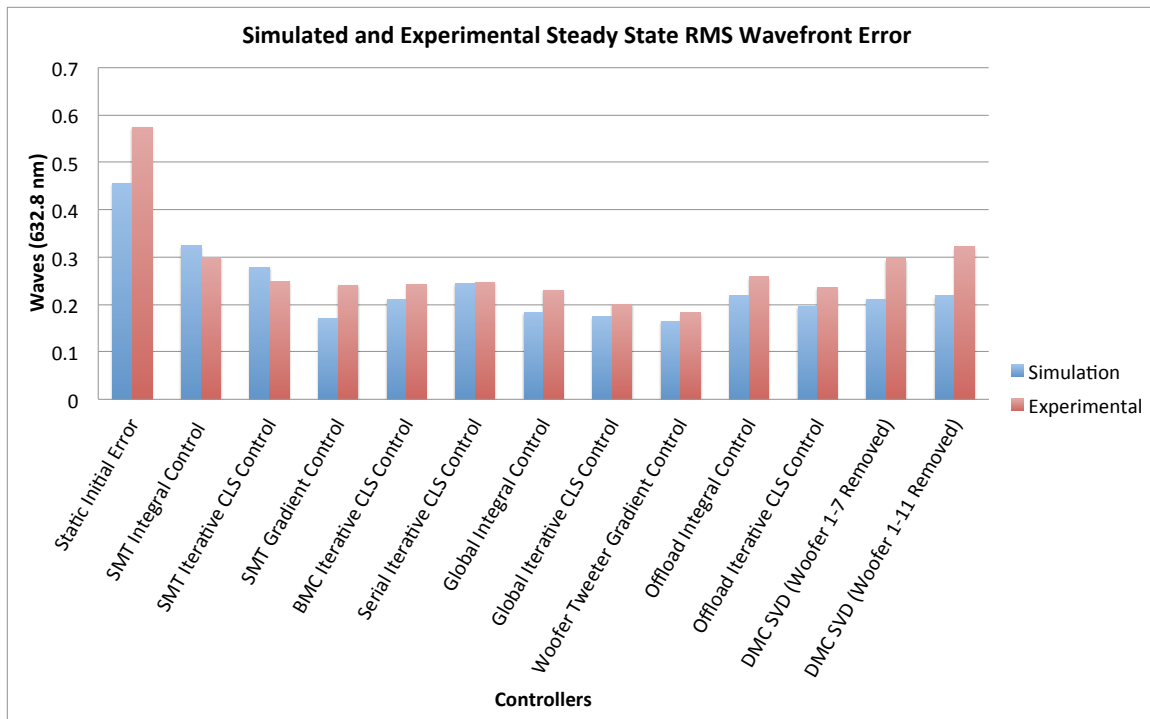
Figure 80. Simulated and experimental woofer-tweeter steady state feedback control RMS wavefront error comparison
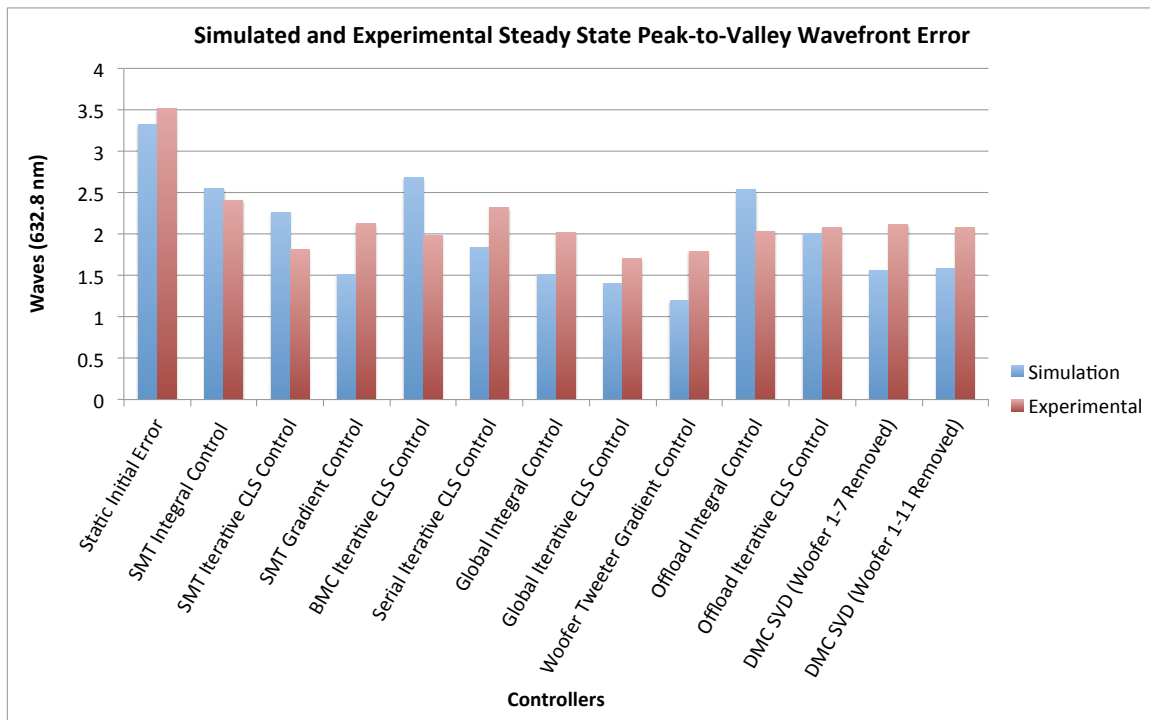

Figure 81. Simulated and experimental woofer-tweeter steady state feedback control peak-to-valley wavefront error comparison

The steady state woofer-tweeter experimental results are compared with the simulated results from Chapter V. The experimental results generally match the simulated results validating the models. This section presents the following closed loop woofer-tweeter control results; serial control, global control, offload control, and modal control.

a.   Serial Control

The woofer-tweeter serial controller closely matched the trend seen in simulation. The serial controller outperformed the SMT integral controller steady state RMS wavefront error. The serial control results were similar to the SMT iterative constrained minimization control and the gradient control results and like in simulation the tweeter only control slight produced a better RMS wavefront error result. This is due to the high spatial frequency residual error after applying the SMT AHM correction compared to the lower order errors that are present when the factory bias controls are applied. In this case the second deformable mirror is more effective at removing the residual error from the SMT AHM bias position than from the SMT AHM corrected position.

b.   Global Control

The global woofer-tweeter experimental RMS wavefront error results are similar to the simulated global controller results. The woofer-tweeter gradient control approach produced the best RMS wavefront error compared to the other woofer-tweeter controllers. Figure 82 compares the global control error histories. The woofer-tweeter gradient control showed a 24% RMS wavefront error improvement over the SMT segment gradient control results. As with the SMT AHM correction the global gradient approach outperformed the global iterative constraint based minimization approach. The total control cost was also slightly less using the gradient approach than using the global integral or iterative constraint minimization approach (see Figure 83).

The global gradient approach offers significantly improved performance over the integral controller. This is because the gradient control approach is more numerically stable and does not require the multiplying the feedback by the pseudo-inverse of the global influence matrix. The global gradient approach also weights the modal feedback

by the square of the influence matrix singular values placing emphasis on the modes that can be well corrected by the mirrors.

The global gradient approach showed similar performance to the constrained minimization control because the constrained minimization and gradient approach cost functions are both minimizing the quadratic wavefront error, but using different minimization approaches and constraints. The global gradient approach and constrained based minimization approach also converged in a similar number of iterations, however, the global gradient control approach was computationally faster because it did not require using a numerical optimization solver.
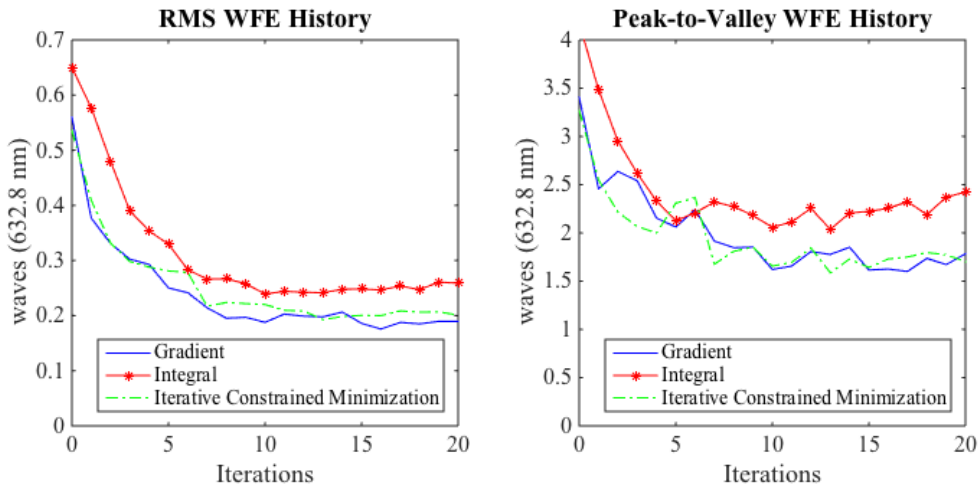

Figure 82. Experimental woofer-tweeter error history using gradient control, integral control, and iterative constrained minimization
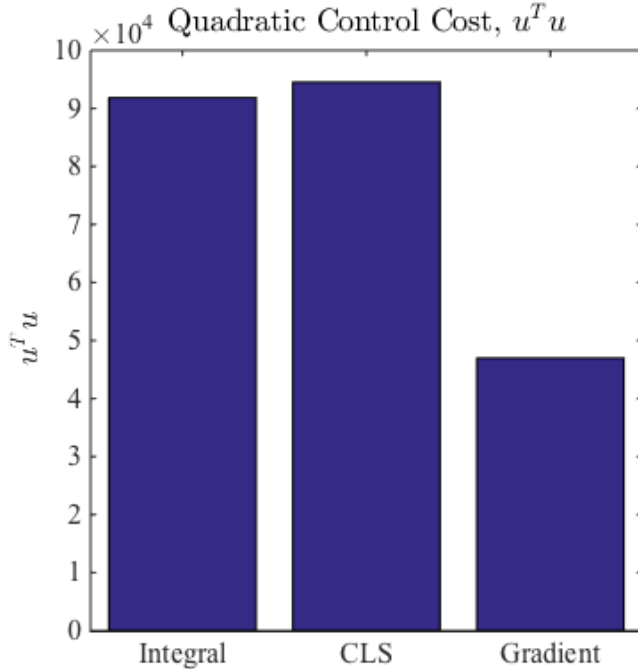
Figure 83. Woofer-tweeter quadratic final control cost

c.   *Offload Control*

The two offload controller experimental RMS wavefront error results were slightly worse than the global control results like with the simulated results.   The constrained minimization offload controller produced slightly better results than the integral controller as expected. The offload iterative constrained minimization controller did produce better RMS wavefront error results than the SMT segment control and the serial woofer-tweeter control. Although the results were not as good as the global control results in this experiment this technique is suitable. This approach would have produced better results if the woofer and tweeter shared more of the same SVD spatial modes. This control approach could work if the deformable mirrors used in the woofer-tweeter system were selected or designed to operate in an offload woofer-tweeter configuration.

d.   *Modal Control*

This section presents the woofer-tweeter distributed modal control results. Two experiments were conducted to match the simulated distributed modal control. The first experiment removed the first 7 woofer SVD modes from the tweeter and the second

experiment removed the first 11 woofer SVD modes from the tweeter. The experimental results did not show as much improvement as predicted by the simulation. Although the full capability of the woofer was used in the experiment a significant amount of capability to correct low order modes was removed from the tweeter. This is evident because the RMS wavefront error becomes worse as more woofer modes are de-projected from the tweeter. This control approach could work if the woofer and tweeter were designed and sized appropriately to complement their capabilities.

2. Woofer-Tweeter Open Loop Control

This section presents open loop control experimental results the woofer-tweeter system. Experimental results for the SMT AHM segment are included for comparison. Three open loop minimization approaches were tested using the cost functions from Chapter III repeated here in equation (6.3). Table 3 shows the weighting coefficients applied for the three experiments. Figure 84 and Figure 85 compare the simulated and experimental RMS and peak-to-valley wavefront error after applying open loop corrections.

$$\underset{u}{\operatorname{argmin}} J(u) = \frac{1}{2} \left(c_1 \left(\{\phi\}^T \{\phi\} \right) + c_2 \left(\max(\{\phi\}) - \min(\{\phi\}) \right) + c_3 \left(\{v_\Delta\}^T \{v_\Delta\} \right) + c_4 \left(\{u\}^T \{u\} \right) \right)$$
$$\text{subject to: } lb \leq \{u\} \leq ub \tag{6.3}$$

Table 3.   Cost function coefficients

	c1	c2	c3	c4
Cost Function 1	1	0	0	0
Cost Function 2	1	2	0	0
Cost Function 3	1	1	0	5.00E-04

The open loop minimization experimental results do not closely match the simulated results. This is due to the fact that the linear influence matrix model response varies from the physical hardware response. However, the open loop control does show improvement in RMS and peak-to-valley wavefront error from the starting wavefront error.

The different weighting coefficient results generally match the predicted results. For example, the experimental results show that adding a penalty to peak-to-valley wavefront error was able to slightly improve the peak-to-valley wavefront error. The results also show that penalizing the control increases the RMS and peak-to-valley wavefront error because less control authority is available. These experimental results shows that the SMT AHM and woofer-tweeter system perform better using a closed loop feedback control system.

Open Loop Minimization Control RMS Wavefront Error
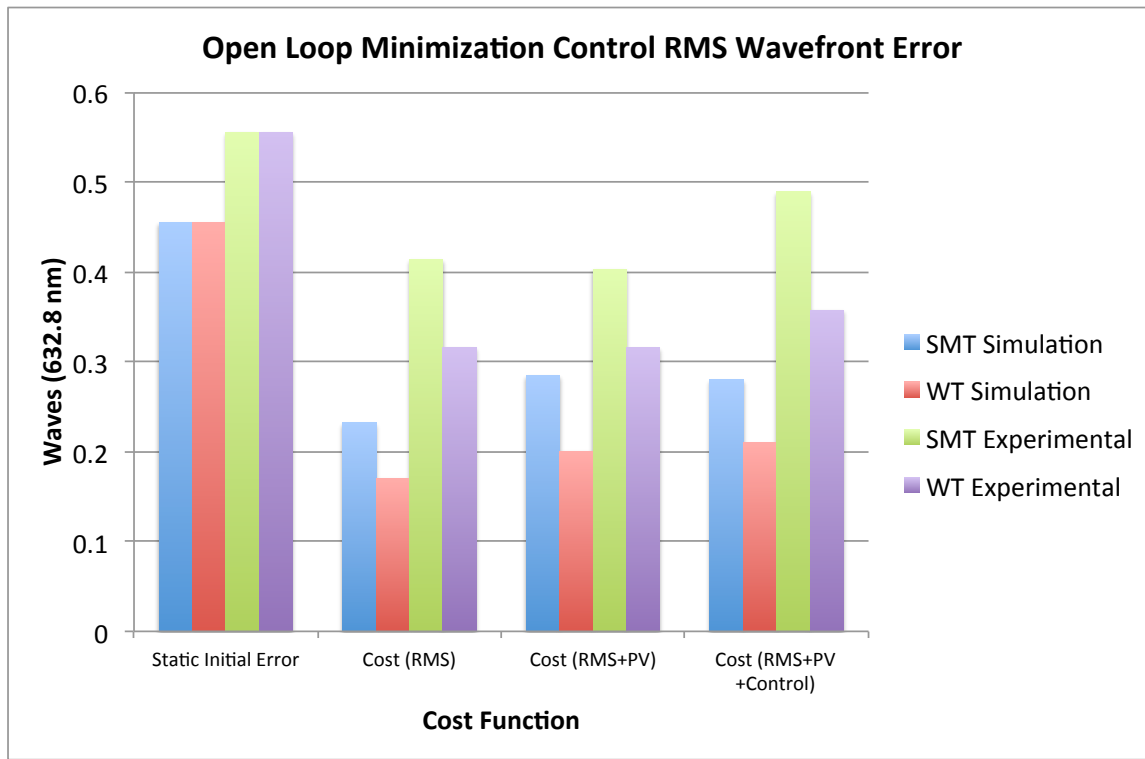
Figure 84. Comparison between open loop simulated and experimental control, RMS wavefront error
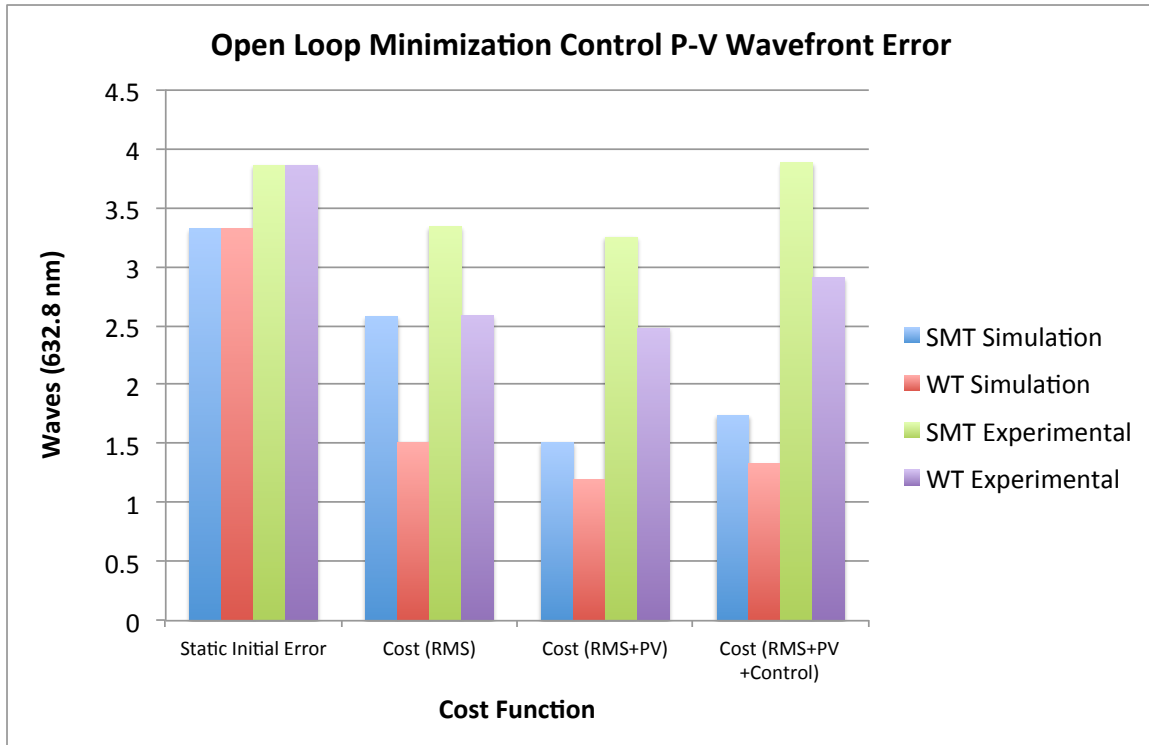
Figure 85. Comparison between open loop simulated and experimental control, peak-to-valley wavefront error

3.   Adaptive Influence Matrix

The adaptive influence matrix experimental results are presented in this section. The results show a small improvement in RMS and peak-to-valley wavefront error by applying an update to the influence matrix prior to using the influence matrix in feedback control.   Two experiments are presented using two different experimentally derived influence matrices. The first experiment uses an influence matrix with influence functions collected at +/-15V.   The second experiment uses an influence matrix with influence functions collected at +/-30V.

The adaptive influence matrix is tested using the SMT AHM segment. The influence matrix is updated using the approach described in Chapter IV.   After the influence matrix is update it is used with an integral feedback controller to correct the SMT AHM surface.   The error history results are compared to an integral feedback controller without the influence matrix update.

126

Figure 86 and Figure 87 show the experimental results for the two experiments. Both experiments show the influence matrix update slight improves the RMS and peak-to-valley wavefront error. The results also show the variation in performance based on the influence matrix. The +/-15V influence matrix does not produce results as good as the +/-30V influence matrix. An adaptive influence function may prove useful to update the influence function to better represent the physical system.
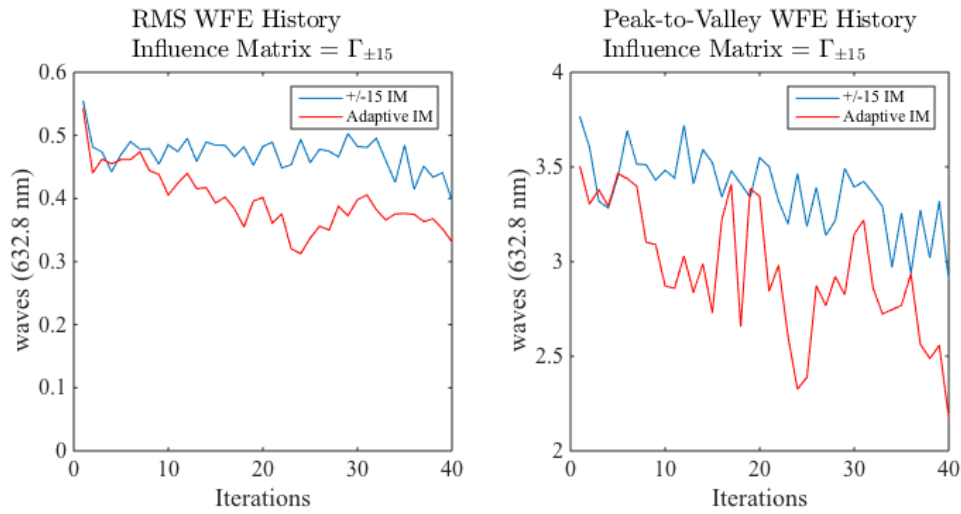

Figure 86. SMT AHM wavefront error history with and without influence matrix update using integral control, +/-15V influence matrix
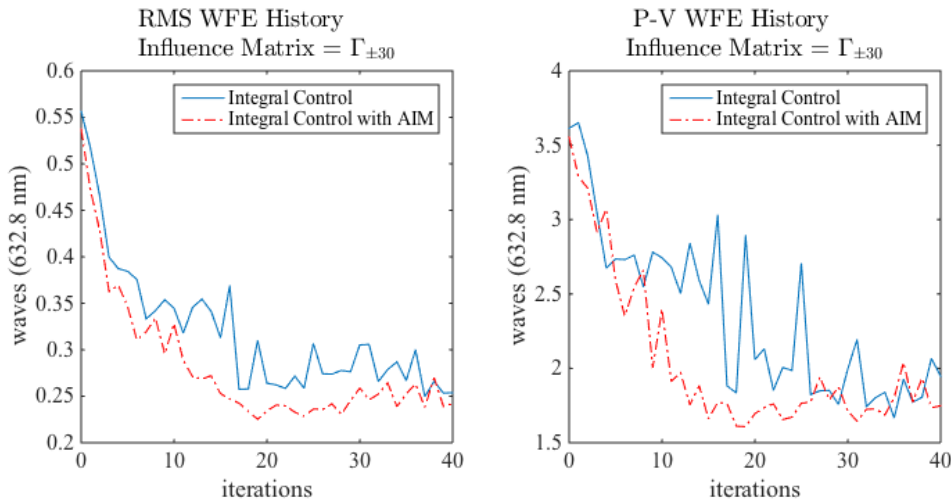
Figure 87. SMT AHM wavefront error history with and without influence matrix update using integral control, +/- 30V influence matrix

E.   CONCLUSIONS

The experimental results validated the woofer-tweeter models from Chapter III and Chapter IV. The results showed that a space telescope woofer-tweeter system is viable and can improve the wavefront error attributed to the primary mirror segment. The experimental woofer-tweeter performance was limited by the size of the additional deformable mirror and available actuators, however a 24% RMS wavefront error and 16% peak to valley wavefront error improvement was shown using the woofer-tweeter gradient controller. The woofer-tweeter global integral controller and global iterative constrained minimization controller also showed wavefront improvement compared to the SMT segment constrained minimization controller. Updating the SMT segment influence matrix using the adaptive influence matrix technique also showed wavefront error improvement.

VII. SUMMARY, CONTRIBUTIONS, AND FUTURE WORK

This chapter presents a final summary of the work presented in this dissertation. The significant contributions of this research are summarized. Recommendations for future research are also described.

A. SUMMARY OF WORK

The goal of this dissertation was to develop woofer-tweeter control techniques for use in a space telescope. In order to do this, a space telescope woofer-tweeter model was developed to simulate woofer-tweeter control techniques. The woofer-tweeter model was based on the Naval Postgraduate School's 3-meter SMT. This required an understanding the SMT woofer-tweeter design assumptions and an understanding of the SMT design. The result was a woofer-tweeter design that placed a deformable mirror at the SMT exit pupil.

Two analytical models were developed based on woofer-tweeter design. The first analytical model included a dynamic model of the SMT with a static influence matrix model for the additional deformable mirror. The second model included a quasi-static SMT model with a static influence matrix deformable mirror model. The quasi-static woofer-tweeter model was reduced to represent a single SMT segment in order to match the experimental setup. The models were updated to include the measured primary mirror residual surface error. The measured surface error produced simulated results representative of the physical system.

The SMT wavefront control was simulated beginning from segment stacking through fine phasing with the SMT AHM residual error as an initial condition. The simulated results showed that the current SMT system could not meet the fine phasing requirements due to the residual primary mirror surface error. Two problems were identified. First, the Shack-Hartmann wavefront sensor did not have enough spatial resolution to measure the high frequency wavefront error. Second, the residual surface error of the AHM segment was outside the capture range of the phase retrieval algorithm.

These results supported the use of an additional deformable mirror to improve the residual wavefront error.

Fine phasing improvement approaches were presented including closed loop woofer-tweeter control and open loop woofer-tweeter control. The simulated and experimental research showed that the closed loop control approaches outperformed the open loop control approaches because the woofer-tweeter influence matrix models varied from the physical hardware. The global woofer-tweeter control techniques reduced the residual wavefront error more than the serial, modal, and offload control techniques. The woofer-tweeter gradient controller produced the best results experimentally reducing the RMS wavefront error by 24% compared to the best SMT AHM corrected wavefront error.

Another fine phasing improvement presented was the SMT influence matrix model update. The SMT AHM influence matrix was iteratively updated using the gradient of a cost function that compared the difference between the predicted mirror response and the measured mirror response. Simulation and experimental results showed the influence matrix update technique could slightly improve the performance of the SMT AHM. This technique may be advantageous updating the influence matrix without recollecting influence functions saving precious collection time.

Existing closed loop woofer-tweeter control techniques were presented and a woofer-tweeter gradient control technique was introduced. Open loop woofer-tweeter control techniques were also introduced. Finally an adaptive influence matrix technique was presented as a means to improve fine phasing residual wavefront error by improving the SMT AHM segment model.

The simulated and experimental research presented in this dissertation showed that a space telescope woofer-tweeter system is feasible and can improve the wavefront error attributed to the primary mirror segment. Woofer-tweeter space telescope control techniques were presented and experimentally validated showing significant improvement in residual wavefront error.

B. CONTRIBUTIONS

Adaptive optics have been proposed in the past to compensate for space telescope primary mirrors. However, the current state of the art has not addressed wavefront control techniques for a woofer-tweeter space telescope configuration. The contributions of this research are as follows:

1. Woofer-Tweeter Space Telescope Modeling and Simulation

A woofer-tweeter space telescope model was developed for the SMT test bed. This model built upon the SMT state space model but was updated to include an additional deformable mirror, experimentally derived influence matrices, actuator models, sensor models, full state observer, and residual errors associated with the active primary segments. These updates enabled more realistic results during simulation.

The SMT incremental wavefront sensing and control system was also simulated for the first time from deployment through fine phasing using the measured SMT AHM surface figure error data. The coarse alignment and coarse phasing steps were successfully controlled using LQG state feedback controllers. The fine phasing step was accomplished using a quasi-static adaptive optic integral control technique. This simulation showed that the current SMT Shack-Hartmann wavefront sensor lacked the necessary spatial resolution to successfully correct the SMT AHM residual error. The simulation also showed that the SMT AHM residual error was outside the capture range of phase diversity phase retrieval algorithms.

The model was reduced to a single segment quasi-static model to represent the SMT woofer-tweeter experimental test bed and was experimentally validated using the SMT test bed. The model was used to simulate fine phasing control techniques and evaluate performance prior to testing the controllers on the test bed.

2. Woofer-Tweeter Space Telescope Control Techniques

Existing closed loop woofer-tweeter control techniques were applied to a space telescope application. The techniques were simulated and experimentally test and performance was evaluated. A new woofer-tweeter gradient control technique was

developed using SVD modal feedback. The gradient controller includes singular value weighting that automatically weights the modal coefficient feedback and is specific to the deformable mirror capabilities. The result showed the gradient controller outperformed the other woofer-tweeter controllers in simulation and experimental tests. The SVD modal gradient controller was also applied to the SMT AHM mirror and showed improved performance over the integral feedback control and iterative constrained minimization.

3. Woofer-tweeter Space Telescope Experimental Results

This research showed that a space telescope woofer-tweeter system is feasible and can improve the wavefront error attributed to the primary mirror segment. The experiments were conducted using large aperture active mirrors designed for space applications. The errors present in the experimental system were representative of current large aperture lightweight optics. The research showed that even with an undersized additional deformable mirror an improvement of 24% RMS wavefront error was achieved.

4. Experimental Characterization of Actuated Hybrid Mirror

A SMT actuated hybrid mirror was experimentally characterized. The experimental results showed a non-linear response of the SMT segment over the varying face sheet actuator range. Both the actuator response and face sheet response were shown to vary from the linear model. This information provides better understanding of the behavior of these mirrors and can be used to develop new control strategies to improve the performance of the mirrors.

5. Adaptive Influence Matrix Update

An adaptive influence matrix update technique was developed in order to improve the performance of the SMT AHM influence matrix. Experimental results showed that using the updated influence matrix with an integral controller improved the RMS wavefront error compared to a controller with a static influence matrix. This technique may be advantageous for updating a telescopes active primary mirror influence matrix on

orbit, as it does not require the collection of influence functions for each actuator saving valuable collection time.

C.   RECOMMENDATIONS

This dissertation showed the feasibly of using an additional deformable mirror with a large active primary mirror to improve the residual wavefront error.   However the simulated and experimental results were based on the performance of existing mirror capabilities. The woofer-tweeter fine surface control approach can work better if it is considered from the beginning of the design phase. This would allow the woofer and tweeter performance to be properly traded to determine the individual mirror surface requirements and correction capabilities.

Future woofer-tweeter experimental work should include testing a properly sized woofer-tweeter space telescope system.   This could include the replacement of the existing deformable mirror with a deformable mirror with a higher actuator count. Simulations in this research showed a minimum of 543 actuators were need to reduce the SMT AHM segment residual wavefront error of $\lambda/15$ waves RMS. Another option would be to demonstrate a woofer-tweeter system with a newer large AHM with less residual surface error.

Another recommendation is to update the SMT test bed to include a deformable mirror in the rear optics. This could add confidence to the woofer-tweeter approach, by demonstrating a more realistic implementation. There are challenges with including the deformable mirror in the optical path including field steering, field angle magnification, and the optical design. The SMT Shack-Hartmann wavefront sensor would also need to be upgraded to improve spatial resolution.

THIS PAGE INTENTIONALLY LEFT BLANK

APPENDIX A. SIMULATION RESULTS

This appendix includes the error history and wavefront surface plots for both the feedback control techniques and open loop control techniques simulated in Chapter V.

A.   SMT AHM SEGMENT SIMULATED RESULTS

The SMT AHM segment was simulated using the 156 FSAs to compare the results to the woofer-tweeter configuration. The simulations included zero mean Gaussian plant and sensor noise.

1.   SMT Segment 3 Static Error
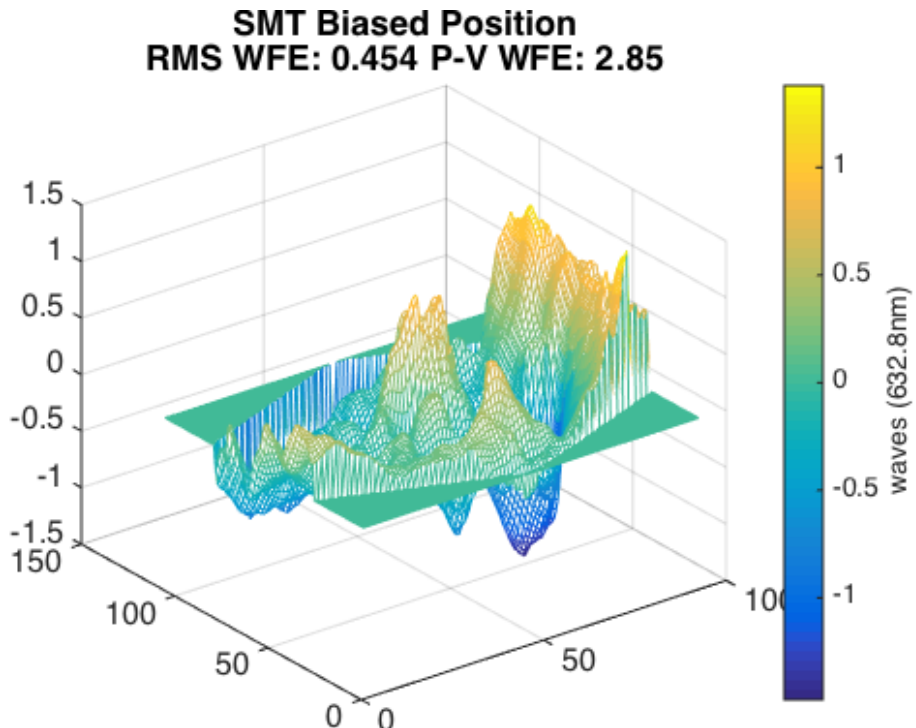
Figure 88. SMT Segment 3 biased position

## 2.	SMT Integral Control

SMT Segment Integral Control
RMS WFE History

SMT Segment Integral Control
P-V WFE History
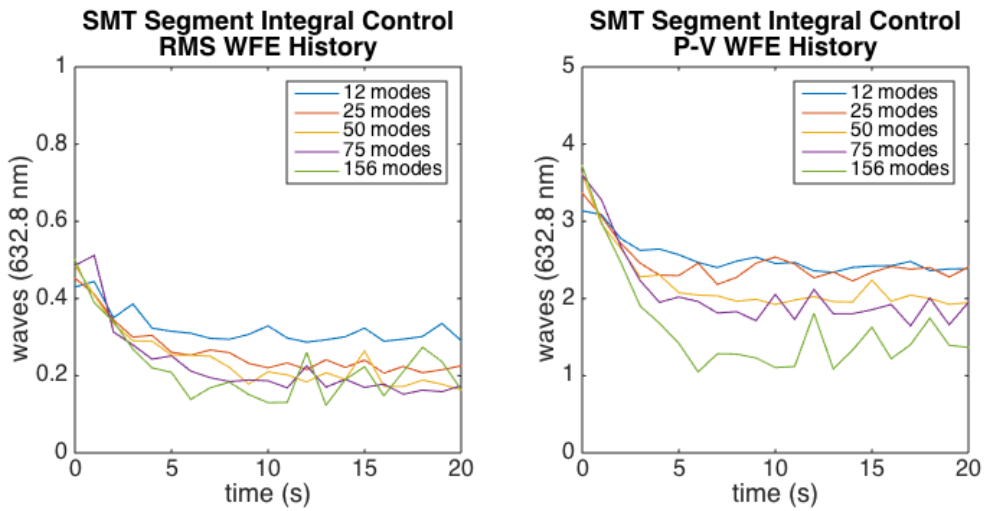
Figure 89. SMT integral modal control for different modal feedback

SMT Integral Control
RMS WFE = 0.324, P-V WFE = 2.55
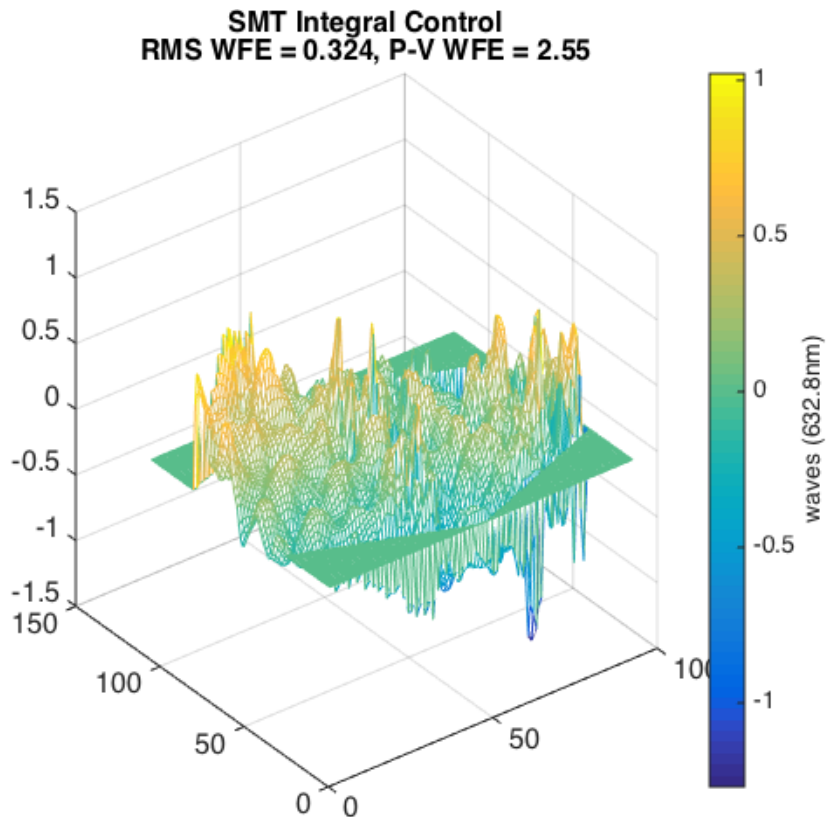
Figure 90. SMT segment integral control surface error

3. SMT Constrained Minimization Control
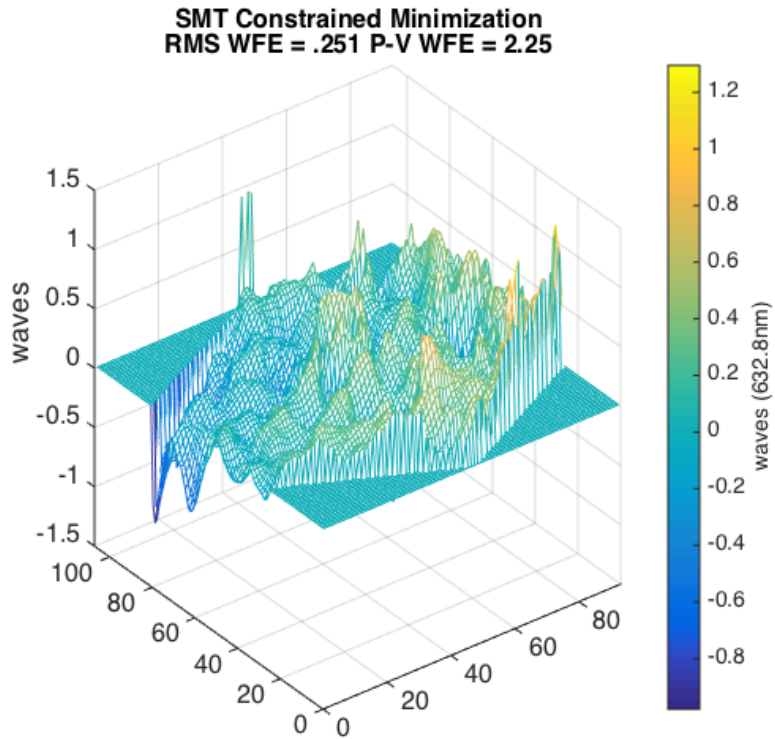
Figure 91. SMT constrained least squares control residual surface error

4. SMT Gradient Control

This simulation only adds zero mean Gaussian noise with a standard deviation of 0.5 volts to the mirror input. To represent the DM fitting capability of the SMT AHM segment we feedback the first 12 SVD modes.
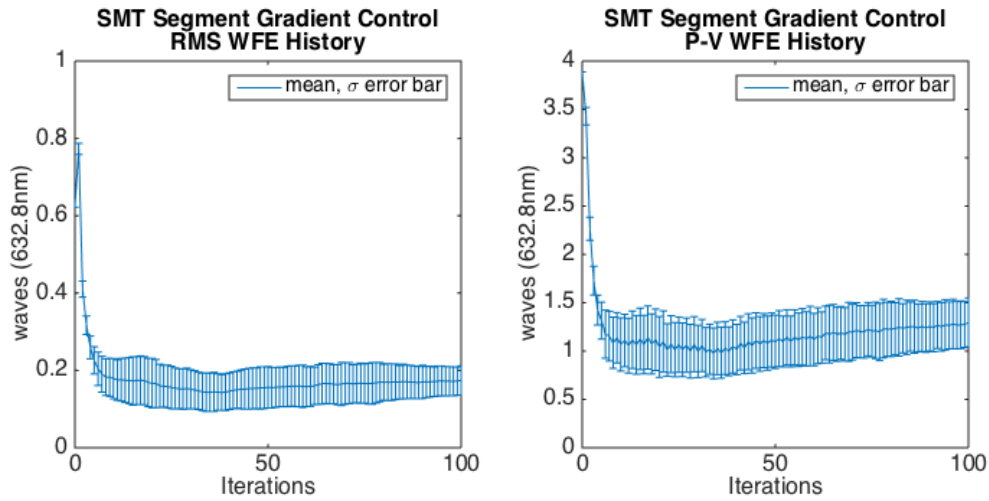
Figure 92. SMT AHM segment gradient control wavefront error history
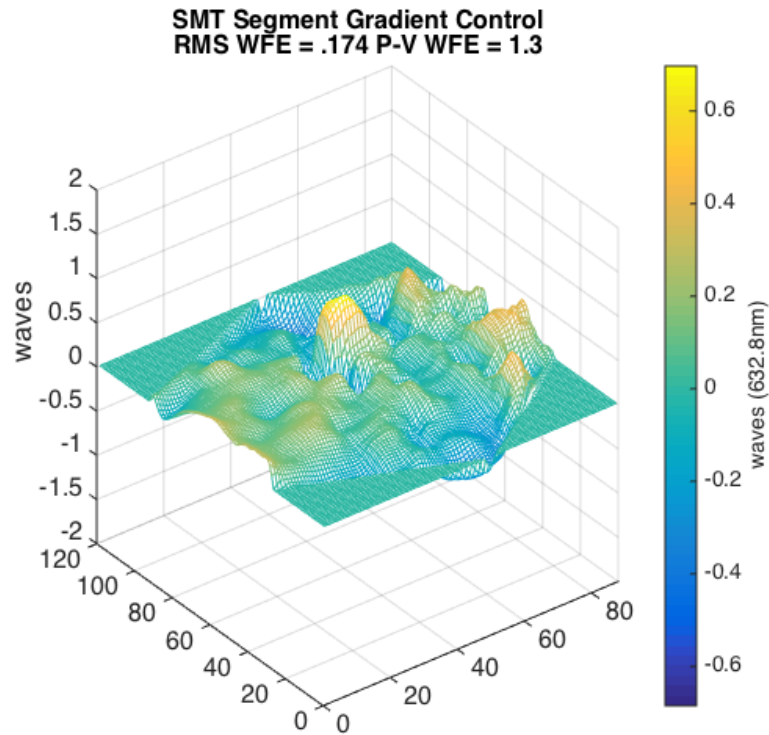
Figure 93. SMT AHM gradient control residual surface error

5.   Tweeter Control

The tweeter only simulation applies a correction to the static SMT segment wavefront using the BMC-140 deformable mirror. The process noise is zero mean

Gaussian white noise with a standard deviation of 0.25 volts. The noise is only applied to the tweeter mirror. The simulation uses an iterative constrained least squares controller with an update gain of 0.2 and an actuator saturation limit of +/- 80% of the mirror's biased maximum voltage.
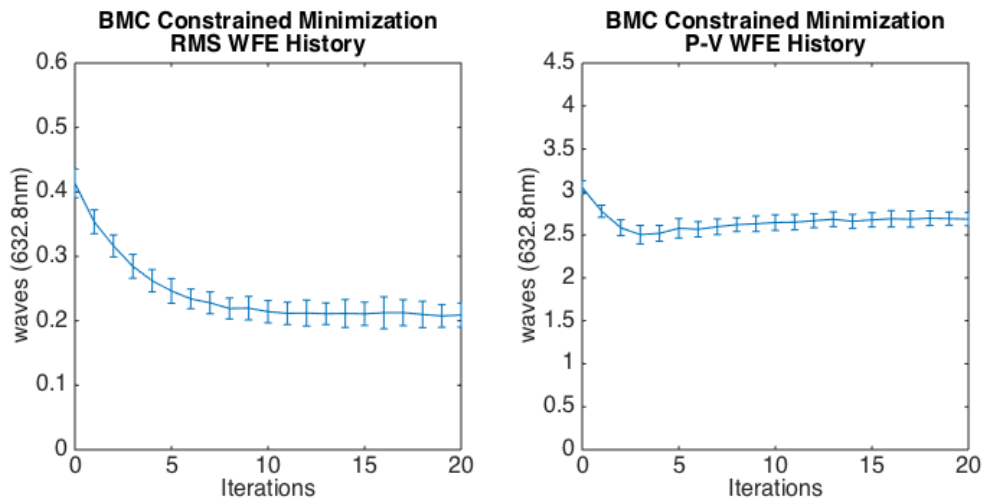
Figure 94. Tweeter iterative constrained minimization wavefront error history
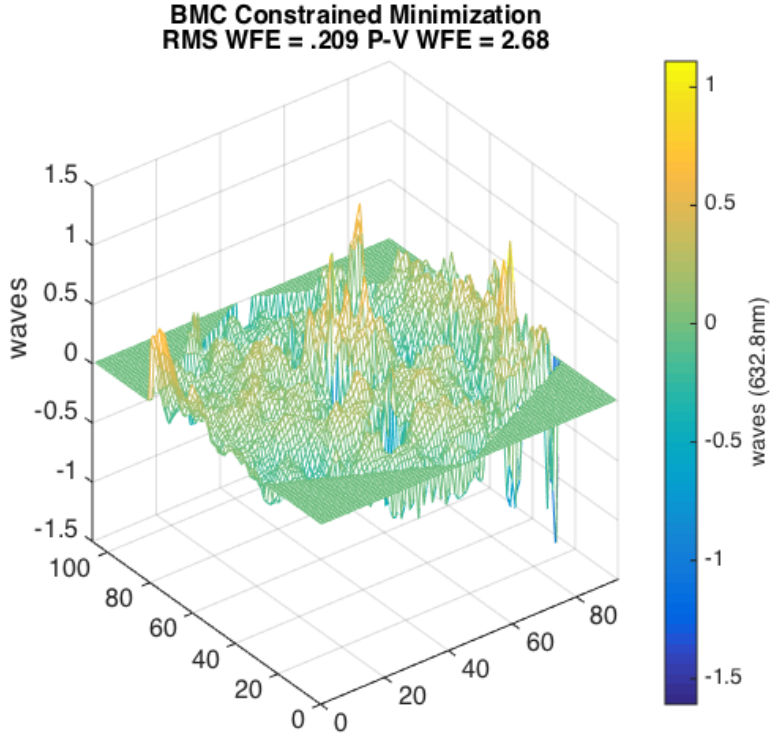
Figure 95. Tweeter iterative constrained minimization control residual surface error

B. WOOFER-TWEETER CLOSED-LOOP SIMULATED RESULTS

This section includes the woofer-tweeter simulated results. The woofer in this case is the SMT AHM segment and the tweeter is the BMC deformable mirror with 61 active channels.

1. Serial Constrained Minimization Control

The simulation runs 100 times and the mean RMS and peak-to-valley wavefront error are plotted. The two-step correction uses an iterative constrained least squares routine to minimize the wavefront. First the SMT AHM segment applied correction, and then the 61 actuators of BMC-140 deformable mirror applied correction. An update gain of 0.2 is used for both controllers and the saturation limit is set to +/- 30 volts for the SMT and the BMC deformable mirror where the BMC deformable mirror inputs are normalized to match the SMT input voltages. Process noise is zero mean Gaussian with a standard deviation of 0.5 volts on the SMT AHM and 0.25 volts on the BMC-140 input.

140
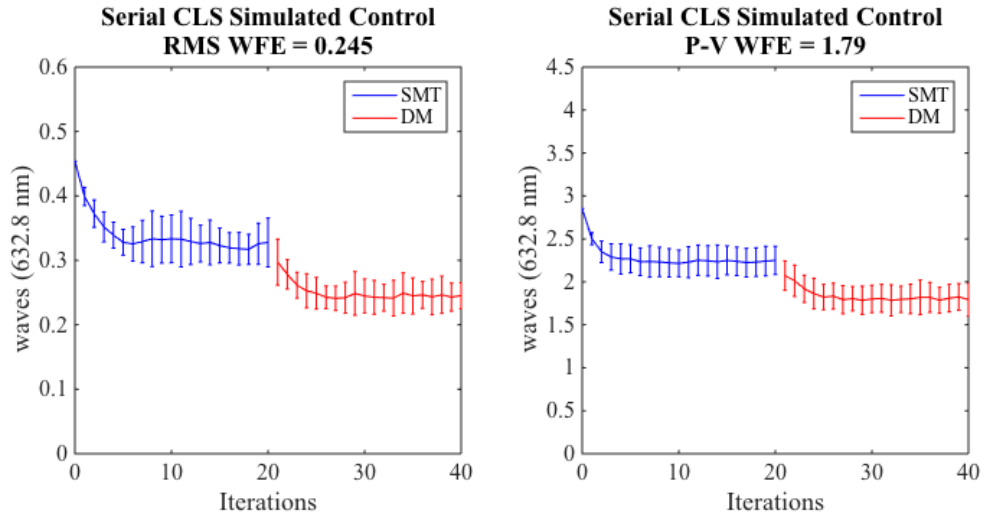
Figure 96. Serial iterative constrained least squares woofer-tweeter controller
wavefront error history
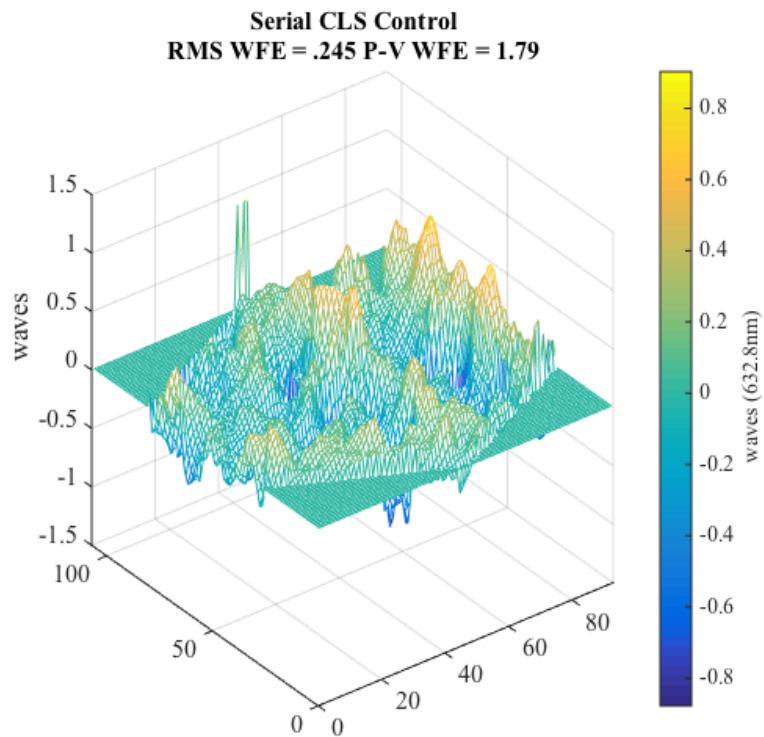
Figure 97. Serial iterative constrained least squares controller residual surface
error

2.   Global Control

The global integral control simulations run 100 times. Results are shown for integral control, iterative constrained minimization control and gradient control. The figures in this section show the mean RMS and peak-to-valley wavefront error. The error bars show the standard deviation. The process noise is zero mean Gaussian white noise with a standard deviation of 0.5 volts.

a.   *Global Integral Control*
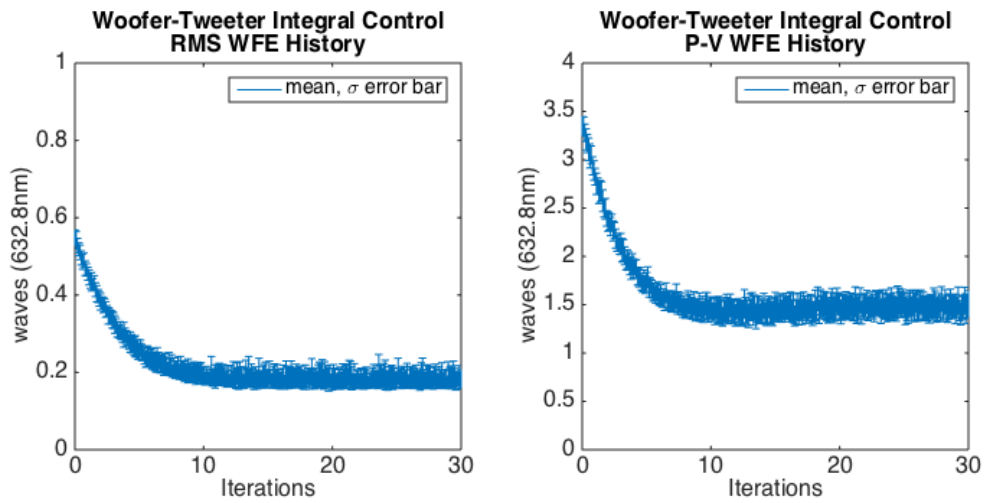
Figure 98. Woofer-tweeter integral control wavefront error history
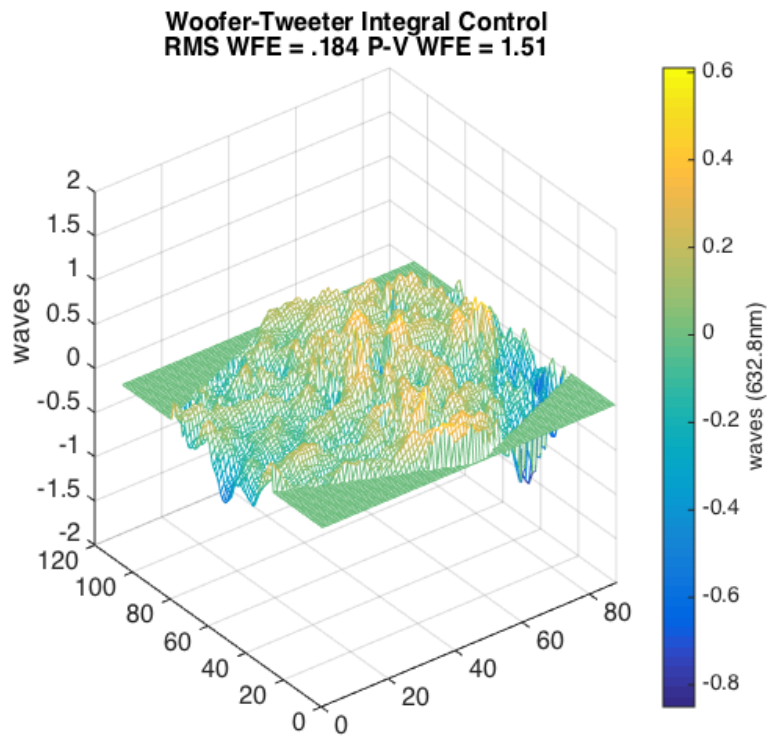
Figure 99. Woofer-tweeter integral control residual surface error

b.   *Global Iterative Constrained Minimization Control*
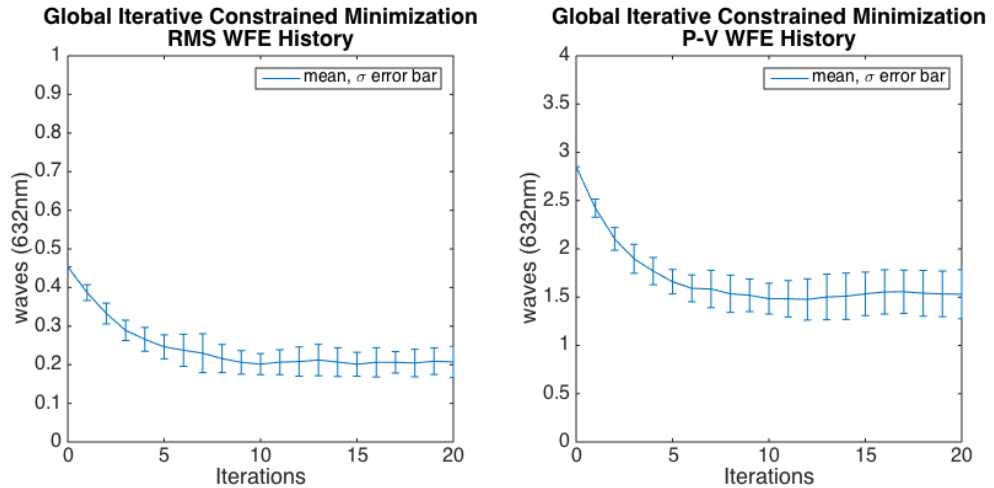

Figure 100. Woofer-tweeter global iterative minimization control wavefront error history

Global Iterative Constrained Minimization
RMS WFE = 0.174, P-V WFE = 1.4
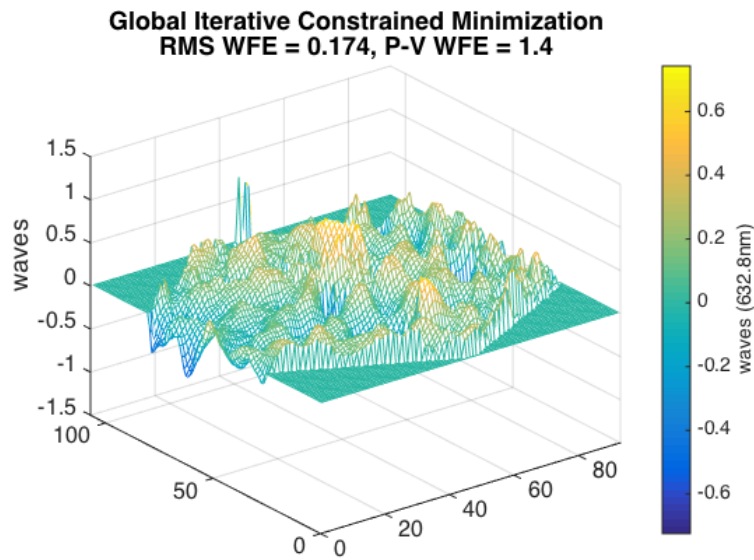
Figure 101. Woofer-tweeter global iterative minimization control residual surface error

c.   *Global Gradient Control*

The first 100 SVD modes are used as feedback.
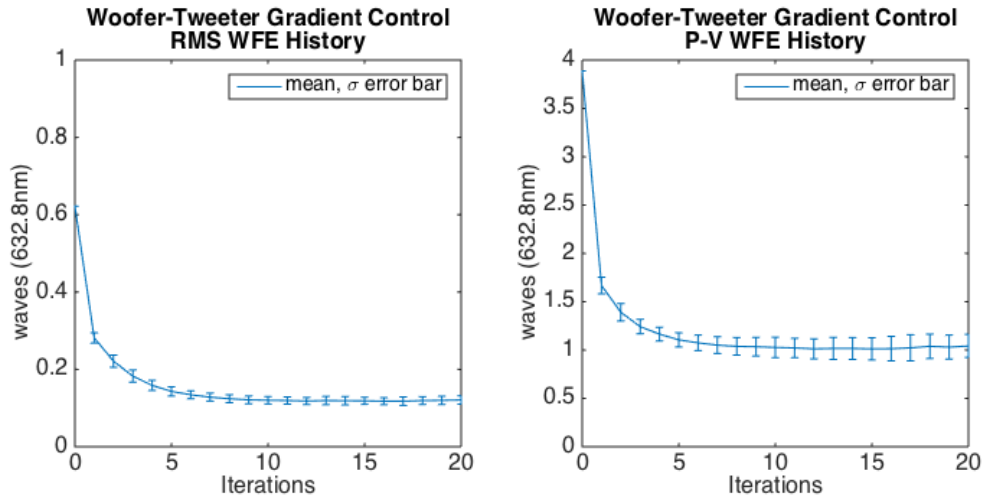
Figure 102. Woofer-tweeter gradient control wavefront error history
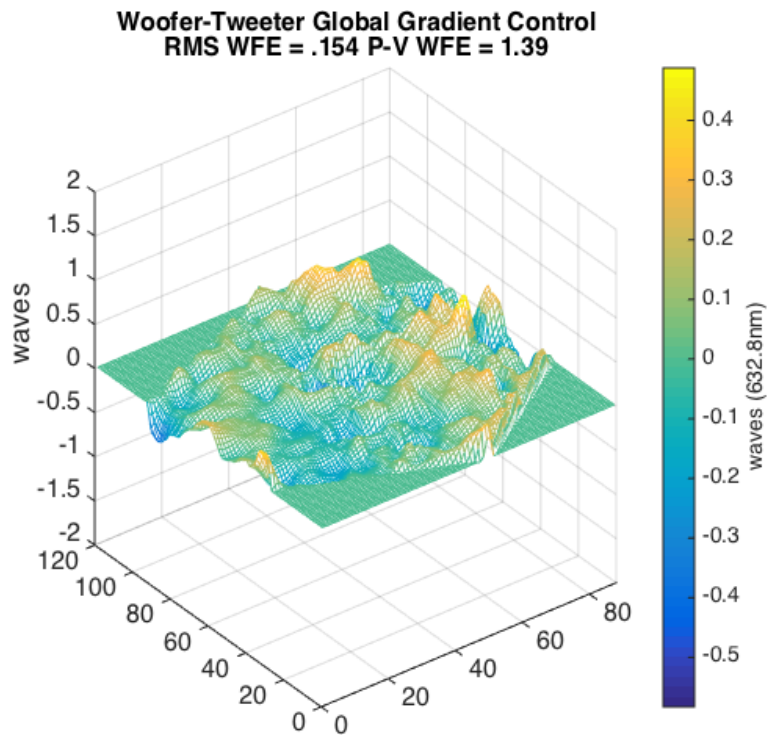
Figure 103. Woofer-tweeter gradient control residual surface error

3. Offload Control

The offload control approach is simulated using an integral controller and a constrained minimization controller. The control simulation runs 100 times. The figures show the mean RMS and peak-to-valley wavefront error. The error bars show the standard deviation. The process noise is zero mean Gaussian white noise with a standard deviation of 0.5 volts.

a. *Offload Integral Control*
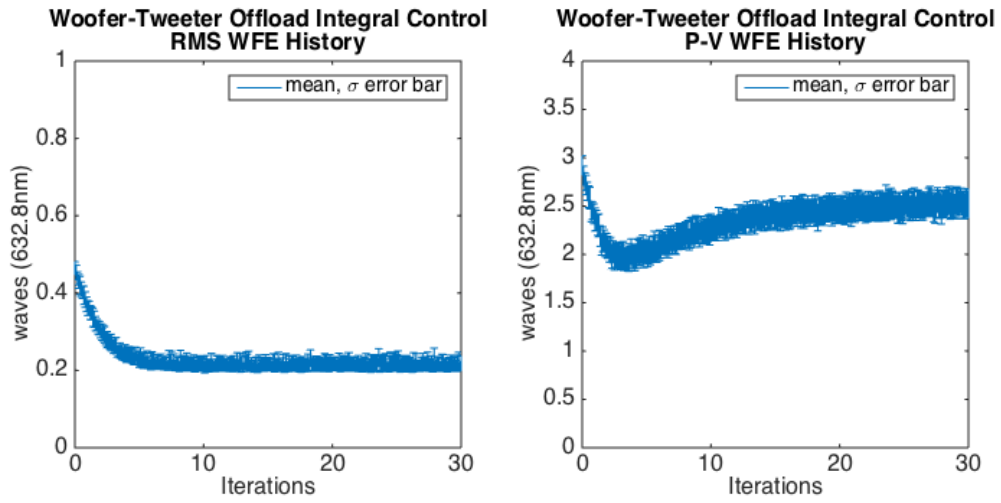
Figure 104. Woofer-tweeter offload integral control wavefront error history
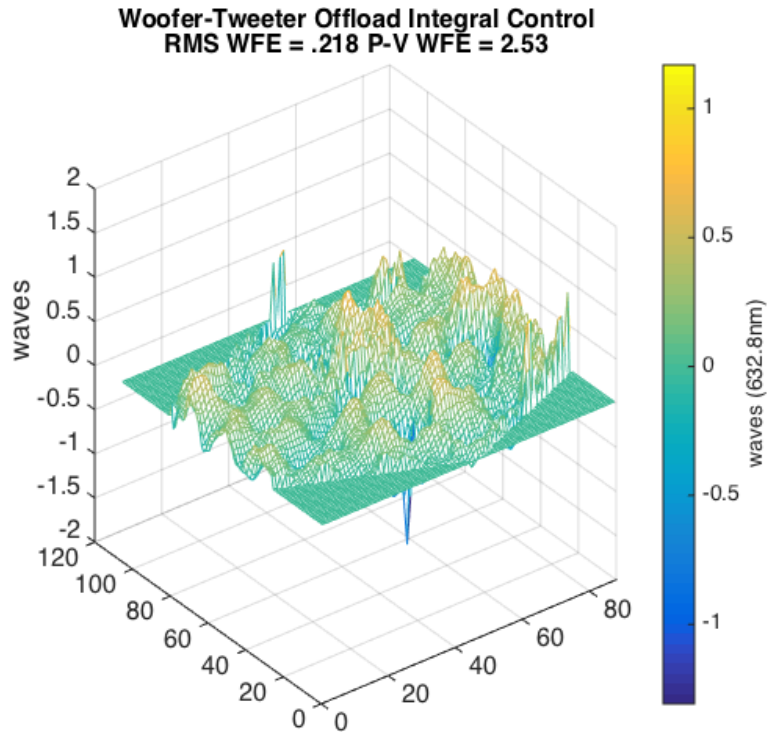
Figure 105. Woofer-tweeter offload integral control residual surface error

146

b. *Offload Iterative Constrained Minimization Control*
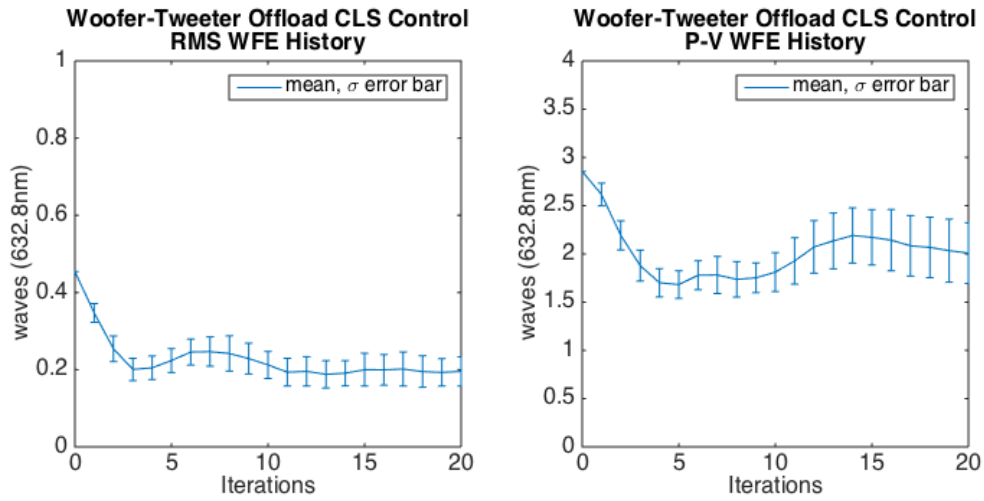
Figure 106. Woofer-tweeter offload iterative constrained least squares wavefront error history
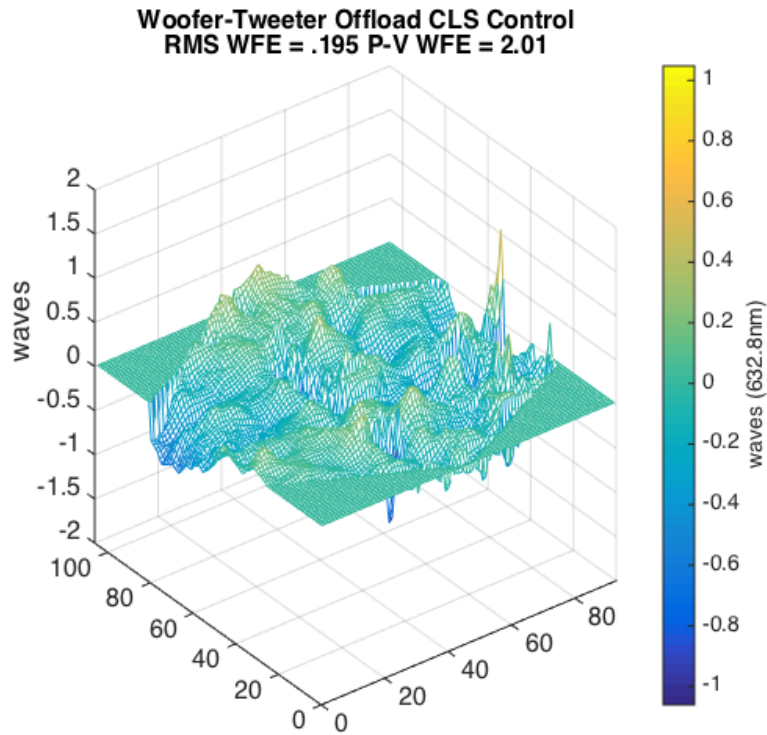

Figure 107. Woofer-tweeter offload constrained least squares residual surface error

147

4. Modal Control

This section presents simulated results for two modal controllers. The first is the modal coefficient controller and the second is the distributed modal controller. The control simulations run 100 times. The distributed modal control simulation is run for three separate scenarios described in this section. The figures show the mean RMS and peak-to-valley wavefront error. The error bars show the standard deviation. The process noise is zero mean Gaussian white noise with a standard deviation of 0.5 volts.

a. Modal Coefficient Control

This modal coefficient controller uses Zernike coefficients as the common basis for the two SMT segment and deformable mirror. The woofer is assigned the first 7 modes while the tweeter is assigned the Zernike modes 8-24. The residual wavefront includes the high order modes above 24 as well as the deformable mirror fitting error. The fitting error is the error associated with the mirror not reproducing the Zernike mode exactly.
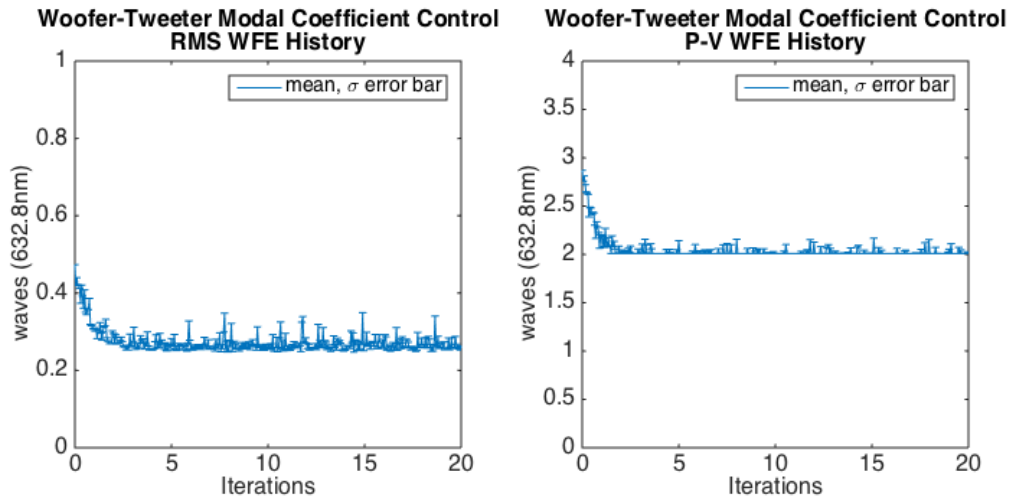

Figure 108. Woofer-tweeter modal coefficient control wavefront error history
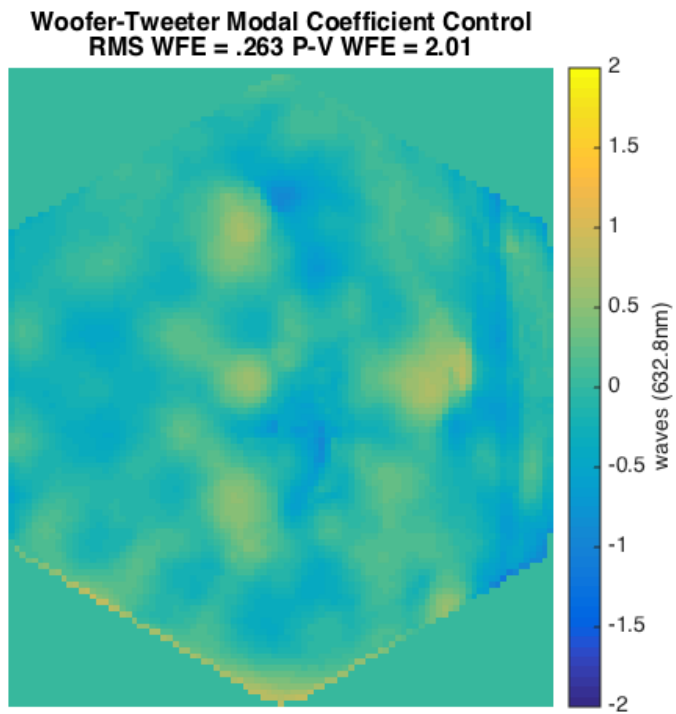
Figure 109. Woofer-tweeter modal coefficient control residual surface error

b.   *Distributed Modal Control*

Distributed modal control simulations are run for three scenarios.   The first scenario completely removes the influence of the woofer from the tweeter.   The second scenario removes the first 7 modes of the woofer from the tweeter, and the third scenario removes the first 11 modes of the woofer from the tweeter.   The figures in this section show the steady state surface error and the RMS and peak-to-valley wavefront error history.
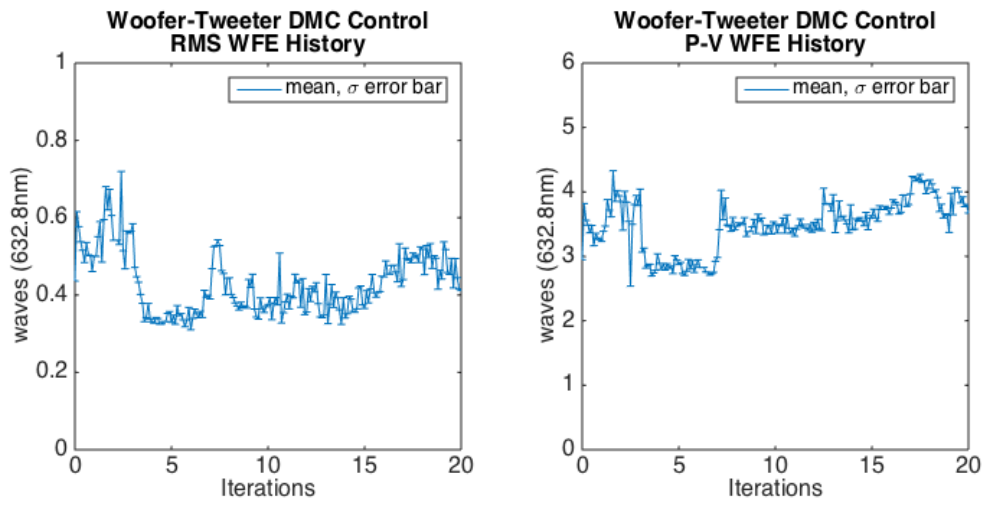
Figure 110. Woofer-tweeter distributed modal control wavefront error history woofer removed from tweeter
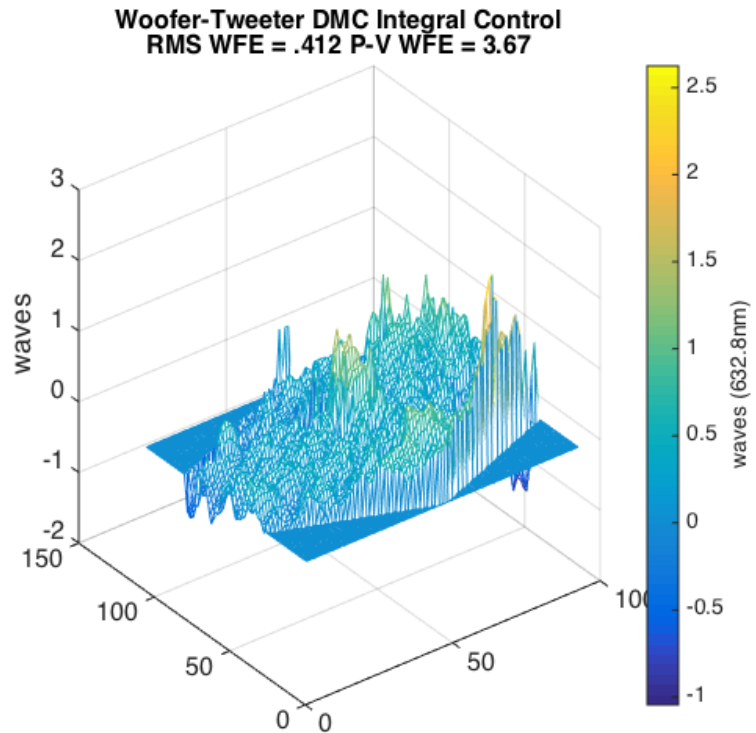

Figure 111. Woofer-tweeter distributed modal control, woofer removed from tweeter, residual surface error
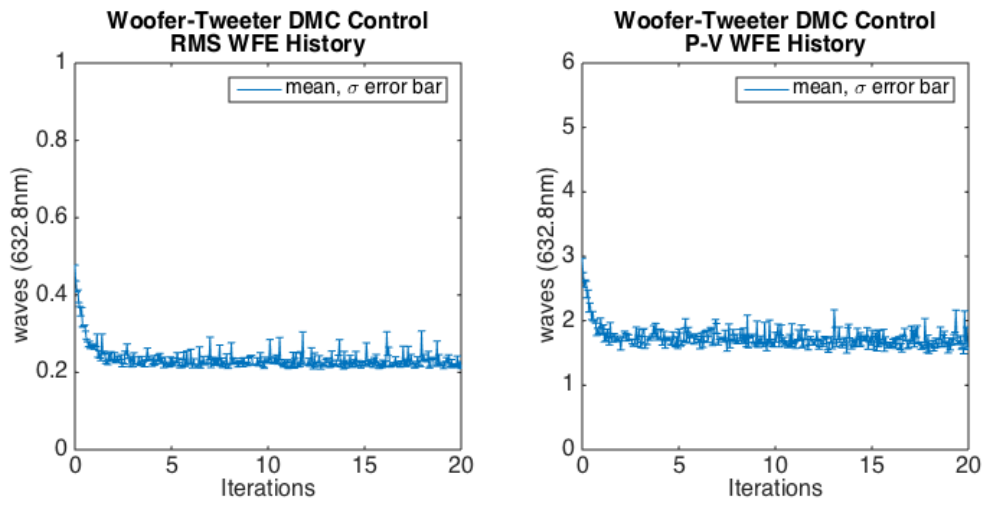
Figure 112. Woofer-tweeter distributed modal control wavefront error history,
mode 1-7 removed from tweeter
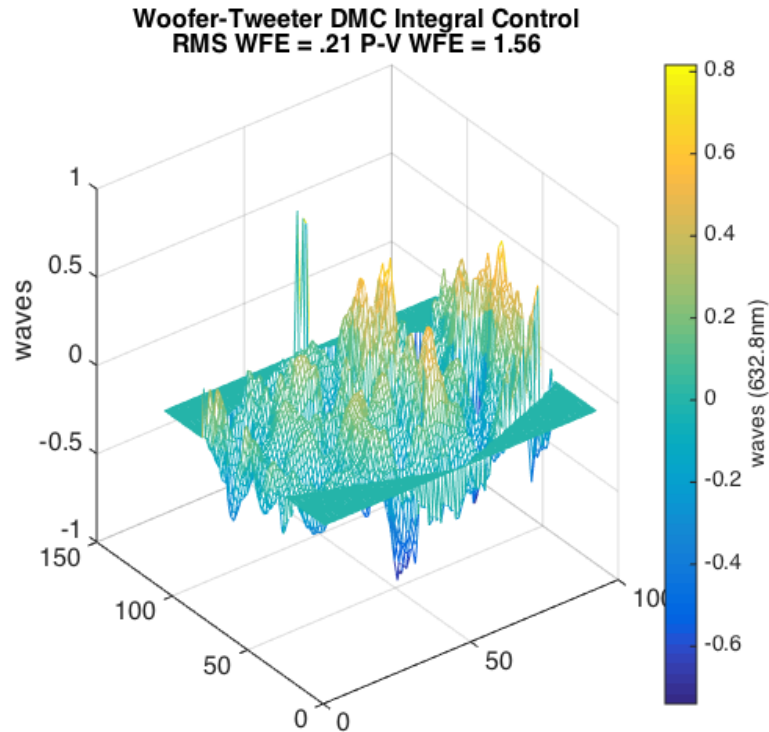
Figure 113. Woofer-tweeter distributed modal control, mode 1-7 removed from
tweeter, residual surface error

151
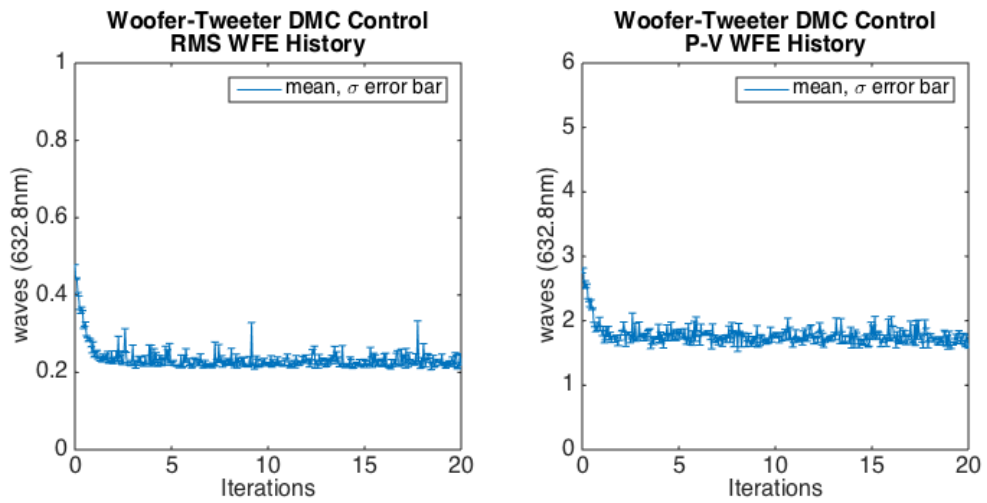
Figure 114. Woofer-tweeter distributed modal control wavefront error history, mode 1-11 removed from tweeter
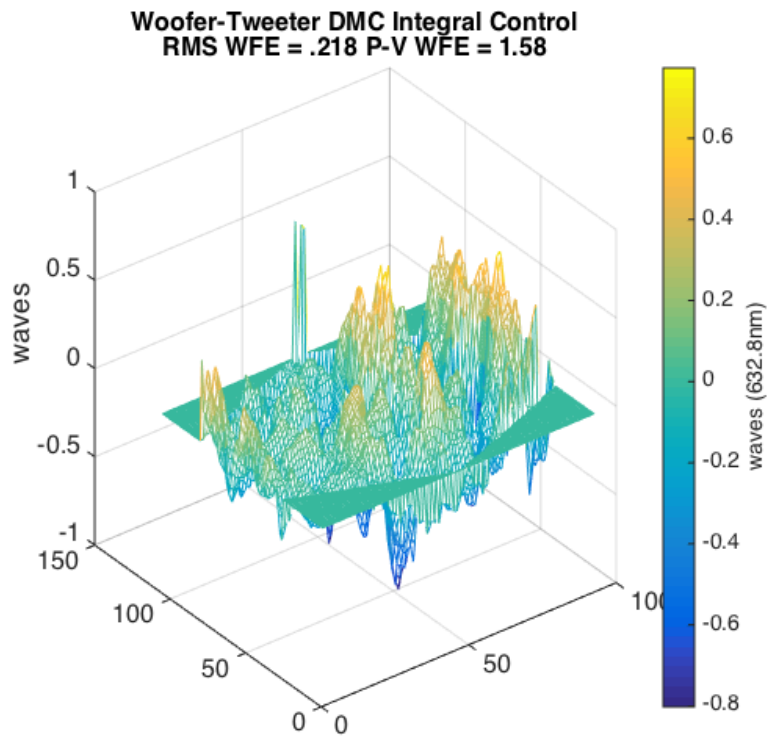

Figure 115. Woofer-tweeter distributed modal control, mode 1-11 removed from tweeter, residual surface error

APPENDIX B. EXPERIMENTAL RESULTS

Included in this appendix are the SMT test bed woofer-tweeter controller experimental results. The section includes wavefront error history plots presented as RMS wavefront error and peak-to-valley wavefront error measured in waves (632.8 nm). A trend line is fitted to the experimental data in the error plots. The open loop control results are presented as before and after surface plots.

A.   SMT AHM SEGMENT EXPERIMENTAL RESULTS

This section includes experimental results for correcting the SMT AHM segment. This includes integral control, iterative constrained minimization control, gradient control, and tweeter control.

1.   SMT Integral Control
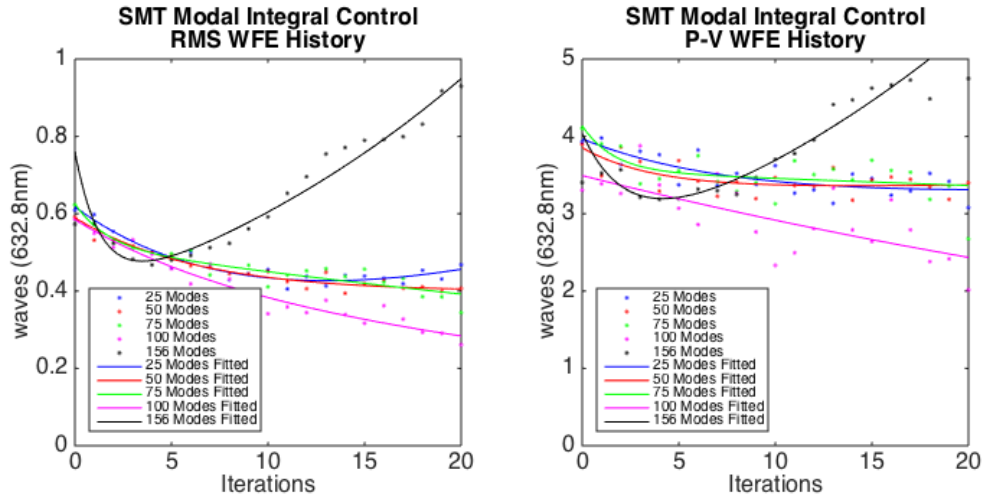
Figure 116. SMT AHM modal feedback integral control

153

2. SMT Iterative Constrained Minimization Control
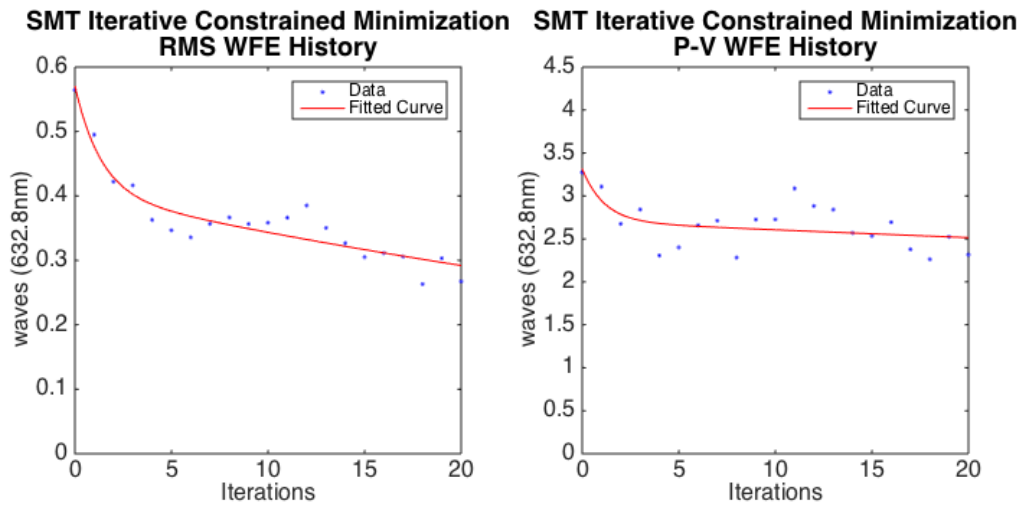

Figure 117. SMT AHM iterative constrained minimization control

3. SMT Gradient Control
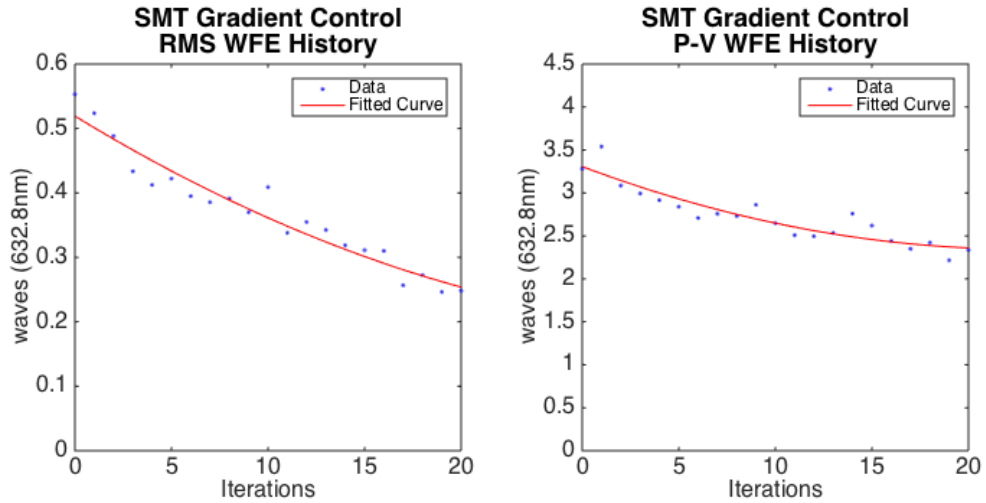
Figure 118. SMT AHM gradient control

4.   Tweeter Correction
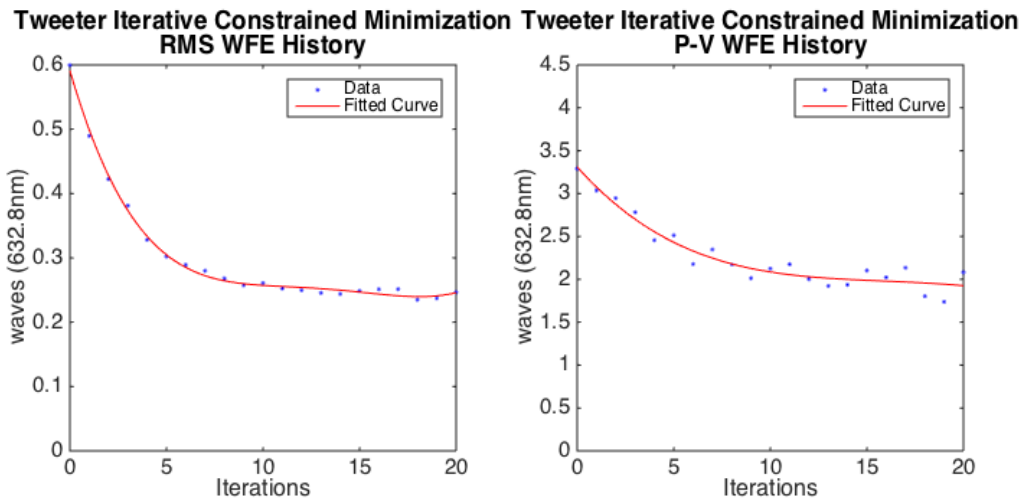
Figure 119. SMT AHM tweeter correction
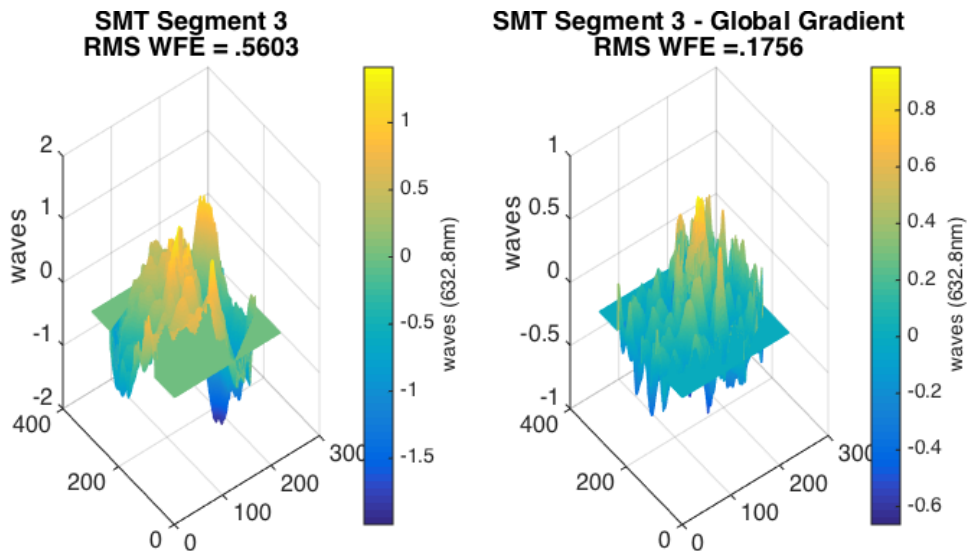
Figure 120. Comparison of static SMT wavefront error before and after correction using deformable mirror with global gradient control

B. WOOFER-TWEETER CLOSED LOOP EXPERIMENTAL RESULTS

This section includes woofer-tweeter closed loop control results including the 2-step iterative constrained least squares controller, global controllers, and distributed modal controller.

1. Serial Control Constrained Minimization Control
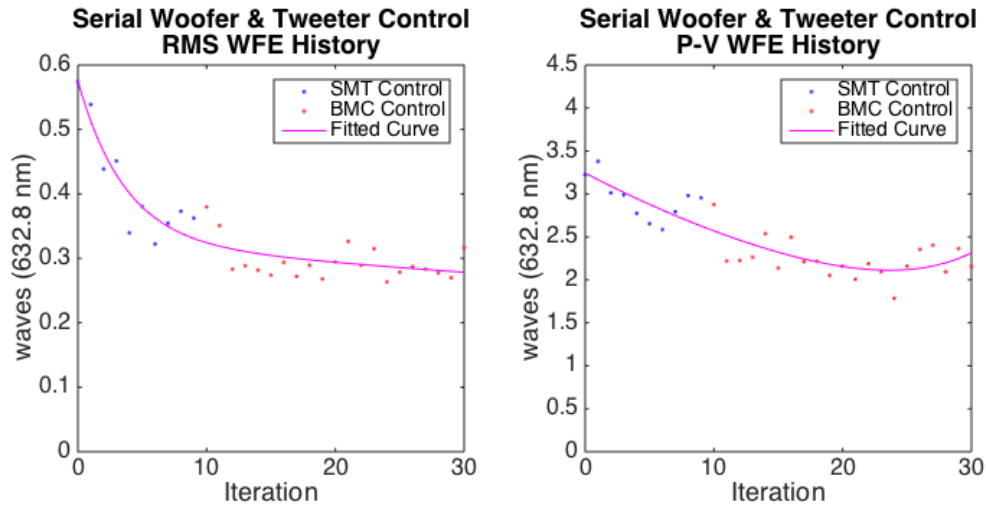
Figure 121. Serial integral control
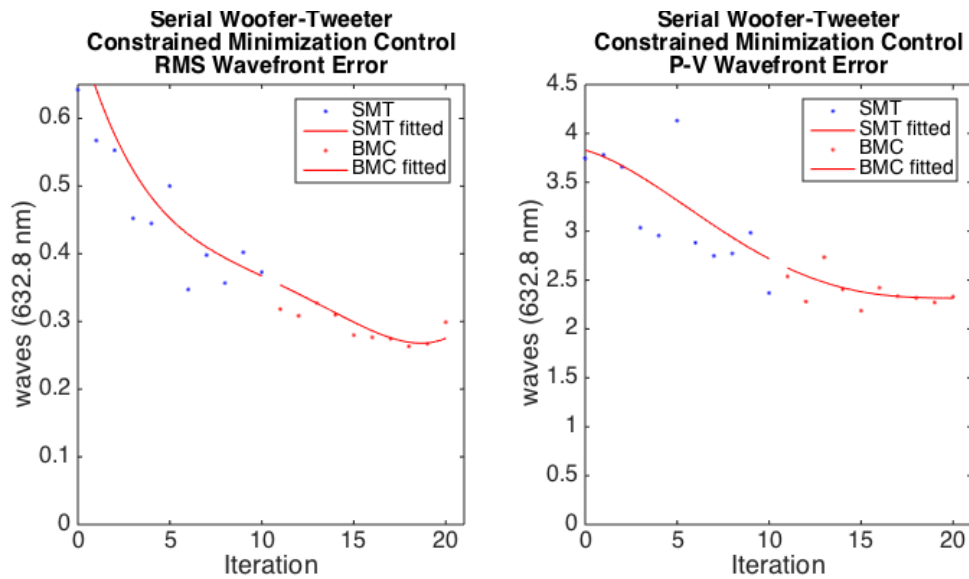
Figure 122. Serial constrained minimization control

2. Global Control

a. *Global Integral Control*
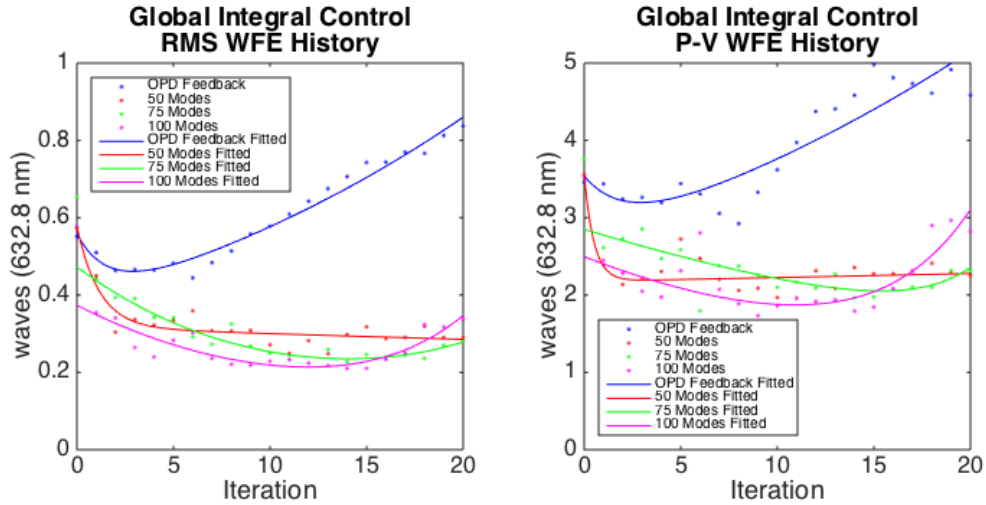
Figure 123. Global integral control

b. *Global Iterative Constrained Minimization Control*
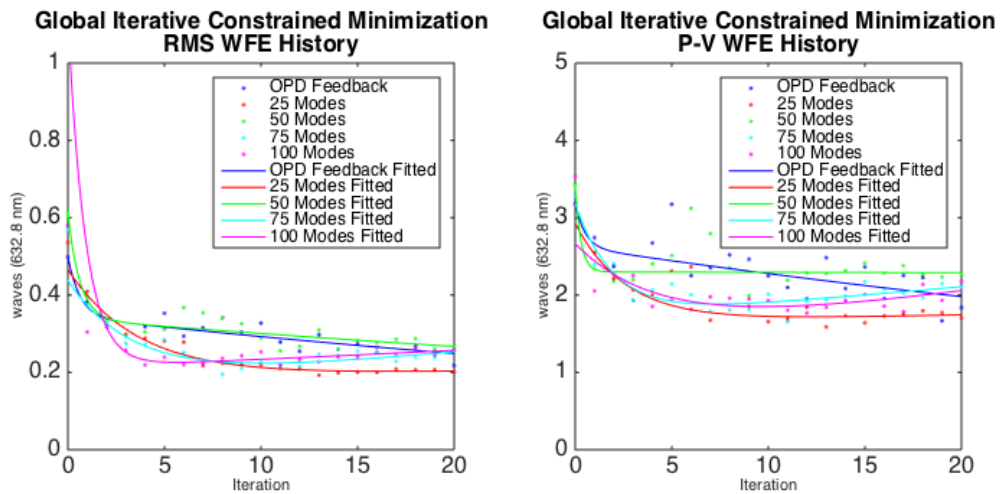
Figure 124. Global iterative constrained minimization control

c. ***Gradient Control***
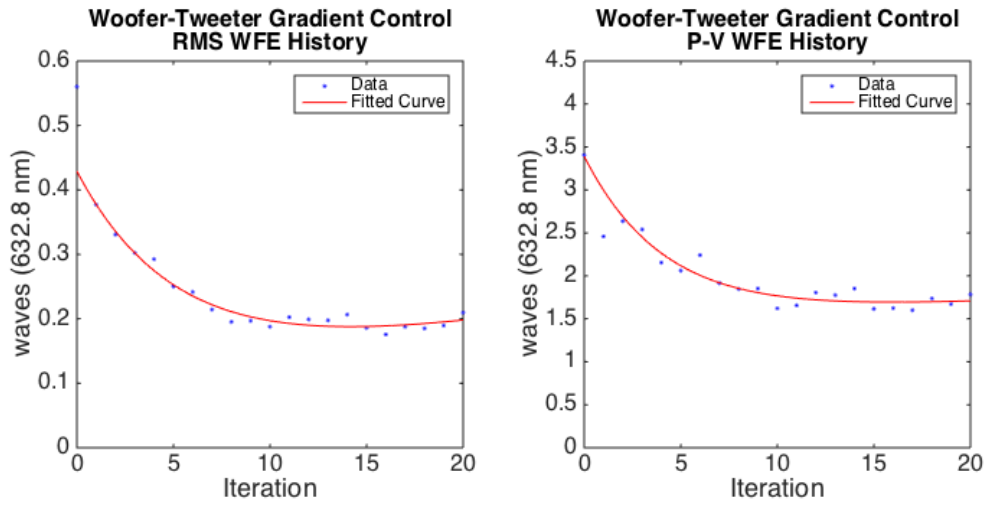
Figure 125. Woofer-tweeter gradient control

3. Offload Control

Experimental offload control techniques are shown in this section using an integral controller and a constrained minimization controller.

*a.* ***Offload Integral Control***
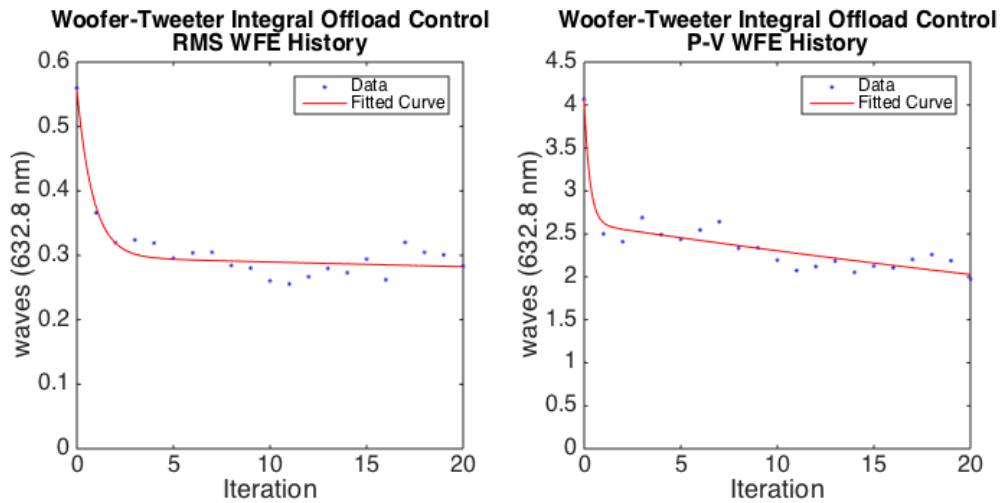
Figure 126. Offload integral control

b. ***Offload Iterative Constrained Minimization Control***
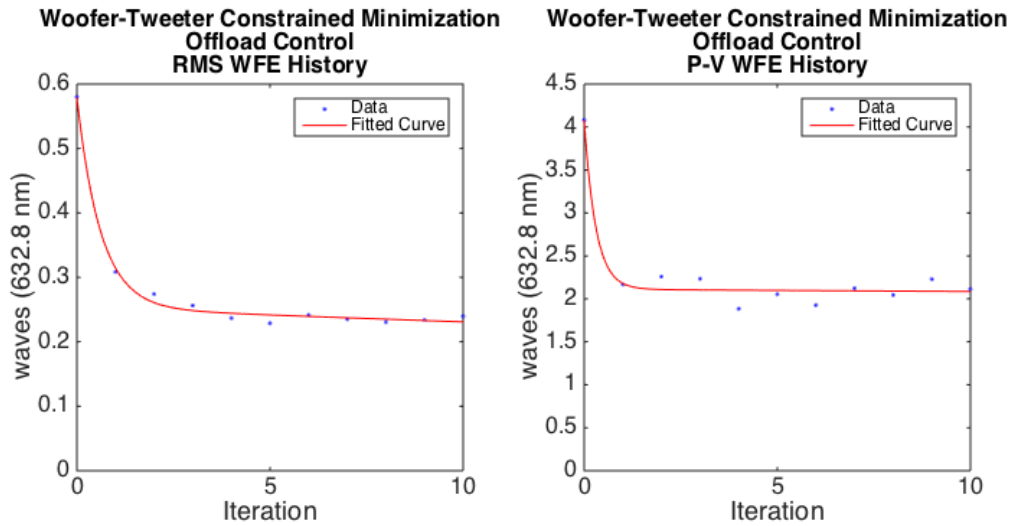
Figure 127. Offload iterative constrained minimization

4. Distributed Modal Control

This section presents the distributed modal control experimental results for two cases. The first case removes the first 7 SVD woofer modes from the tweeter and the second case removes the first 11 SVD woofer modes from the tweeter. The experiments were run for different modal feedback settings. These settings removed higher frequency modes from the feedback.

159
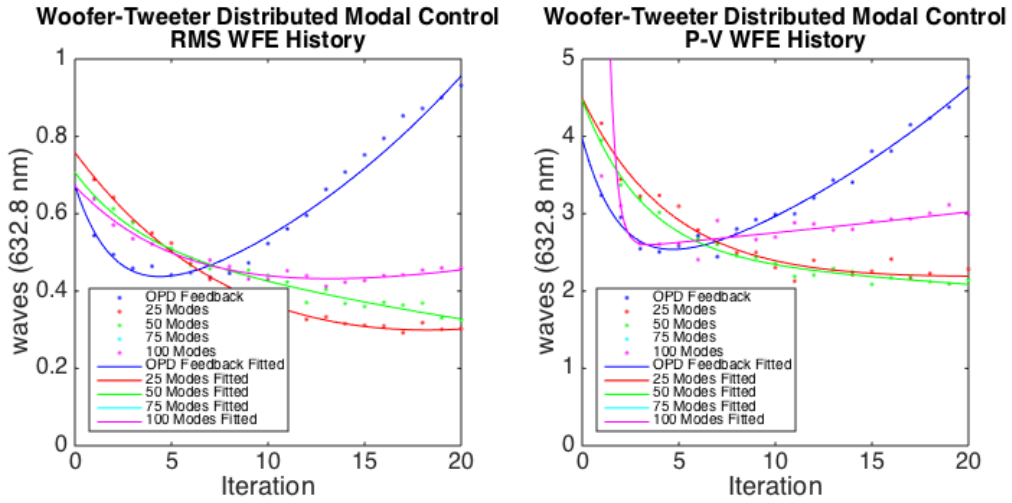
Figure 128. Distributed modal control, SVD woofer modes 1-7 removed from tweeter
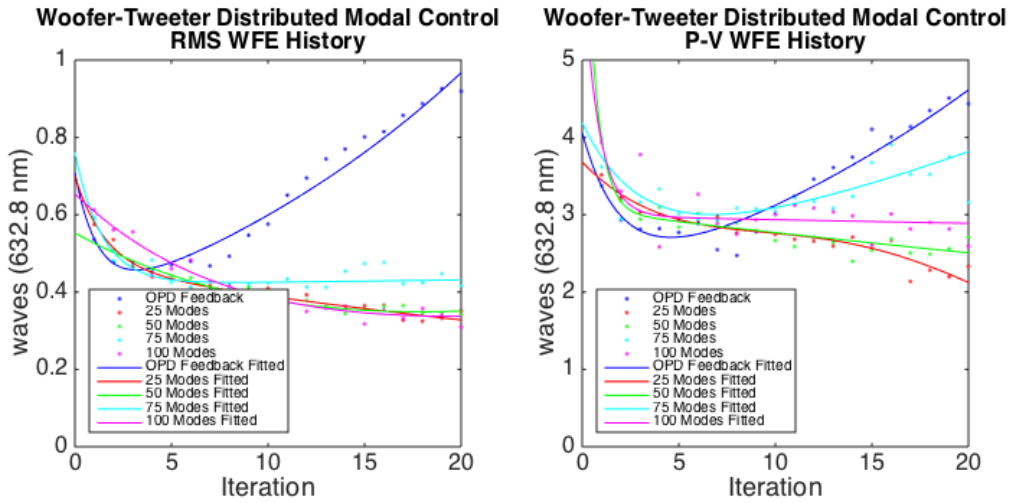
Figure 129. Distributed modal control, SVD woofer modes 1-11 removed from tweeter

C.   OPEN LOOP EXPERIMENTAL RESULTS

This section includes the open loop experimental results using the SMT AHM segment and the woofer-tweeter experimental setup. The cost function (4.40) from Chapter IV is used and presented again.   Three minimizations are performed with

different weighting coefficients, shown in Table 3. The minimization was solved using the MATLAB function *fmincon.m*.

$$\arg\min J(u) = \frac{1}{2}\left(c_1\left(\{\phi\}^T\{\phi\}\right) + c_2\left(\max(\{\phi\}) - \min(\{\phi\})\right) + c_3\left(\{v_\Delta\}^T\{v_\Delta\}\right) + c_4\left(\{u\}^T\{u\}\right)\right)$$

subject to: $lb \leq \{u\} \leq ub$

Table 4.   Cost function coefficients

	c1	c2	c3	c4
Cost Function 1	1	0	0	0
Cost Function 2	1	2	0	0
Cost Function 3	1	1	0	5.00E-04

The experiments were completed 10 times and the final wavefront error results were averaged. The surface plots below show the resulting surface error for a single experiment.
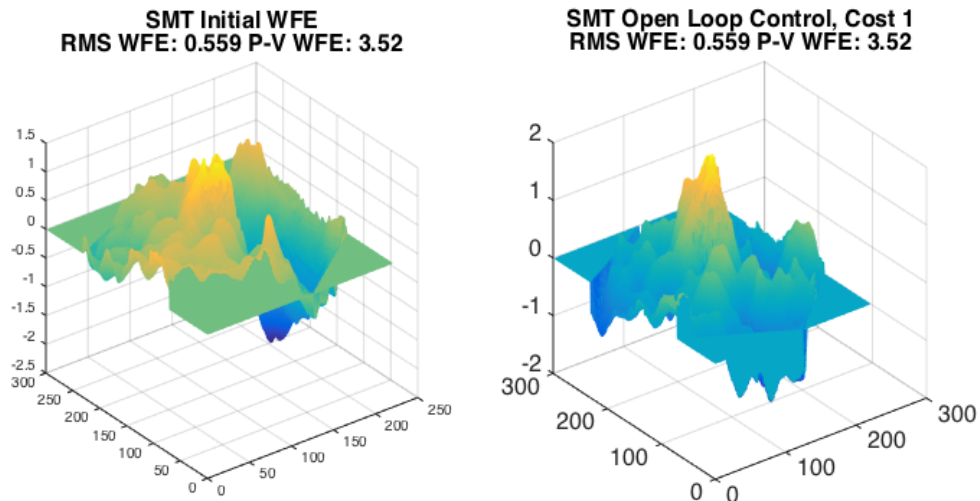
Figure 130. SMT open loop minimization, cost function 1
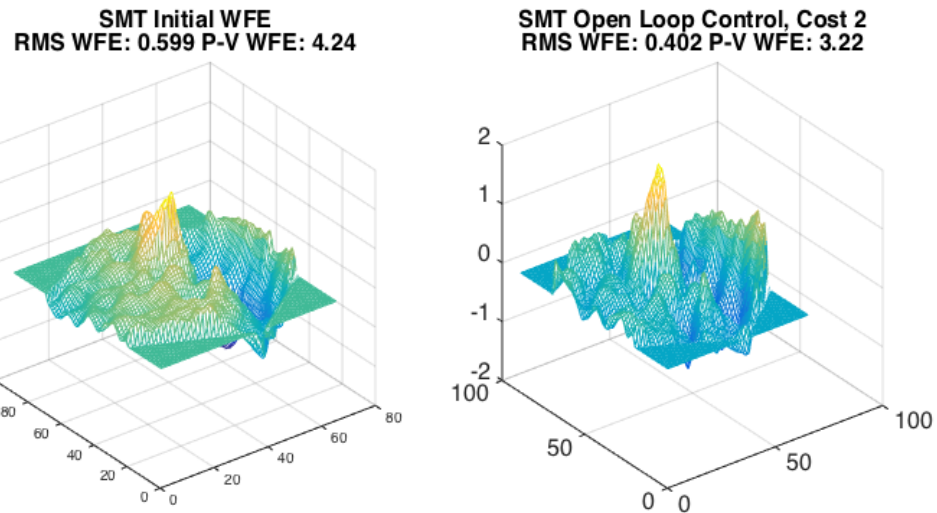
Figure 131. SMT open loop minimization, cost function 2
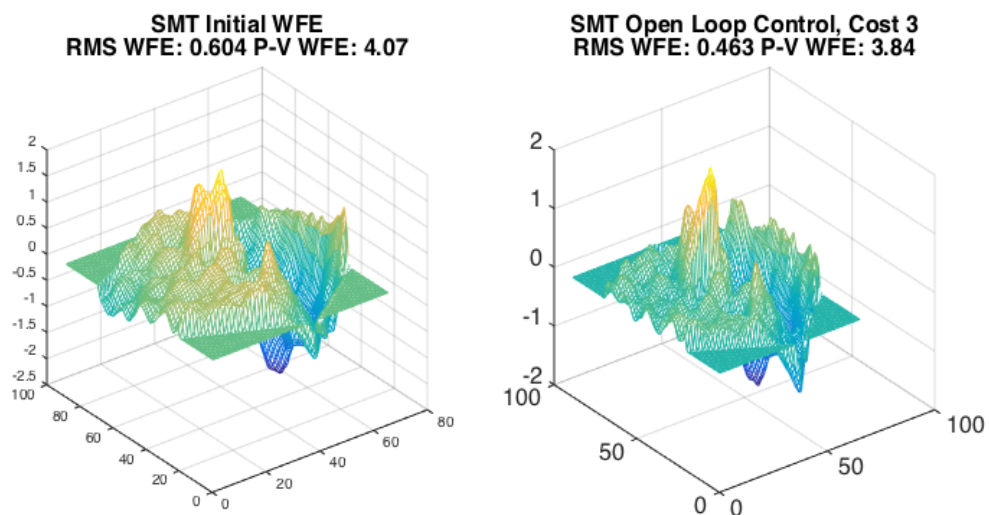
Figure 132. SMT open loop minimization, cost function 3
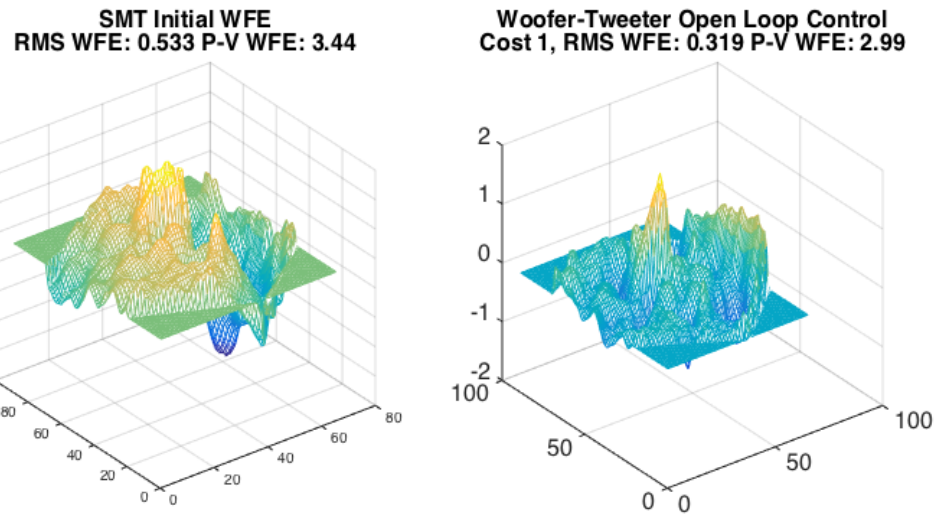
Figure 133. Woofer-tweeter open loop minimization, cost function 1
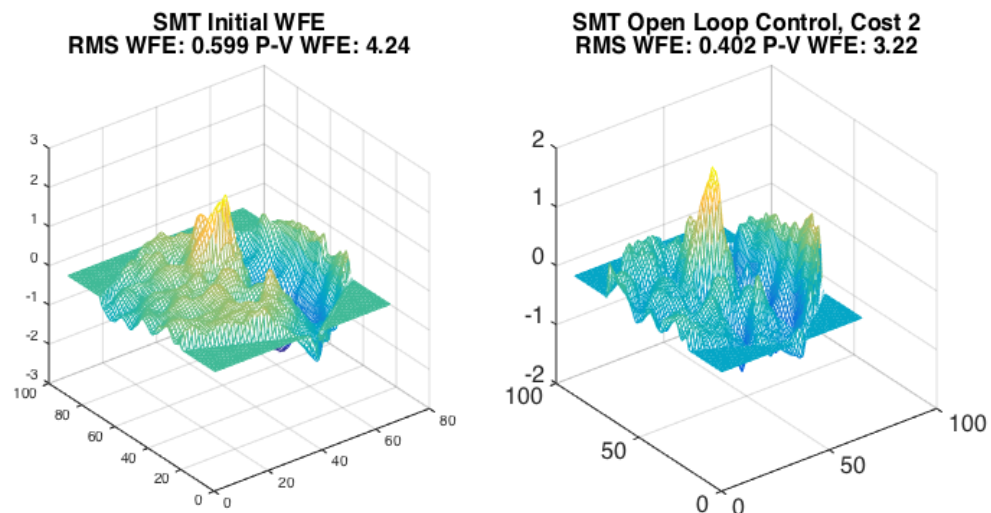
Figure 134. Woofer-tweeter open loop minimization, cost function 2
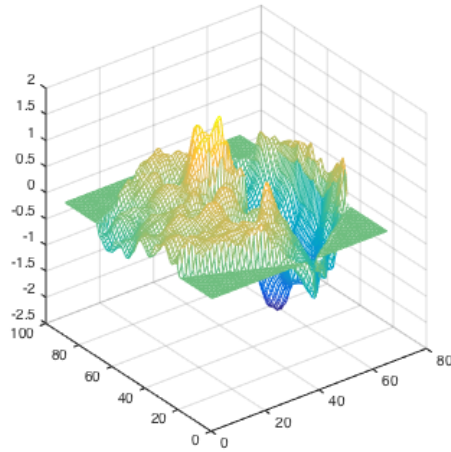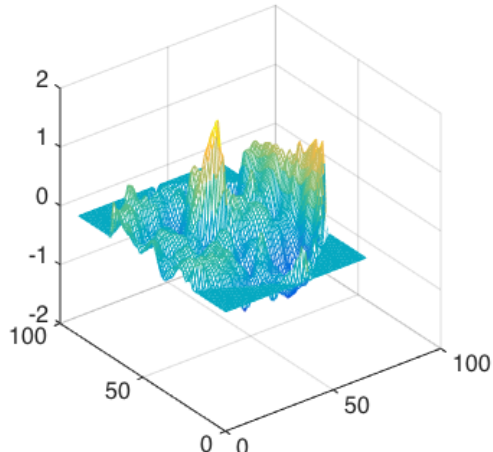
Figure 135. Woofer-tweeter open loop minimization, cost function 3

LIST OF REFERENCES

[1]   U.S. Department of Defense, "National Security Space Strategy," Jan. 2011.

[2]   W. E. Howell, "Recent advances in optical control for large space telescopes," in *Space Optics: Proceedings of the Ninth International Congress of the International Commission for Optics (ico IX)*, 1974, pp. 239–258.

[3]   H. W. Babcock, "The possibility of compensating astronomical seeing," *Publ. Astron. Soc. Pac.*, vol. 65, Oct. 1953, pp. 229–236.

[4]   J. E. Nelson, T. S. Mast, and S. M. Faber, "The design of the Keck Observatory and telescope," Caltech, Pasadena, CA, Report Observatory Rep. 90, Nov. 1985. [Online]. Available: http://resolver.caltech.edu/CaltechAUTHORS:20130225-104253452

[5]   G. Chanan, M. Troy, F. Dekens, S. Michaels, J. Nelson, T. Mast, and D. Kirkman, "Phasing the mirror segments of the Keck Telescopes: The broadband phasing algorithm," *Appl. Opt.*, vol. 37, no. 1, Jan. 1998, pp. 140-155.

[6]   G. Chanan, C. Ohara, and M. Troy, "Phasing the mirror segments of the Keck Telescopes II: The narrow-band phasing algorithm," *Appl. Opt.*, vol. 39, no. 25, Sep. 2000, pp. 4706-4714.

[7]   G. A. Chanan, M. Troy, and C. M. Ohara, "Phasing the primary mirror segments of the Keck telescopes: A comparison of different techniques," *Proc. of SPIE*, vol. 4003, 2000, pp. 188–202.

[8]   G. Chanan, M. Troy, and E. Sirko, "Phase discontinuity sensing: a method for phasing segmented mirrors in the infrared," *Appl. Opt.*, vol. 38, no. 4, Feb. 1999, pp. 704-713.

[9]   S. A. Lane, S. L. Lacy, V. Babuska, S. Hanes, K. Schrader, and R. Fuentes, "Active vibration control of a deployable optical telescope," *J. Spacecr. Rockets*, vol. 45, no. 3, May 2008, pp. 568–586.

[10]   F. Shi, D. C. Redding, J. J. Green, and C. M. Ohara, "Performance of segmented mirror coarse phasing with a dispersed fringe sensor: modeling and simulations," *Proc. of SPIE*, vol. 5487, 2004, pp. 897–908.

[11]   D. C. Redding, S. A. Basinger, D. Cohen, A. E. Lowman, F. Shi, P. Y. Bely, C. W. Bowers, R. Burg, L. A. Burns, P. S. Davila, B. H. Dean, G. E. Mosier, T. A. Norton, P. Petrone III, B. D. Perkins, and M. E. Wilson, "Wavefront control for a segmented deployable space telescope," *Proc. of SPIE,* vol. 4013, 2000, pp. 546–558.

[12] G. S. Hickey, S.-S. Lih, and J., Troy W. Barbee, "Development of nanolaminate thin-shell mirrors," *Proc. of* SPIE, vol. 4849, 2002, pp. 63–76.

[13] G. Hickey, T. Barbee, M. Ealey, and D. Redding, "Actuated hybrid mirrors for space telescopes," in *Proc. of SPIE*, vol. 7731, 2010.

[14] R. C. Romeo, R. N. Martin, B. Twarog, B. Anthony-Twarog, R. Taghavi, R. Hale, P. Etzel, R. Fesen, and S. Shawl, "Progress in the ULTRA 1-m ground-based telescope," *Proc. of SPIE*, vol. 6267, 2006, pp. 62670D–62670D–7.

[15] J. Steeves, M. Laslandes, S. Pellegrino, D. Redding, S. C. Bradford, J. K. Wallace, and T. Barbee, "Design, fabrication and testing of active carbon shell mirrors for space telescope applications," *Proc. of SPIE*, vol. 9151, 2014, pp. 915105–915105–13.

[16] M. R. Allen, J. J. Kim, and B. N. Agrawal, "Correction of active space telescope mirror using woofer-tweeter adaptive optics," in *Proc. SPIE*, Baltimore, Maryland, vol. 9469, April 2015.

[17] T. R. O' Meara, C. J. Swigert, and W. P. Brown, "Adaptive optics for space telescopes," in *Proc. SPIE*, vol. 0075, 1976, pp. 126–135.

[18] T. L. Gray, M. W. Smith, L. E. Cohan, and D. W. Miller, "Minimizing high spatial frequency residual error in active space telescope mirrors," in *Proc. SPIE*, vol. 7436, 2009.

[19] L. David, "Mirrors finished for NASA's new James Webb Space Telescope," Space.com. [Online]. Available: http://www.space.com/17202-nasa-james-webb-space-telescope-mirrors.html. Accessed July 16, 2015..

[20] R. E. Parks, "Overview of optical manufacturing methods," in *Proc. SPIE*, vol. 306, 1982, pp. 2–12.

[21] G. Hickey, T. Barbee, M. Ealey, and D. Redding, "Actuated hybrid mirrors for space telescopes," in *Proc. SPIE*, vol. 7731, 2010.

[22] D. Baiocchi and H. P. Stahl, "Enabling future space telescopes: mirror technology review and development roadmap," in *astro2010: The Astronomy and Astrophysics Decadal Survey*, vol. 2010, pp. 23–34.

[23] H. P. Stahl, L. D. Feinberg, and S. C. Texter, "JWST primary mirror material selection," 2004, vol. 5487, 2009, pp. 818–824.

[24] D. Baiocchi, "Design and control of lightweight, active space mirrors," Dissertation, University of Arizona, 2004.

[25]   J. H. Burge, B. Cuerden, S. M. Miller III, R. C. Crawford, H. H. Dorth, D. G. Sandler, and R. W. Wortley, "Manufacture of a 2-m mirror with a glass membrane facesheet and active rigid support," *Proc. of SPIE*, vol. 3782, 1999, pp. 123–133.

[26]   M. A. Ealey, "Integrated zonal meniscus mirror," U.S. Patent CA2516991 A1, Sep. 10, 2004.

[27]   J., T.W. Barbee, "Nano-laminates: A new class of materials for aerospace applications," in *2003 IEEE Aerospace Conference, 2003 Proceedings*, vol. 4, 2003, pp. 4_1745–4_1754.

[28]   R. C. Romeo, "CFRP composites for optics and structures in telescope applications," *Proc. of SPIE*, vol. 2543, 1995, pp. 154–161.

[29]   B. Coughenour, S. M. Ammons, M. Hart, R. Romeo, R. Martin, M. Rademacher, and H. Bailey, "Demonstration of a robust curved carbon fiber reinforced polymer deformable mirror with low surface error," *Proc. of SPIE*, vol. 7736, 2010, pp. 77363I–77363I–9.

[30]   M. E. L. Jungwirth, C. C. Wilcox, D. V. Wick, M. S. Baker, C. G. Hobart, J. J. Milinazzo, J. Robichaud, R. C. Romeo, R. N. Martin, J. Ballesta, E. Lavergne, and E. L. Dereniak, "Large-aperture active optical carbon fiber reinforced polymer mirror," *Proc. of SPIE*, vol. 8725, 2013, pp. 87250W–1-87250W–11.

[31]   M. E. L. Jungwirth, C. C. Wilcox, R. C. Romeo, D. V. Wick, E. L. Dereniak, R. N. Martin, and M. S. Baker, "Actuation for carbon fiber reinforced polymer active optical mirrors," in *2012 IEEE Aerospace Conference*, 2012, pp. 1–9.

[32]   J. W. Hardy, *Adaptive Optics for Astronomical Telescopes*, New York, NY: Oxford University Press, 1998.

[33]   J. W. Hardy, "Adaptive optics: a progress review," *Proc. of SPIE*, vol. 1542, 1991, pp. 2–17.

[34]   D. P. Greenwood and C. A. Primmerman, "History of Adaptive Optics Development at the MIT Lincoln Laboratory," *Proc. of SPIE*, vol. 1920, 1993, pp. 220–234.

[35]   F. Y. Kanev and V. P. Lukin, "Amplitude phase beam control with the help of a two-mirror adaptive system," *Atmo Ocean. Opt*, vol. 4, no. 12, Dec. 1991, pp. 878–880.

[36]   M. C. Roggemann and D. J. Lee, "Two-deformable-mirror concept for correcting scintillation effects in laser beam projection through the turbulent atmosphere," *Appl. Opt.*, vol. 37, no. 21, Jul. 1998, pp. 4577–4585.

[37] B. L. Kelchner and R. C. Dauk, "ABL beam control segment," in *Proc. SPIE*, vol. 3381, Apr. 1998, pp. 8–13.

[38] P. J. Hampton, R. Conan, C. Bradley, and P. Agathoklis, "Control of a woofer tweeter system of deformable mirrors," in *Proc. SPIE*, vol. 6274, 2006.

[39] D. Gavel and A. Norton, "Woofer-tweeter deformable mirror control for closed-loop adaptive optics: theory and practice," in *Proc. of SPIE*, vol. 9148, 2014.

[40] W. H. Southwell, "Wave-front estimation from wave-front slope measurements," *J. Opt. Soc. Am.*, vol. 70, no. 8, Aug. 1980, pp. 998–1006.

[41] J. R. Fienup, B. J. Thelen, R. G. Paxman, and D. A. Carrara, "Comparision of phase diversity and curvature wavefront sensing," *SPIE Conf. Adapt. Opt. Syst. Technol.*, vol. 3353, Mar. 1998.

[42] F. Roddier, "Curvature sensing and compensation: a new concept in adaptive optics," *Appl. Opt.*, vol. 27, no. 7, Apr. 1988, pp. 1223–1225.

[43] N. A. Roddier, "Algorithms for wavefront reconstruction out of curvature sensing data," in *SPIE Active and Adaptie Optical Systems*, vol. 1542, 1991, pp. 120–129.

[44] R. W. Gerchberg and W. O. Saxton, "A practical algorithm for the determination of phase from image and diffraction plane pictures," *Optik*, vol. 35, no. 2, 1972, pp. 237–246.

[45] D. C. Redding, S. A. Basinger, S. Bikkannavar, D. Chohen, J. J. Green, C. M. Ohara, and F. Shi, "How defocused images are used to measure phase: An explanation of the modified Gerchberg-Saxton phase retrieval software.", unpublished, Jet Propulsion Laboratory, California Institute of Technology.

[46] F. Shi, S. A. Basinger, and D. C. Redding, "Performance of dispersed fringe sensor in the presence of segmented mirror aberrations: modeling and simulation," 2006, *Proc. of SPIE*, vol. 6265, pp. 62650Y–62650Y–12.

[47] R. K. Tyson, *Principles of Adaptive Optics*, 2nd ed, San Diego, CA: Academic Press, 1998.

[48] R. K. Tyson and B. W. Frazier, *Field Guide to Adaptive Optics*, 2nd ed., Bellingham, WA: SPIE Press, 2012.

[49] A. Wirth and A. Jankevics, "Final report: Segmented mirror study." AOA Xinetics, Northrup Grumman Corporation, Mar. 2014.

[50] S.-J. Chung, D. W. Miller, and O. L. de Weck, "ARGOS testbed: study of multidisciplinary challenges of future spaceborne interferometric arrays," *Opt. Eng.*, vol. 43, no. 9, pp. 2156–2167, Sep. 2004.

[51]   M. Postman, T. Brown, K. Sembach, M. Giavalisco, W. Traub, K. Stapelfeldt, D. Calzetti, W. Oegerle, R. Michael Rich, H. Phillip Stahl, J. Tumlinson, M. Mountain, R. Soummer, and T. Hyde, "Advanced Technology Large-Aperture Space Telescope: Science drivers and technology developments," *Opt. Eng.*, vol. 51, no. 1, pp. 011007–1, 2012.

[52]   M. Postman, W. B. Sparks, F. Liu, K. Ess, J. Green, K. G. Carpenter, H. Thronson, and R. Goullioud, "Using the ISS as a testbed to prepare for the next generation of space-based telescopes," *Proc. of SPIE,* vol. 8442, 2012, pp. 84421T–84421T–10.

[53]   C. Lee, "Comparison optical telescope primary mirrors." (2014 July 28). Wikipedia. [Online]. Available: http://en.wikipedia.org/wiki/File: Comparison_optical_telescope_primary _mirrors.svg. Accessed Apr 17, 2015.

[54]   A. Yingling, "Integrated optics, structures, and controls of segmented mirror telescopes," Dissertation, Naval Postgraduate School, Monterey, CA, 2012.

[55]   D. C. Redding, G. Hickey, G. Agnes, P. Eisenhardt, J. J. Green, J. Krist, L. Peterson, K. Stapelfeldt, W. A. Traub, S. Unwin, and M. Werner, "Active optics for a 16-Meter advanced technology large aperture space telescope." Jet Propulsion Laboratory, California Institute of Technology, Jun. 2008.

[56]   D. C. Redding, F. Shi, S. A. Basinger, D. Cohen, J. J. Green, A. E. Lowman, and C. M. Ohara, "Wavefront sensing and control for large space optics," in *IEEE Aerospace Conference, 2003 Proceedings*, vol. 4, 2003, pp. 4_1729–4_1744.

[57]   C. L. Hom and C. Bampton, "Opto-mechanical plant model for the segmented mirror demonstrator (SMD)," Advanced Technology Center, Lockheed Martin Space Corporation, Nov. 2012.

[58]   B. Agrawal, T. Matinez, J. Bagnasco, and A. Yingling, "Segmented Mirror Telescope Laboratory annual report 2012," Naval Postgraduate School, Monterey CA, Dec. 2012.

[59]   D. Burtz, "Fine surface control of flexible space mirrors using adaptive optics and robust control," Dissertation, Naval Postgraduate School, Monterey, CA, 2009.

[60]   M. Looysen, "Combined integral and robust control of the segmented mirror telescope," Master's thesis, Naval Postgraduate School, Monterey, CA, 2009.

[61]   M. Nagashima and B. N. Agrawal, "Active control of adaptive optics system in a large segmented mirror telescope." Naval Postgraduate School, Monterey, CA, 2011.

[62]   T. W. Axtell, "Wavefront reconstruction and mirror surface optimization for adaptive optics," Dissertation, Naval Postgraduate School, Monterey, CA, Jun. 2014.

[63]   L. Dras, A. L. Jennings, and R. Cobb, "Model complexity reduction of a segmented mirror telescope," in *AIAA Modeling and Simulation Technologies Conference*, American Institute of Aeronautics and Astronautics, Jan. 2014.

[64]   J. Bagnasco, T. Martinez, B. Agrawal, J. J. Kim, B. Fernandez, J. Watson, and T. Axtell, "Correction of space telescope surface figure error using a deformable mirror," in *AIAA SPACE 2014 Conference and Exposition*, San Diego, CA, 2014.

[65]   J. J. Watson, "Correcting surface figure error in imaging satellites using a deformable mirror," Master's thesis, Naval Postgraduate School, Monterey, CA, Dec. 2013.

[66]   R. Conan, C. Bradley, P. Hampton, O. Keskin, A. Hilton, and C. Blain, "Distributed modal command for a two-deformable-mirror adaptive optics system," *Appl. Opt.*, vol. 46, no. 20, 2007, pp. 4329–4340.

[67]   T. J. Brennan and T. A. Rhoadarmer, "Performance of a woofer-tweeter deformable mirror control architecture for high-bandwidth high-spatial resolution adaptive optics," *Proc. of SPIE*, vol. 6306, Aug. 2006.

[68]   C. Correia, H. F. Raynaud, C. Kulcsár, and J. M. Conan, "Minimum variance control for the woofer-tweeter concept," Frontiers in Optics 2009/Laser Science XXV/Fall 2009 OSA Optics & Photonics Technical Digest, Optical Society of America Technical Digest, 2009, paper AOWB4.

[69]   B. K. McComas, "Configurable adaptive optics for the correction of space-based optical systems," Dissertation, University of Colorado, Boulder, CO, 2002.

[70]   B. K. McComas, E. J. Friedman, R. B. Hooker, and M. A. Cermak, "Configurable adaptive optical system for imaging of ground-based targets from space," vol. 4884, 2003, pp. 233–244.

[71]   E. J. Friedman and B. K. McComas, "Synthetic guide star for on-orbit assembly and configuration of large earth remote sensing optical systems," U.S. Patent 6278100 B1, Aug. 2001.

[72]   D. T. Gavel, "Adaptive optics sensing and control development: final report on collaborative research with Naval Postgraduate School adaptive optics controls laboratory." University of California Observatories, Jan. 2011.

[73]   M. S. Scholl and G. N. Lawrence, "Adaptive optics for in-orbit aberration correction: spherical aberration feasibility study," *Appl. Opt.*, vol. 34, no. 31, Nov. 1995, pp. 7295.

[74] W. Jiang, N. Ling, X. Rao, and F. Shi, "Fitting capability of deformable mirror," in *Proc. of SPIE*, vol. 1542, 1991, pp. 130–137.

[75] C. Correia, H. F. Raynaud, C. Kulcsár, and J.-M. Conan, "Globally optimal minimum mean-square error control in adaptive optical systems with mirror dynamics," *Proc. of SPIE*, vol. 7015, 2008, pp. 70151F–1-70151F–12.

[76] K. Ogata, *Modern Control Engineering*, 4th ed., Upper Saddle River, NJ: Prentice Hall, 2002.

[77] L. Zhu, P. C. Sun, D. U. Bartsch, W. R. Freeman, and Y. Fainman, "Adaptive control of a micromachined continuous-membrane deformable mirror for aberration compensation," *Appl. Opt.*, vol. 38, no. 1, Jan. 1999, pp. 168–176.

[78] P. Hampton, C. Bradley, P. Agathoklis, and R. Conan, "Control system performance of a woofer-tweeter adaptive optics system," in *The Advanced Maui Optical and Space Surveillance Technologies Conference*, vol.1, 2006, pp. 59–69.

[79] S. Hu, B. Xu, X. Zhang, J. Hou, J. Wu, and W. Jiang, "Double-deformable-mirror adaptive optics system for phase compensation," *Appl. Opt.*, vol. 45, no. 12, 2006 pp. 2638–2642.

[80] D. C. Redding, "Wavefront control with masks and actuator penalty functions." unpublished, Jet Propulsion Lab, Pasadena CA, Dec. 2009.

THIS PAGE INTENTIONALLY LEFT BLANK

INITIAL DISTRIBUTION LIST

1.   Defense Technical Information Center
        Ft. Belvoir, Virginia

2.   Dudley Knox Library
        Naval Postgraduate School
        Monterey, California